ESTIMATION STRATEGIES FOR CONSTRAINED AND HYBRID DYNAMICAL SYSTEMS

A Dissertation

by

JULIE MARIE JONES PARISH

Submitted to the Office of Graduate Studies of
Texas A&M University
in partial fulfillment of the requirements for the degree of

DOCTOR OF PHILOSOPHY

August 2011

Major Subject: Aerospace Engineering

ESTIMATION STRATEGIES FOR CONSTRAINED AND HYBRID DYNAMICAL SYSTEMS

A Dissertation

by

JULIE MARIE JONES PARISH

Submitted to the Office of Graduate Studies of
Texas A&M University
in partial fulfillment of the requirements for the degree of

DOCTOR OF PHILOSOPHY

Approved by:

Chair of Committee,	John E. Hurtado
Committee Members,	John L. Junkins
	Daniele Mortari
	Alan Palazzolo
Head of Department,	Dimitris C. Lagoudas

August 2011

Major Subject: Aerospace Engineering

ABSTRACT

Estimation Strategies for Constrained
and Hybrid Dynamical Systems. (August 2011)
Julie Marie Jones Parish, B.S., Texas A&M University;
M.S., Texas A&M University
Chair of Advisory Committee: Dr. John E. Hurtado

The estimation approaches examined in this dissertation focus on manipulating system dynamical models to allow the well-known form of the continuous-discrete extended Kalman filter (CDEKF) to accommodate constrained and hybrid systems. This estimation algorithm filters sequential discrete measurements for nonlinear continuous systems modeled with ordinary differential equations. The aim of the research is to broaden the class of systems for which this common tool can be easily applied.

Equality constraints, holonomic or nonholonomic, or both, are commonly found in the system dynamics for vehicles, spacecraft, and robotics. These systems are frequently modeled with differential algebraic equations. In this dissertation, three tools for adapting the dynamics of constrained systems for implementation in the CDEKF are presented. These strategies address (1) constrained systems with quasi-velocities, (2) kinematically constrained redundant coordinate systems, and (3) systems for which an equality constraint can be broken. The direct linearization work for constrained systems modeled with quasi-velocities is demonstrated to be particularly useful for systems subject to nonholonomic constraints. Concerning redundant coordinate systems, the "constraint force" perspective is shown to be an effective

approximation for facilitating implementation of the CDEKF while providing similar performance to that of the fully developed estimation scheme. For systems subject to constraint violation, constraint monitoring methods are presented that allow the CDEKF to autonomously switch between constrained and unconstrained models. The efficacy of each of these approaches is shown through illustrative examples.

Hybrid dynamical systems are those modeled with both finite- and infinite-dimensional coordinates. The associated governing equations are integro-partial differential equations. As with constrained systems, these governing equations must be transformed in order to employ the CDEKF. Here, this transformation is accomplished through two finite-dimensional representations of the infinite-dimensional coordinate. The application of these two assumed modes methods to hybrid dynamical systems is outlined, and the performance of the approaches within the CDEKF are compared. Initial simulation results indicate that a quadratic assumed modes approach is more advantageous than a linear assumed modes approach for implementation in the CDEKF.

The dissertation concludes with a direct estimation methodology that constructs the Kalman filter directly from the system kinematics, potential energy, and measurement model. This derivation provides a straightforward method for building the CDEKF for discrete systems and relates these direct estimation ideas to the other work presented throughout the dissertation.

Together, this collection of estimation strategies provides methods for expanding the class of systems for which a proven, well-known estimation algorithm, the extended Kalman filter, can be applied. The accompanying illustrative examples and simulation results demonstrate the utility of the methods proposed herein.

To God be the glory.

For Allen, my husband and dearest friend.

1 Peter 4:8

ACKNOWLEDGMENTS

It is a truth universally acknowledged, that a motivated student in possession of a love for dynamics, must be in want of a doctorate. This endeavor, however, is accomplished only with the help of many. In my estimation, I have been blessed with the support of the most excellent academic family for which one could wish.

How great is my appreciation for Dr. John E. Hurtado, my research advisor since 2004. I am very thankful to have had the opportunity to work with such a kind, talented, and enthusiastic professor. Thank you not only for your technical leadership, but also for your support of my aspirations, patience with my disappointments, and guidance through my decisions. It is difficult to fully describe my gratitude for the time and energy you have invested in me, but perhaps a concise summary would better suit...

Drs. John Junkins and John Valasek have also mentored, encouraged, and helped me to mature technically and to successfully apply for research funding and employment. Furthermore, as described by the beloved and very quotable head of the family, each truly is "a dedicated, and I believe, stellar classroom teacher that takes great pride in development of people at all levels."

I also would like to extend my thanks to Dr. Daniele Mortari, with whom it is always a joy to work and to visit. To Drs. Alan Palazzolo and Shankar Bhattacharyya, thank you very much for serving on my graduate committee. I very much appreciate the time that each of you have taken to support the completion of my doctorate.

For funding my graduate studies, I thank the National Science Foundation, the Department of Defense, the Texas Space Grant Consortium, Zonta International, AIAA, Dr. Hurtado, and the Texas A&M Department of Aerospace Engineering.

To my academic sisters, brothers, and cousins, thank you for your love, friendship,

and encouragement over the years. I am particularly thankful to Lesley Weitz and Nick Denissen, who each have brought a unique combination of technical insight, camaraderie, and humor to my time at Texas A&M. So many others have positively impacted my time in graduate school, including Dasia Reyes, Carolina Restrepo, Jeremy Davis, James Doebbler, Kurt Cavalieri, Becky Bertsch, Kristen Johnson, and Xiaoli Bai.

In Allen, I am exceedingly blessed to have so supportive and loving a husband and best friend. This is truly *our* accomplishment, and I appreciate the sacrifices he has made toward this achievement.

Lastly, I again thank my advisor, Dr. Hurtado. It is my hope that he is ever sensible of my warmest gratitude towards the person who, by guiding me through my education, has been the means of accomplishing this goal.

TABLE OF CONTENTS

CHAPTER Page

LIST OF FIGURES

FIGURE Page

FIGURE Page

FIGURE Page

FIGURE Page

FIGURE Page

FIGURE Page

FIGURE Page

FIGURE Page

FIGURE Page

LIST OF TABLES

CHAPTER I

INTRODUCTION

Algorithms for filtering sensor measurements and estimating the states of a dynamical system are powerful tools in engineering. Estimation algorithms for dynamical systems that can modeled with ordinary differential equations (ODEs) are well-known and commonly implemented for both linear and nonlinear systems. These methods may be applied using a set of measurements (batch estimation) or an individual measurement (sequential estimation or filtering) [1]. Because batch estimation is not executed in real-time, sequential estimation is the focus of this work. The most ubiquitous sequential estimation technique is called the Kalman filter [2, 3]. For nonlinear systems, there exist extensions of the Kalman filter, including the extended Kalman filter and unscented Kalman filter [4, 5]. In this work, the extended Kalman filter is employed because it is better-known and more commonly implemented in aerospace applications.

For this dissertation, strategies for applying the extended Kalman filter are investigated for two types of dynamical systems that are not typically modeled with ODEs: constrained systems, which are commonly modeled with differential algebraic equations (DAEs), and hybrid dynamical equations, which are governed by integro-partial differential equations (IPDEs). Many aerospace systems are modeled with these types of equations. For space applications, tethered satellite systems and flexible satellites are examples of systems that can be modeled with DAEs and IPDEs, respectively [6, 7].

The journal model is *IEEE Transactions on Automatic Control*.

Regarding constrained systems, three specific types are considered: those with quasi-velocities, those with redundant coordinates, and those with constraint surfaces that change discretely. Through a judicious choice of quasi-velocities, the governing DAEs (employing generalized velocities) for a constrained system can be transformed into a system of ODEs (employing quasi-velocities). This approach is particularly useful for systems subject to nonholonomic constraints. This method can also be extended to redundant coordinate systems (which are kinematically constrained), though these systems can also be modeled with ODEs and generalized velocities through the use of Lagrange multipliers [8, 9]. For many applications, it is indeed more desirable to use redundant coordinates and generalized velocities due to the system's physical geometry, control design, or locations of sensors and control actuators. For the subset of systems subject to equality constraints that can be violated, monitoring constraint violation is useful for real-time determination of the more appropriate dynamical model of the system. Here, two strategies for sequentially estimating the states and constraint are examined.

For systems with an elastic body, sometimes generally called distributed parameter systems, an infinite-dimensional coordinate can be used to model the flexible components of the system [7]. Systems with only infinite-dimensional coordinates are called continuous systems, whereas systems that also have a discrete coordinate are called hybrid systems. For this dissertation, two finite-dimensional representations of the infinite-dimensional domain are investigated for use in an estimation scheme for hybrid dynamical systems.

This dissertation is divided into six main sections. The *Background* chapter outlines the ideas and tools implemented in the work, including an overview of dynamical modeling for discrete, constrained, and hybrid systems and an outline of the continuous-discrete extended Kalman filter (CDEKF). The chapter *Direct Lin-*

earization via the Gibbs Function describes a straightforward method for finding the linearized equations of motion using quasi-velocities for a constrained dynamical system. In *Redundant Coordinate System Estimation Strategy*, an alternative perspective that facilitates implementation of the extended Kalman filter for systems that employ redundant coordinates, and are subsequently kinematically constrained, is presented. The focus on constrained systems is continued in the next chapter, *Constraint Monitoring Estimation Strategy*. For this work, two methods for calculating the value of the constraint, as well as an associated variance, are presented. Subsequently, an algorithm for employing these estimates to select the constrained or unconstrained dynamical model, as appropriate, is outlined with several illustrative examples. Turning then to infinite-dimensional systems, *Hybrid System Estimation Strategy* investigates two methods for creating a finite-dimensional model of an infinite-dimensional hybrid system and estimating the resulting states. Lastly, *Direct Estimation* outlines a clear approach for constructing the CDEKF utilizing only the directly linearized equations of motion for a system. The dissertation concludes with a summary of the work and an appendix outlining a numerical method for finding the Eigenvalues for an linear ODE boundary-value problem.

CHAPTER II

BACKGROUND

In this chapter, the underlying mathematical models and estimation tools employed in this dissertation are presented. First, the construction of the dynamical models of discrete, constrained, and hybrid systems are presented from a Lagrangian perspective. The continuous-discrete extended Kalman filter is then outlined for dynamical systems modeled with ordinary differential equations. Throughout this dissertation, vector, matrix, and Einstein index notation are all utilized as needed [10].

A. Mathematical Models of Dynamical Systems

The motion of systems described with discrete coordinates can usually be modeled with ordinary differential equations via a Newton or Lagrangian approach [8, 11]. However, for constrained systems, the possible motions of a system are restricted because these governing equations are subject to a constraint, and a differential algebraic equation representation of the dynamics results. If, on the other hand, the system motion is augmented by a flexible-body component in addition to the rigid body components, an infinite-dimensional coordinate may be necessary to describe the motion of the system. The resulting hybrid dynamical system is modeled with integro-partial differential equations (whereas continuous systems, which do not include a discrete coordinate, are modeled with partial differential equations). In this section, the equations of motion for each of these types of systems are developed using Lagrange's equations. Lagrangian mechanics are particularly useful because they allow one to "develop a universal form of the differential equations of motion,

as a function of the system kinetic energy and unspecified generalized coordinates" [8]. The Lagrangian approach is selected because it employs velocity-level kinematics and provides clear representations of the governing equations for the general case of each class of system. The general forms of Lagrange's equations presented here can be derived from the extended Hamilton's principle [7, 12].

1. Kinematics

Kinematics describe the motion of a system without consideration of forces acting on the system [8, 11]. Regardless of system classification, the development of Lagrange's equations begins with the kinematics of a particle (or rigid body or continuum), representative of the system motion. Consider the position vector for one of $i = 1 \dots m$ particles of mass m_i in a discrete system.

$$\boldsymbol{r}_i = \boldsymbol{r}_i(q_j, t) \tag{2.1}$$

Here, q_j are the $j = 1 \dots n$ generalized coordinates of the system and t represents time. The velocity vector of the system is then the frame-independent time derivative of the position vector [11].

$$\dot{\boldsymbol{r}}_i = \dot{\boldsymbol{r}}_i(\dot{q}_j, q_j, t) \tag{2.2}$$

The overdot indicates differentiation with respect to time. Note that for rheonomic systems the velocity vector may be a function of time-varying parameters in addition to time, the general coordinates, and the generalized velocities $\dot{q}_j$. Using these velocity-level kinematics and the kinetic energy of the system, the Lagrangian L can be formed by summing the kinetic energies of the particles and subtracting the system potential energy.

$$L = T - V = \frac{1}{2} m_i \left(\dot{\boldsymbol{r}}_i \cdot \dot{\boldsymbol{r}}_i \right) - V \tag{2.3}$$

For systems with flexible bodies or rigid bodies, or both, the Lagrangian can be written in a similar manner once angular momentum or integration over the continuum, or both, are taken into account [7, 8, 11]. Once the Lagrangian is formed and non-potential forces Q_j, including control inputs, are identified, Lagrange's equations can be applied to find the equations of motion.

2. Discrete Systems

For unconstrained systems that can be described with discrete generalized coordinates and generalized velocities, Lagrange's equations are well-known.

$$\frac{\mathrm{d}}{\mathrm{dt}}\left(\frac{\partial L}{\partial \dot{q}_j}\right) - \frac{\partial L}{\partial q_j} = Q_j \tag{2.4}$$

Note that this form assumes that the potential energy is a function of the generalized coordinates alone, $V = V(\boldsymbol{q})$, which is common. The dynamical model that results from applying these equations has the form of ordinary differential equations. Eq. 2.4 can also be written without loss of generality in a form linear in the generalized accelerations.

$$M_{jl}(\dot{q}_i, q_i, t)\ddot{q}_l + g_j(\dot{q}_i, q_i, t) = Q_j \tag{2.5}$$

This equation can be further rearranged into state-vector form. This form of the equations assumes that the mass matrix M is invertible, which is usually the case for mechanical systems.

$$\begin{bmatrix} \dot{q}_j \\ \ddot{q}_j \end{bmatrix} = \begin{bmatrix} \dot{q}_j \\ M_{lj}^{-1}(\dot{q}_i, q_i, t)\left[-g_l(\dot{q}_i, q_i, t) + Q_l\right] \end{bmatrix} \tag{2.6}$$

Defining x_i, $i = 1 \ldots 2n$ as the complete set of states as written in Eq. 2.6—both the generalized coordinates and generalized velocities—these second-order ODEs can be

written in first-order form.

$$\dot{x}_i = f_i(x_j, Q_j, t) \tag{2.7}$$

Here, f_i, $i = 1 \ldots n$, represents the kinematic identity $\dot{x}_i = x_{i+n}$, and f_i, $i = n{+}1 \ldots 2n$ represents the contribution from Eq. 2.5.

3. Constrained Systems

For this work, only constrained systems that are subject to k equality constraints that can be written in Pfaffian form are considered.

$$\dot{\phi}_k(\dot{q}_i, q_i, t) = C_{kj}(q_i, t)\dot{q}_j + b_k(q_i, t) = 0 \tag{2.8}$$

Note that the constraint influence matrix, C, maps a relationship between the generalized velocities and constraint.

$$C_{kj} = \frac{\partial \dot{\phi}_k}{\partial \dot{q}_j} \tag{2.9}$$

If $\dot{\phi}_k$ is integrable and can be expressed in generalized coordinates, then the constraint is called holonomic and its integrated form can be written $\phi_k(q_j, t)$; otherwise, it is called nonholonomic [9, 11]. In this dissertation, ϕ_k is used to describe both types of constraints.

Redundant coordinate systems are systems for which the number of generalized coordinates used to describe the system are greater than the number of degrees of freedom of the system. For example, if a system has n generalized coordinates and m independent constraints, the system has $n - m$ degrees of freedom [13]. A simple example of a redundant coordinate system is the pendulum in the plane described in cartesian coordinates. Lagrange's equations for constrained systems have the form of

differential algebraic equations.

$$\frac{\mathrm{d}}{\mathrm{dt}}\left(\frac{\partial L}{\partial \dot{q}_j}\right) - \frac{\partial L}{\partial q_j} = C_{kj}\lambda_k + Q_j \tag{2.10}$$

$$\phi_k(\dot{q}_i, q_i, t) = 0 \tag{2.11}$$

Two primary methods exist for instead writing the governing equations as ordinary differential equations. The first involves defining quasi-velocities in a Gibbs/Appell or Kane framework, as discussed in the Ch. III. (Note however, that Lagrange's equations for systems with quasi-velocities do exist [8]). The second method eliminates the Lagrange multipliers in Eq. 2.10 to instead write it as a function of the generalized coordinates, velocities, and forces: $\lambda_k = \lambda_k(\dot{q}_i, q_i, Q_i, t)$. Many methods for eliminating the Lagrange multipliers exist [14]. Some examples include range and null space methods, Maggi's formulation, and Udwadia and Kalaba's formulation. One method that has been shown useful for finding numerical approximations of the Lagrange multipliers for optimal control applications is the Augmented Lagrange method [15]. A range space method, as outlined below, may be tedious for complex systems and result in highly nonlinear differential equations, but it is straightforward.

1. Differentiate the constraint twice with respect to time.
2. Substitute the governing equations into the resulting expression.
3. Solve for the Lagrange multipliers as functions of the coordinates and velocities.
4. Substitute the expressions for the Lagrange multipliers back into the governing equations.

For this dissertation, the range space method is employed to solve for the values of the Lagrange multipliers. However, these expressions may not be directly substituted

back into the equations to retain a clear partition of the constraint forces. Returning to the equations of motion, Eq. 2.10 can be rearranged without loss of generality.

$$M_{jl}(\dot{q}_i, q_i, t)\ddot{q}_l + g_j(\dot{q}_i, q_i, t) = C_{kj}\lambda_k + Q_j \tag{2.12}$$

Again assuming the mass matrix is invertible, this equation can be written in state-vector form.

$$\begin{bmatrix} \dot{q}_j \\ \ddot{q}_j \end{bmatrix} = \begin{bmatrix} \dot{q}_j \\ M_{lj}^{-1}(\dot{q}_i, q_i, t)\left[-g_l(\dot{q}_i, q_i, t) + C_{kl}\lambda_k + Q_l\right] \end{bmatrix} \tag{2.13}$$

Defining x_i as before, and successfully solving for the Lagrange multipliers, these equations can be written in first-order form.

$$\dot{x}_i = f_i(x_j, \lambda_k, Q_j, t) = f_i(x_j, Q_j, t) \tag{2.14}$$

These governing equations are employed in two chapters of this dissertation in the form that retains λ_k as an argument to allow both numerical approximations and analytical solutions of the Lagrange multipliers to be implemented.

4. Infinite-Dimensional Systems

Continuous and hybrid dynamical systems are those which include a coordinate that is a function of both space and time, $\mathbf{w}(x, t)$, called an infinite-dimensional (or "continuous" or "distributed parameter") coordinate [7]. A hybrid system also includes a discrete generalized coordinate, $q(t)$, in the kinematic description. An aerospace example of a hybrid dynamical system is a satellite composed of a rigid hub and a flexible appendage. This class of systems can be modeled from first principles using the extended Hamilton's principle or this Lagrangian approach, and there exists a distinction between those that have a single or multiple flexible bodies [7, 16]. The

resulting equations of motion for hybrid systems are generally integro-partial differential equations, which include terms in which the continuous coordinate is (1) differentiated with respect to time, (2) differentiated with respect to space, and (3) integrated with respect to space. The first two of these characteristics are attributes of partial differential equations, whereas the third is indicative of integro-differential equations.

An outline of Lagrange's equations for hybrid systems now follows [16]. In this work, the class of systems considered have $i = 1 \ldots n$ discrete coordinates q_i and $j = 1 \ldots m$ continuous coordinates $\mathbf{w}_j$, and the strain energy terms, $\mathbf{w}'_j$ and $\mathbf{w}''_j$, are assumed to belong only to the potential energy function. Each prime on the continuous coordinate represents differentiation with respect to the spacial domain (x). The Lagrangian is formed with up to three distinct parts related to the coordinate classification (discrete, infinite, boundary, or a combination thereof). A further distinction is made between systems that contain a single elastic domain (a) or multiple elastic domains (b). This division is chosen because coupling between multiple domains must be taken into account, starting with the Lagrangian.

$$(a) \quad \mathcal{L} = L_D + \int_{l_0}^{l} \widehat{L} \mathrm{d}x + L_B \qquad \text{Single Elastic Domain} \qquad (2.15)$$

$$(b) \quad \mathcal{L} = L_D + \mathcal{L}_B \qquad \text{Multiple Elastic Domains} \qquad (2.16)$$

Each of these terms are defined below using the following argument lists.

$L_D = T_D - V_D = L_D(\boldsymbol{q}, \dot{\boldsymbol{q}}, t)$	Discrete Lagrangian
$\widehat{L} = \widehat{T} - \widehat{V} = \widehat{L}(\boldsymbol{q}, \dot{\boldsymbol{q}}, \mathbf{w}, \dot{\mathbf{w}}, \mathbf{w}', \mathbf{w}'', x, t)$	Single Elastic Domain Continuous Lagrangian
$\widehat{L}^i = \widehat{T}^i - \widehat{V}^i = \widehat{L}(\boldsymbol{q}, \dot{\boldsymbol{q}}, \mathbf{w}_i, \dot{\mathbf{w}}_i, \mathbf{w}_i{}', \mathbf{w}_i{}'', \underline{\mathbf{w}}(\underline{\boldsymbol{l}}), \underline{\dot{\mathbf{w}}}(\underline{\boldsymbol{l}}), \underline{\mathbf{w}}'(\underline{\boldsymbol{l}}), \underline{\dot{\mathbf{w}}}'(\underline{\boldsymbol{l}}), x_i, t)$	Multiple Elastic Domains Continuous Lagrangian
$L_B = T_B - V_B = L_B(\boldsymbol{q}, \dot{\boldsymbol{q}}, \mathbf{w}(l), \dot{\mathbf{w}}(l), \mathbf{w}'(l), \dot{\mathbf{w}}'(l), t)$	Single Elastic Domain Boundary Lagrangian
$\mathcal{L}_B = L_B(\boldsymbol{q}, \dot{\boldsymbol{q}}, \underline{\mathbf{w}}(\underline{\boldsymbol{l}}), \underline{\dot{\mathbf{w}}}(\underline{\boldsymbol{l}}), \underline{\mathbf{w}}'(\underline{\boldsymbol{l}}), \underline{\dot{\mathbf{w}}}'(\underline{\boldsymbol{l}}), t) + \sum_{i=1}^{n} \int_{l_{0i}}^{l_i} \widehat{L}^i \mathrm{d}x_i$	Multiple Elastic Domains Boundary Lagrangian

The first expression of Lagrange's equations for hybrid systems, which governs the discrete coordinates, resembles the form of Eq. 2.4.

$$\frac{\mathrm{d}}{\mathrm{d}t}\left(\frac{\partial \mathcal{L}}{\partial \dot{q}_i}\right) - \frac{\partial \mathcal{L}}{\partial q_i} = Q_i \tag{2.17}$$

The second expression of the equations, which governs the continuous coordinates, clearly accounts for change with respect to the spatial domain.

$$(a) \quad \frac{\mathrm{d}}{\mathrm{d}t}\left(\frac{\partial \widehat{L}}{\partial \dot{\mathbf{w}}}\right) - \frac{\partial \widehat{L}}{\partial \mathbf{w}} + \frac{\mathrm{d}}{\mathrm{d}x}\left(\frac{\partial \widehat{L}}{\partial \mathbf{w}'}\right) - \frac{\mathrm{d}^2}{\mathrm{d}x^2}\left(\frac{\partial \widehat{L}}{\partial \mathbf{w}''}\right) = \widehat{\mathbf{f}}^T \tag{2.18}$$

$$(b) \quad \frac{\mathrm{d}}{\mathrm{d}t}\left(\frac{\partial \widehat{L}^i}{\partial \dot{\mathbf{w}}_i}\right) - \frac{\partial \widehat{L}^i}{\partial \mathbf{w}_i} + \frac{\mathrm{d}}{\mathrm{d}x_i}\left(\frac{\partial \widehat{L}^i}{\partial \mathbf{w}_i'}\right) - \frac{\mathrm{d}^2}{\mathrm{d}x_i^2}\left(\frac{\partial \widehat{L}^i}{\partial \mathbf{w}_i''}\right) = \widehat{\mathbf{f}}^{iT} \tag{2.19}$$

Because the equations include differentiation with respect to space, boundary conditions are needed. These equations are also derived from the extended Hamilton's

principle [16].

$$(a)\quad \left\{\frac{\partial \widehat{L}}{\partial \mathbf{w}'}-\frac{\mathrm{d}}{\mathrm{d}x}\left(\frac{\partial \widehat{L}}{\partial \mathbf{w}''}\right)\right\}\delta\mathbf{w}\Big|_{l_0}^{l}+\left\{\frac{\partial L_B}{\partial \mathbf{w}(l)}-\frac{\mathrm{d}}{\mathrm{d}t}\left(\frac{\partial L_B}{\partial \dot{\mathbf{w}}(l)}\right)\right\}\delta\mathbf{w}(l)$$

$$+\mathbf{f}_1^T\delta\mathbf{w}(l)=0 \tag{2.20}$$

$$\frac{\partial \widehat{L}}{\partial \mathbf{w}''}\delta\mathbf{w}'\Big|_{l_0}^{l}+\left\{\frac{\partial L_B}{\partial \mathbf{w}'(l)}-\frac{\mathrm{d}}{\mathrm{d}t}\left(\frac{\partial L_B}{\partial \dot{\mathbf{w}}'(l)}\right)\right\}\delta\mathbf{w}'(l)+\mathbf{f}_2^T\delta\mathbf{w}'(l)=0 \tag{2.21}$$

$$(b)\quad \left\{\frac{\partial \widehat{L}^i}{\partial \mathbf{w}_i'}-\frac{\mathrm{d}}{\mathrm{d}x_i}\left(\frac{\partial \widehat{L}^i}{\partial \mathbf{w}_i''}\right)\right\}\delta\mathbf{w}_i\Big|_{l_{0i}}^{l_i}+\left\{\frac{\partial \mathcal{L}_B}{\partial \mathbf{w}_i(l_i)}-\frac{\mathrm{d}}{\mathrm{d}t}\left(\frac{\partial \mathcal{L}_B}{\partial \dot{\mathbf{w}}_i(l_i)}\right)\right\}\delta\mathbf{w}_i(l_i)$$

$$+\mathbf{f}_1^{iT}\delta\mathbf{w}_i(l_i)=0 \tag{2.22}$$

$$\frac{\partial \widehat{L}^i}{\partial \mathbf{w}_i''}\delta\mathbf{w}_i'\Big|_{l_{0i}}^{l_i}+\left\{\frac{\partial \mathcal{L}_B}{\partial \mathbf{w}_i'(l_i)}-\frac{\mathrm{d}}{\mathrm{d}t}\left(\frac{\partial \mathcal{L}_B}{\partial \dot{\mathbf{w}}_i'(l_i)}\right)\right\}\delta\mathbf{w}_i'(l_i)+\mathbf{f}_2^{iT}\delta\mathbf{w}_i'(l_i)=0 \tag{2.23}$$

For hybrid systems with a single elastic domain, Eqs. 2.17, 2.18, 2.20 and 2.21 are implemented, whereas Eqs. 2.17, 2.19, 2.22 and 2.23 are used for those with multiple continuous coordinates. There is not a straightforward method for transforming these IPDEs into an ODE form, but finite-dimensional approximations do exist and are discussed further in Ch. VI.

B. Continuous-Discrete Extended Kalman Filter

Sequential estimation algorithms provide a means for estimating parameters or states of a dynamical system in real-time. The most commonly-used sequential estimation method is the Kalman filter [4]. Several formulations of the Kalman filter exist; here, an estimation algorithm for nonlinear systems modeled with differential equations and discrete measurements is utilized called the continuous-discrete extended Kalman filter [1]. Let $\tilde{\boldsymbol{y}}_k$ be the measurement vector, $\hat{\boldsymbol{x}}$ be the state estimate vector, and $\tilde{\boldsymbol{x}}$ be the error between the state estimates and true states. Unbiased Gaussian measurement noise, $\boldsymbol{v}_k$, and process noise, $\boldsymbol{w}(t)$, is assumed with respective covariance matrices R_k and $Q(t)$. Initializing with state estimate $\hat{\boldsymbol{x}}(t_0)=\hat{\boldsymbol{x}}_0$ and state

covariance matrix $P_0 = E\{\tilde{\boldsymbol{x}}(t_0)\tilde{\boldsymbol{x}}^T(t_0)\}$, the following estimation algorithm can be employed. Note that the system model is assumed to be a continuous, nonlinear ordinary differential equation in this formulation.

System Model

$$\dot{\boldsymbol{x}}(t) = \boldsymbol{f}(\boldsymbol{x}(t), \boldsymbol{u}(t), t) + G(t)\boldsymbol{w}(t) \tag{2.24}$$

Measurement Model

$$\tilde{\boldsymbol{y}}_k = \boldsymbol{h}_k(\boldsymbol{x}_k) + \boldsymbol{v}_k \tag{2.25}$$

Gain Equation

$$K_k = P_k^- H_k^T(\hat{\boldsymbol{x}}_k^-)\left[H_k(\hat{\boldsymbol{x}}_k^-)P_k^- H_k^T(\hat{\boldsymbol{x}}_k^-) + R_k\right]^{-1} \tag{2.26}$$

State Estimate Update

$$\hat{\boldsymbol{x}}_k^+ = \hat{\boldsymbol{x}}_k^- + K_k[\tilde{\boldsymbol{y}} - \boldsymbol{h}(\hat{\boldsymbol{x}}_k^-)] \tag{2.27}$$

State Covariance Matrix Update

$$P_k^+ = [I - K_k H_k(\hat{\boldsymbol{x}}_k^-)]P_k^- \tag{2.28}$$

State Estimate Propagation Equation

$$\dot{\hat{\boldsymbol{x}}} = \boldsymbol{f}(\hat{\boldsymbol{x}}(t), \boldsymbol{u}(t), t) \tag{2.29}$$

State Covariance Matrix Propagation Equation

$$\dot{P}(t) = F(\hat{\boldsymbol{x}}(t), t)P(t) + P(t)F^T(\hat{\boldsymbol{x}}(t), t) + G(t)Q(t)G^T(t) \tag{2.30}$$

Here, the measurement and state matrices, $H_k(\hat{\boldsymbol{x}}_k^-)$ and $F(\hat{\boldsymbol{x}}(t), t)$, matrices are defined as follows.

$$H_k(\hat{\boldsymbol{x}}_k^-) = \left.\frac{\partial \boldsymbol{h}}{\partial \boldsymbol{x}}\right|_{\hat{\boldsymbol{x}}_k^-} \quad ; \quad F(\hat{\boldsymbol{x}}(t), t) = \left.\frac{\partial \boldsymbol{f}}{\partial \boldsymbol{x}}\right|_{\hat{\boldsymbol{x}}(t)} \tag{2.31}$$

This basic structure of the estimation algorithm is utilized throughout this dissertation, but the emphasis of the work lies primarily in the state estimate propagation equation, Eq. 2.29, and the related form of the state matrix F in Eq. 2.31.

CHAPTER III

DIRECT LINEARIZATION VIA THE GIBBS FUNCTION*

The linearized form of governing equations is desirable for system stability analysis and control design, primarily because the tools available for analyzing a linear system are far greater in number than those for nonlinear systems. These equations are also useful in estimation, where a number of algorithms for linear systems are available, including the original Kalman filter [2, 3]. The extension to estimation of the direct linearization ideas presented in this chapter is more fully discussed in Ch. VII.

Usually, linearization of the equations of motion about a point of interest, such as an equilibrium point, is performed using a Taylor series approximation or perturbation methods [17, 18]. These are indirect methods because they require first deriving the full, nonlinear equations of motion before forming the linearized approximations. Direct linearization, however, produces the linearized equations directly from a kinematic-based scalar function. Existing direct linearization methods employ the Lagrangian function for both finite and infinite-dimensional systems [9, 19]. For applications where the nonlinear equations are unnecessary, these direct methods are advantageous because they do not involve forming the nonlinear equations and, as a result, are generally significantly less computationally expensive. Note that a linear representation of nonlinear motion may not capture all of the relevant motion of a system, but often serves as a useful approximation. For example, the motion of a system about an equilibrium point can usually be characterized as linear, and stability information can be derived from this approximation [7, 8].

In this chapter, a direct linearization method via the Gibbs function, rather than via the Lagrangian, is presented. One of the additional advantages of the direct method via Lagrange's equations is that they are able to handle holonomic constraints. The interest in linearization via the Gibbs function is likewise related to its ability to also handle nonholonomic constraints [9]. Furthermore, the resulting set of equations includes only first-order equations, and the quasi-velocities employed in the equations, such as angular velocities, are often of physical interest.

It is important to also note the relation of the Gibbs and Appell equations to Kane's equations. When the Gibbs and Appell equations are derived using partial velocities, it can be shown that the kinetic equations that result from using virtual work and the Gibbs function are identical to those formed using Kane's equations [9]. Furthermore, Kane outlines a method for direct linearization of Kane's equations. However, our work is differentiated from the Kanian method in two significant ways. First, the method presented here utilizes an operator on a single scalar function, as opposed to a set of vector equations. Second, this operator simultaneously linearizes both the potential forces and kinematic-based terms in the governing equations, whereas Kane's approach uses a series of linearization steps, some of which employ linearization by inspection [20, 21]. A further discussion of the two methods of linearization is later presented.

A. The Gibbs Function

The Gibbs equations (later independently published by Appell) derive the equations of motion (here, for a point mass) from a scalar function, $S(q_i, \eta_j, \dot{\eta}_j)$, where q_i are the n generalized coordinates, η_j are the m quasi-velocities (also called generalized speeds), and $\dot{\eta}_j$ are the m time derivatives of these velocities [22, 23]. The quasi-velocities are related to the generalized velocities by the equation $\dot{q}_i = A_{ij}\eta_j$, where

A is a function of the generalized coordinates and time, $A = A(q_i, t)$. The velocity vector can then be written as a linear function of the quasi-velocities.

$$\boldsymbol{v} = \frac{\partial \boldsymbol{v}}{\partial \eta_j}\eta_j + \boldsymbol{v}_0 = \eta_j \boldsymbol{\tau}_j + \boldsymbol{v}_0 \tag{3.1}$$

The acceleration vector is the time derivative of the velocity vector.

$$\boldsymbol{a} = \eta_j \dot{\boldsymbol{\tau}}_j + \dot{\eta}_j \boldsymbol{\tau}_j + \boldsymbol{a}_0 \tag{3.2}$$

Much like the Lagrangian function is built on velocity-level kinematics, the Gibbs function (sometimes called the Appellian) is built on acceleration-level kinematics.

$$S = \frac{1}{2} m \left(\boldsymbol{a} \cdot \boldsymbol{a} \right) \tag{3.3}$$

The kinetic equations of motion can then be derived from the following [9].

$$\frac{\partial S}{\partial \dot{\eta}_i} = U_i \tag{3.4}$$

Here, U_i are generalized forces, where $\boldsymbol{F}$ are the forces acting on the system. One can find these forces using the Kanian approach, $U_i = \boldsymbol{\tau}_i \cdot \boldsymbol{F}$, or using virtual work, as did Gibbs. In this chapter, linearization of terms arising from the kinematics is of concern, with the assumption that the forces U_i arise from either potential forces or control forces. Also note that, as an alternative to first evaluating the dot product and then differentiating, one can instead differentiate S implicitly and use $\partial S / \partial \dot{\eta}_i = m \left(\boldsymbol{a} \cdot \partial \boldsymbol{a} / \partial \dot{\eta}_i \right)$ [24].

If the system is a rotating rigid body, then the rotational motion must be accounted for in the Gibbs function, just as it is in the Lagrangian. The angular velocity vector, $\boldsymbol{\omega} = (\partial \boldsymbol{\omega} / \partial \eta_j)\eta_j + \boldsymbol{\omega}_0 = \eta_j \tilde{\boldsymbol{\tau}}_j + \boldsymbol{\omega}_0$, and angular acceleration vector, $\boldsymbol{\alpha} = \dot{\boldsymbol{\omega}}$, are needed [9]. The Gibbs function for rigid bodies is composed of translational and

rotational terms.

$$S = \frac{1}{2} m \left(\boldsymbol{a}_c \cdot \boldsymbol{a}_c \right) + \frac{1}{2} \left(\boldsymbol{\alpha} \cdot \boldsymbol{I}_c \boldsymbol{\alpha} \right) + \boldsymbol{\alpha} \cdot \left(\boldsymbol{\omega} \times \boldsymbol{I}_c \boldsymbol{\omega} \right) \tag{3.5}$$

Here, $\boldsymbol{a}_c$ is the acceleration of the mass center and $\boldsymbol{I}_c$ is the rigid body inertia tensor about the mass center. Equation 3.4 can then be utilized by augmenting the generalized forces to include moments about the mass center (pure moments or moments due to forces) using virtual work or using $U_i = \boldsymbol{\tau}_i \cdot \boldsymbol{F} + \tilde{\boldsymbol{\tau}}_i \cdot \boldsymbol{M}$. These equations provide the full set of first order differential equations for the system when coupled with the kinematic differential equations that relate the quasi-velocities to the generalized velocities, $\dot{q}_i = A_{ij} \eta_j$ [8, 11].

1. Example 1a: Planar Vehicle

As an illustrative example, consider the classic problem of a sled, a system that has a non-holonomic constraint that prevents a sideslip velocity [9]. That is, the sled can move forward or rotate, but cannot move side to side. The sled has mass m and inertia I about the center of mass, located at the sled's rear axle midpoint. Forces F_1 and F_2 act along the sled and perpendicular to the sled, and a torque, u rotates the sled. The system can move in the plane with generalized coordinates $\{x, y, \theta\}$, where θ is the heading angle, as shown in Fig. 1.

If the $\boldsymbol{b}$ frame is chosen to be body-fixed with $\hat{\boldsymbol{b}}_1$ along the forward direction of the sled and $\hat{\boldsymbol{b}}_2$ perpendicular to the motion of the sled, the velocity in the $\hat{\boldsymbol{b}}_2$ direction is zero, i.e. $\boldsymbol{v} = \dot{x}\hat{\boldsymbol{n}}_1 + \dot{y}\hat{\boldsymbol{n}}_2 = v_1 \hat{\boldsymbol{b}}_1$. However, if the velocity vector is written in the body frame, it is $\boldsymbol{v} = \left(\dot{x} \cos\theta + \dot{y} \sin\theta \right) \hat{\boldsymbol{b}}_1 + \left(\dot{y} \cos\theta - \dot{x} \sin\theta \right) \hat{\boldsymbol{b}}_2$. Equating the two expressions for the velocity, the nonholonomic constraint can then be found and written in Pfaffian form: $\phi = \dot{y} \cos\theta - \dot{x} \sin\theta = 0$.

The problem is first solved using Lagrange's equations for constrained systems.

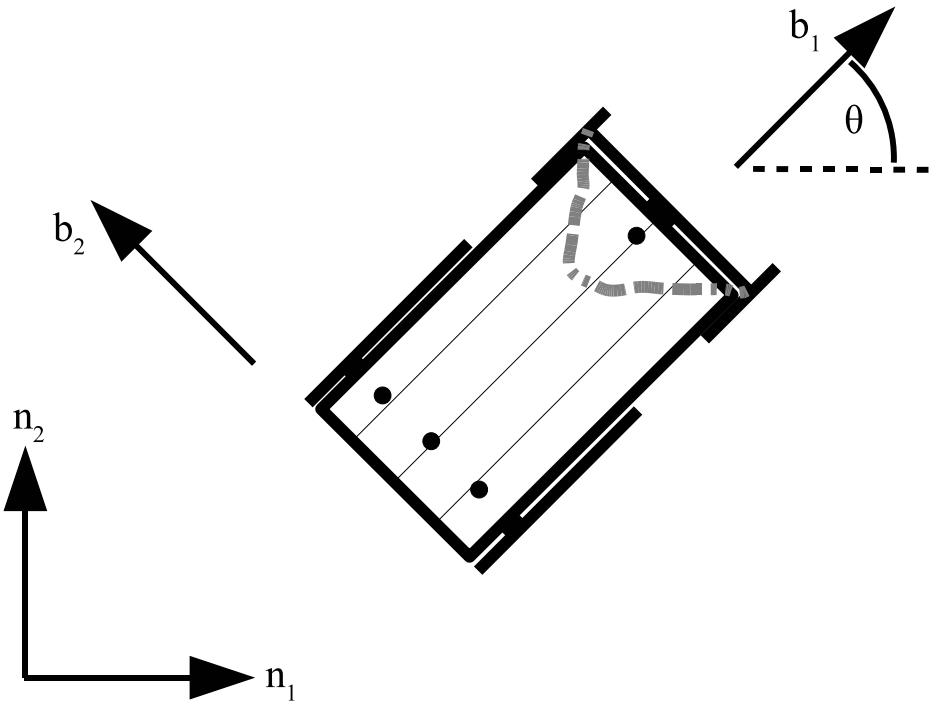

Fig. 1. Planar Vehicle (Sled) Illustration.

For this example, the Lagrangian is $L = 1/2m\,(\dot{x}^2 + \dot{y}^2) + 1/2I\dot{\theta}^2$ and the constraint influence matrix is $C = [\partial\phi/\partial\dot{x}, \partial\phi/\partial\dot{y}, \partial\phi/\partial\dot{\theta}]^T = [-\sin\theta, \cos\theta, 0]^T$. Applying Eq. 2.10, the resulting equations and constraint are a 7th order system of differential algebraic equations.

$$\begin{aligned} m\ddot{x} &= F_1\cos\theta - F_2\sin\theta - \lambda\sin\theta \\ m\ddot{y} &= F_1\sin\theta + F_2\cos\theta + \lambda\cos\theta \\ I\ddot{\theta} &= u \end{aligned} \tag{3.6}$$

Solving for the Lagrange multiplier, $\lambda = -F_2$, these equations can be reduced to the

following set of 6th order ordinary differential equations.

$$\begin{aligned} m\ddot{x} &= F_1 \cos\theta \\ m\ddot{y} &= F_1 \sin\theta \\ I\ddot{\theta} &= u \end{aligned} \tag{3.7}$$

If, instead, quasi-velocities are used to describe the system motion with $\boldsymbol{v} = \eta_1 \hat{\boldsymbol{b}}_1 + \eta_2 \hat{\boldsymbol{b}}_2 = (\dot{x}\cos\theta + \dot{y}\sin\theta)\,\hat{\boldsymbol{b}}_1 + (\dot{y}\cos\theta - \dot{x}\sin\theta)\,\hat{\boldsymbol{b}}_2$ and $\boldsymbol{\omega} = \eta_3 \hat{\boldsymbol{b}}_3 = \dot{\theta}\hat{\boldsymbol{b}}_3$, the system can be further reduced. Using these relationships, the generalized velocities and quasi-velocities can be related with the following equations.

$$\begin{bmatrix} \dot{x} \\ \dot{y} \\ \dot{\theta} \end{bmatrix} = \begin{bmatrix} \cos\theta & -\sin\theta & 0 \\ \sin\theta & \cos\theta & 0 \\ 0 & 0 & 1 \end{bmatrix} \begin{bmatrix} \eta_1 \\ \eta_2 \\ \eta_3 \end{bmatrix} \tag{3.8}$$

Recall that the velocity in the $\boldsymbol{b}_2$ direction is zero due to the constraint, so $\eta_2 = 0$. With this information and substitution of the quasi-velocities, the system of equations reduces to a 5th order system of first order ordinary differential equations.

$$\begin{aligned} \dot{x} &= \eta_1 \cos\theta \\ \dot{y} &= \eta_1 \sin\theta \\ \dot{\theta} &= \eta_3 \\ \dot{\eta}_1 &= F_1/m \\ \dot{\eta}_3 &= u/I \end{aligned} \tag{3.9}$$

Now the problem is revisited with a Gibbs-Appell approach. Using the same quasi-velocity kinematic description (such that $\boldsymbol{v} = \eta_1 \hat{\boldsymbol{b}}_1$ ($\eta_2 \hat{\boldsymbol{b}}_2 = 0$) and $\boldsymbol{\omega} = \eta_3 \hat{\boldsymbol{b}}_3$ ($= \dot{\theta}\hat{\boldsymbol{b}}_3$)), the translational acceleration vector is $\boldsymbol{a} = \dot{\eta}_1 \hat{\boldsymbol{b}}_1 + \eta_1 \eta_3 \hat{\boldsymbol{b}}_2$ and the angular

acceleration vector is $\boldsymbol{\alpha} = \dot{\eta}_3 \hat{\boldsymbol{b}}_3$. The Gibbs function can then be constructed.

$$S = \frac{1}{2} m \left(\dot{\eta}_1^2 + \eta_1^2 \eta_3^2 \right) + \frac{1}{2} I \dot{\eta}_3^2 \tag{3.10}$$

Applying Eq. 3.4, the following kinetic equations can be found.

$$\frac{\partial S}{\partial \dot{\eta}_1} = m \dot{\eta}_1 = F_1 \quad ; \quad \frac{\partial S}{\partial \dot{\eta}_3} = I \dot{\eta}_3 = u \tag{3.11}$$

The kinematic differential equations relating the generalized velocities to the quasi-velocities then complete the set of first order differential equations.

$$\begin{aligned} \dot{x} &= \eta_1 \cos\theta \\ \dot{y} &= \eta_1 \sin\theta \\ \dot{\theta} &= \eta_3 \end{aligned} \tag{3.12}$$

These equations represent the full, nonlinear system of equations. If one were interested in linearizing them about an equilibrium point, such as $\{\eta_i = 0, q_i = q_i^*\}$, a Taylor series expansion could be used to find the following system of equations (for perturbations of the variables from equilibrium).

$$\begin{aligned} \dot{x} &= \eta_1 \cos\theta^* \\ \dot{y} &= \eta_1 \sin\theta^* \\ \dot{\theta} &= \eta_3 \\ \dot{\eta}_1 &= F_1/m \\ \dot{\eta}_3 &= u/I \end{aligned} \tag{3.13}$$

Next, a method for generating these equations directly from the function S, bypassing the full nonlinear equations, is presented.

B. Direct Linearization via the Gibbs Function

Existing Lagrangian-view direct linearization methods are developed by linearizing the generalized, fully nonlinear equations once and for all. That is, a Taylor series expansion is applied to the general form of the equations of motion and first order terms are retained [9, 19]. In the following derivation, the expansion is assumed to about an equilibrium point, q_i^*, such that $\eta_i = \dot{\eta}_i = 0$ at equilibrium with no nonpotential forces acting. (Note that direct linearization about a trajectory requires some additional computation.) Also, without loss of generality, a change of variables is employed such that $\boldsymbol{q}_{new} = \boldsymbol{q}_{old} - \boldsymbol{q}^*$. The simple form of Eq. 3.4 eases the expansion.

$$U_i = \frac{\partial S}{\partial \dot{\eta}_i} \approx \frac{\partial}{\partial \dot{\eta}_j}\left(\frac{\partial S}{\partial \dot{\eta}_i}\right)\bigg|_{eq} \dot{\eta}_j + \frac{\partial}{\partial \eta_j}\left(\frac{\partial S}{\partial \dot{\eta}_i}\right)\bigg|_{eq} \eta_j + \frac{\partial}{\partial q_j}\left(\frac{\partial S}{\partial \dot{\eta}_i}\right)\bigg|_{eq} q_j + \dots \tag{3.14}$$

This expression can be further simplified by partitioning S in the following manner.

$$\begin{aligned} S =& s_{2_{ij}}(q_k, \eta_p)\dot{\eta}_i\dot{\eta}_j + \left(s_{1a_i}(q_k, \eta_p) + s_{1b_i}(q_k)\right)\dot{\eta}_i + s_0 \\ =& S_2 + S_1 + S_0 = S_2 + S_{1a} + S_{1b} + S_0 \end{aligned} \tag{3.15}$$

Note that S_2 and S_1 are respectively quadratic and linear in the time derivatives of the quasi-velocities, whereas S_0 has no dependence on $\dot{\eta}_j$. The term S_1 can then be partitioned into S_{1a}, which contains the quasi-velocities, and S_{1b}, which does not. Using this partitioning, the full set of linearized equations can then be written in a straightforward manner using Eq. 3.14, along with the linearized kinematic differential equations.

$$U_i = m_{ij}\dot{\eta}_j + z_{ij}\eta_j + k_{ij}q_j \quad ; \quad \dot{q}_i = a_{ij}\eta_j \tag{3.16}$$

$$m_{ij} = \frac{\partial^2 S_2}{\partial \dot{\eta}_i \partial \dot{\eta}_j}\bigg|_{eq} \quad ; \quad z_{ij} = \frac{\partial^2 S_{1a}}{\partial \dot{\eta}_i \partial \eta_j}\bigg|_{eq} \quad ; \quad k_{ij} = \frac{\partial^2 S_{1b}}{\partial \dot{\eta}_i \partial q_j}\bigg|_{eq} \quad ; \quad a_{ij} = A_{ij}|_{eq} \tag{3.17}$$

This set of equations allows one to construct the translational and angular acceleration vectors, and subsequently S, and then find three partial derivative matrices to directly

arrive at the linearized equations of motion.

The generalized forces of Eq. 3.16 represent linearized generalized forces. That is, if these forces depend on the configuration- or velocity-level motion variables, such as potential forces, then they too must be linearized. Rather than linearizing terms related to the kinematics in one step, and those related to the potential forces in another, it is desired to linearize both in a single computation. Hence, an augmented Gibbs function is desirable.

C. Direct Linearization via Augmented Gibbs Function

The Lagrangian function augments the kinetic energy with a potential energy term, allowing the potential forces to be separated from the nonpotential forces. Similarly, a form of the Gibbs function that captures both the kinetic and potential energy of the system is desirable. This augmented function can be constructed by using forms of the definition of virtual work to allow the potential forces to participate in the Gibbs-Appell framework.

First consider the definition of a potential force P_i, a force derived from the gradient of a potential V, the potential energy of the system [8, 11, 25].

$$P_i = -\frac{\partial V}{\partial q_i} \tag{3.18}$$

In the Lagrangian view, the virtual work of the forces is $\delta W = (Q_i + P_i)\delta q_i$, where Q_i are the nonpotential forces [8, 11, 25]. Similarly, from the Gibbs-Appell view, the virtual work can be written $\delta W = U_j \delta\theta_j = (U_j^P + U_j^N)\delta\theta_j$. Here, $\delta\theta_j$ are virtual displacements of the quasi-coordinates. The total force, U_j, is partitioned into parts derived from potential (P) and nonpotential (N) forces. Equating the contributions

of the potential forces to the virtual work, the following relationship emerges.

$$\delta W^P = P_i \delta q_i = -\frac{\partial V}{\partial q_i}\delta q_i = -\frac{\partial V}{\partial q_i} A_{ij}\delta\theta_j = U_j^P \delta\theta_j \tag{3.19}$$

This relationship begets an expression for the potential forces from the Gibbs-Appell perspective: $U_j^P = -\frac{\partial V}{\partial q_i}A_{ij}$. Moving this portion of Eq. 3.4 to the left hand side of the equation, a new form of the Gibbs function, the augmented Gibbs function, and its associated equations of motion can be formed.

$$\tilde{S} = S + \frac{\partial V}{\partial q_i} A_{ij}\dot{\eta}_j \tag{3.20}$$

$$\frac{\partial \tilde{S}}{\partial \dot{\eta}_i} = U_i^N \tag{3.21}$$

Furthermore, in a similar manner as before, these equations can be directly linearized.

$$U_i^N = m_{ij}\dot{\eta}_j + z_{ij}\eta_j + k_{ij}q_j \quad ; \quad \dot{q}_i = a_{ij}\eta_j \tag{3.22}$$

$$m_{ij} = \left.\frac{\partial^2 \tilde{S}_2}{\partial\dot{\eta}_i \partial\dot{\eta}_j}\right|_{eq} \quad ; \quad z_{ij} = \left.\frac{\partial^2 \tilde{S}_{1a}}{\partial\dot{\eta}_i \partial\eta_j}\right|_{eq} \quad ; \quad k_{ij} = \left.\frac{\partial^2 \tilde{S}_{1b}}{\partial\dot{\eta}_i \partial q_j}\right|_{eq} \quad ; \quad a_{ij} = A_{ij}|_{eq} \tag{3.23}$$

This version of the directly linearized equations accounts for linearization of both the kinematic contribution and the potential force contribution to the equations of motion. Note that the equilibrium point of the system, neglecting nonpotential forces, can be found by solving the following equation for q_i^* with $\eta_i = \dot{\eta}_i = 0$.

$$\frac{\partial \tilde{S}_{1b}}{\partial \dot{\eta}_i} = 0 \tag{3.24}$$

The separation of the nonpotential and potential forces is common in Lagrangian formulations, and here it useful also because the dynamic potential, which includes the potential energy, is often used to find the equilibrium point.

1. Example 1b: Planar Vehicle

Recall the example of the sled of Fig. 1. Now also consider two potential forces acting on the system arising from nonlinear springs connected to the mass center such that $\boldsymbol{F} = -kx^3\hat{\boldsymbol{n}}_1 - ky^3\hat{\boldsymbol{n}}_2$. These forces can be derived from the potential energy function, $V = k(x^4 + y^4)/4$. From Eq. 3.20, the augmented Gibbs function can be constructed.

$$\tilde{S} = S + \frac{\partial V}{\partial q_i} A_{ij}\dot{\eta}_j = \frac{1}{2}m\left(\dot{\eta}_1^2 + \eta_1^2\eta_3^2\right) + \frac{1}{2}I\dot{\eta}_3^2 + \begin{bmatrix} kx^3 & ky^3 & 0 \end{bmatrix} \begin{bmatrix} \cos\theta & 0 \\ \sin\theta & 0 \\ 0 & 1 \end{bmatrix} \begin{bmatrix} \dot{\eta}_1 \\ \dot{\eta}_3 \end{bmatrix}$$

$$= \frac{1}{2}m\left(\dot{\eta}_1^2 + \eta_1^2\eta_3^2\right) + \frac{1}{2}I\dot{\eta}_3^2 + \dot{\eta}_1\left(kx^3\cos\theta + ky^3\sin\theta\right) \tag{3.25}$$

Note that the additional terms in the parenthetical are precisely the potential force contributions in the $\hat{\boldsymbol{b}}_1$ direction. Furthermore, the partitioning of $\tilde{S}$ is apparent: $\tilde{S}_2 = 1/2\, m\dot{\eta}_1^2 + 1/2\, I\dot{\eta}_3^2$, $\tilde{S}_{1a} = 0$, and $\tilde{S}_{1b} = \dot{\eta}_1\left(kx^3\cos\theta + ky^3\sin\theta\right)$. Applying direct linearization with Eqs. 3.22 and 3.23, the complete set of first-order linearized equations can be formed for $x, y, \theta, \eta_1, \eta_3$.

$$m_{ij} = \begin{bmatrix} m & 0 \\ 0 & I \end{bmatrix} \quad ; \quad z_{ij} = \begin{bmatrix} 0 & 0 \\ 0 & 0 \end{bmatrix} \quad ; \quad a_{ij} = \begin{bmatrix} \cos\theta^* & 0 \\ \sin\theta^* & 0 \\ 0 & 1 \end{bmatrix}$$

$$k_{ij} = \begin{bmatrix} 3kx^{*2}\cos\theta^* & 3ky^{*2}\sin\theta^* & \left(-kx^{*3}\sin\theta^* + ky^{*3}\cos\theta^*\right) \\ 0 & 0 & 0 \end{bmatrix} \tag{3.26}$$

Once the partial derivatives are found, these matrices are directly substituted into Eq. 3.22 to yield the linearized equations.

$$\begin{aligned}
\dot{x} =& \eta_1 \cos\theta^* \\
\dot{y} =& \eta_1 \sin\theta^* \\
\dot{\theta} =& \eta_3 \\
m\dot{\eta}_1 + (3kx^{*2}\cos\theta^*)x + (ky^{*2}\sin\theta^*)y + (-kx^{*3}\sin\theta^* + ky^{*3}\cos\theta^*)\theta =& F_1 \\
I\dot{\eta}_3 =& u
\end{aligned} \tag{3.27}$$

Note that these are the same linearized equations obtained in the original example, except with potential forces acting on the system. However, rather than forming the full nonlinear equations first and then individually linearizing both the kinematic and potential force contributions, the linearized equations are formed directly from the kinematics via the augmented Gibbs function.

2. Example 2: Complex Spacecraft

A more complicated example is now considered: the system from Kane and Levinson's "Formulation of Equations of Motion for Complex Spacecraft" [26]. The spacecraft B in Fig. 2 has mass M, and is connected to an internal point P of mass m through a link system. The forces acting on the system include the external forces acting on P, the external forces acting on B, the external torques acting on B, a spring/damper force acting between P and the link system, and a spring/damper torque acting between the links of the link system.

The spacecraft (and body-fixed frame $\boldsymbol{b}$) rotates with the following angular velocity.

$$\boldsymbol{\omega}_{B/N} = \omega_1\hat{\boldsymbol{b}}_1 + \omega_2\hat{\boldsymbol{b}}_2 + \omega_3\hat{\boldsymbol{b}}_3 = u_1\hat{\boldsymbol{b}}_1 + u_2\hat{\boldsymbol{b}}_2 + u_3\hat{\boldsymbol{b}}_3 \tag{3.28}$$

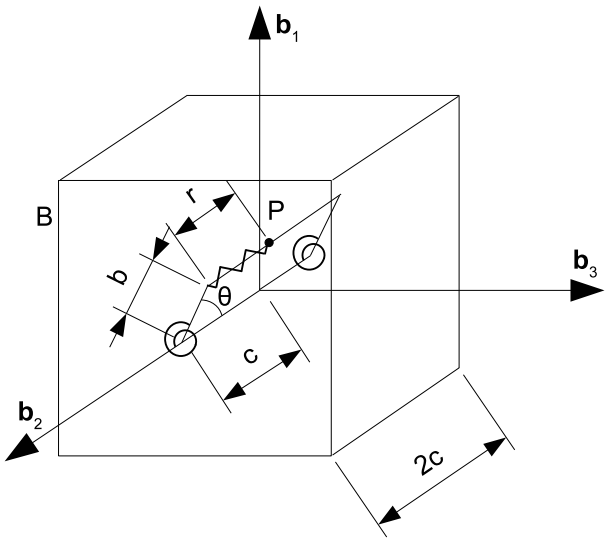

Fig. 2. Complex Spacecraft Illustration.

The velocity of the spacecraft and particle can be written using quasi-velocities in the following manner.

$$\boldsymbol{v}_B = v_1\hat{\boldsymbol{b}}_1 + v_2\hat{\boldsymbol{b}}_2 + v_3\hat{\boldsymbol{b}}_3 = u_4\hat{\boldsymbol{b}}_1 + u_5\hat{\boldsymbol{b}}_2 + u_6\hat{\boldsymbol{b}}_3 \tag{3.29}$$

$$\begin{aligned}\boldsymbol{v}_P &= [v_1 + b\dot{\theta}\cos\theta - \omega_3(c - r - b\cos\theta)]\hat{\boldsymbol{b}}_1 \\ &\quad + [v_2 + b\dot{\theta}\sin\theta - \dot{r} + \omega_3 b\sin\theta]\hat{\boldsymbol{b}}_2 \\ &\quad + [v_3 + \omega_1\,(c - r - b\cos\theta) - \omega_2 b\sin\theta]\,\hat{\boldsymbol{b}}_3 \\ &= [u_4 + u_7\cos\theta - u_3\,(c - r - b\cos\theta)]\,\hat{\boldsymbol{b}}_1 \\ &\quad + [u_5 + u_8 + u_3 b\sin\theta]\,\hat{\boldsymbol{b}}_2 \\ &\quad + [u_6 + u_1\,(c - r - b\cos\theta) - u_2 b\sin\theta]\,\hat{\boldsymbol{b}}_3\end{aligned} \tag{3.30}$$

This choice of quasi-velocities, u_i, results in the following matrix describing their

relationship to the generalized velocities, $\dot{q}_i$.

$$A = \begin{bmatrix} c_3/c_2 & -s_3/c_2 & 0 & 0 & 0 & 0 & 0 & 0 \\ s_3 & c_3 & 0 & 0 & 0 & 0 & 0 & 0 \\ -c_3 s_2/c_2 & s_3 s_2/c_2 & 1 & 0 & 0 & 0 & 0 & 0 \\ 0 & 0 & 0 & c_2 c_3 & -c_2 s_3 & s_2 & 0 & 0 \\ 0 & 0 & 0 & s_1 s_2 c_3 + s_3 c_1 & -s_1 s_2 s_3 + c_3 c_1 & -s_1 c_2 & 0 & 0 \\ 0 & 0 & 0 & -c_1 s_2 c_3 + s_1 s_3 & c_1 s_2 s_3 + s_1 c_3 & c_1 c_2 & 0 & 0 \\ 0 & 0 & 0 & 0 & 0 & 0 & s_8 & -1 \\ 0 & 0 & 0 & 0 & 0 & 0 & 1/b & 0 \end{bmatrix} \tag{3.31}$$

Here, $c_i = \cos q_i$ and $s_i = \sin q_i$, $\{q_1, q_2, q_3\}$ describe the spacecraft attitude, $\{q_4, q_5, q_6\}$ describe the spacecraft position, and $\{q_7, q_8\}$ describe the relative position of point P with $\{r, \theta\}$. The coordinate choices are described in more detail in Ref. [26].

Using $\boldsymbol{v}_B$, $\boldsymbol{v}_P$, and $\boldsymbol{\omega}_{B/N}$, the acceleration of the spacecraft and particle can be constructed.

$$\boldsymbol{a}_B = [\dot{u}_4 + u_2 u_6 - u_3 u_5]\hat{\boldsymbol{b}}_1 + [\dot{u}_5 + u_3 u_4 - u_1 u_6]\hat{\boldsymbol{b}}_2 + [\dot{u}_6 + u_1 u_5 - u_2 u_4]\hat{\boldsymbol{b}}_3 \tag{3.32}$$

$$\begin{aligned} \boldsymbol{a}_P = & \left[\dot{u}_4 + \dot{u}_7 \cos\theta - \dot{u}_3 (c - r - b\cos\theta) - u_7^2 \sin\theta/b - u_3 u_8\right] \hat{\boldsymbol{b}}_1 \\ & + \left[\dot{u}_5 + \dot{u}_8 + \dot{u}_3 b \sin\theta + u_3 u_7 \cos\theta\right] \hat{\boldsymbol{b}}_2 \\ & + \left[\dot{u}_6 + \dot{u}_1 (c - r - b\cos\theta) - \dot{u}_2 b \sin\theta + u_1 u_8 - u_2 u_7 \cos\theta\right] \hat{\boldsymbol{b}}_3 \\ & + \boldsymbol{\omega}_{B/N} \times \boldsymbol{v}_p \end{aligned} \tag{3.33}$$

For this problem, $\boldsymbol{\alpha} = \dot{u}_1 \hat{\boldsymbol{b}}_1 + \dot{u}_2 \hat{\boldsymbol{b}}_2 + \dot{u}_3 \hat{\boldsymbol{b}}_3$ and the (diagonal) elements of the spacecraft moment of inertia about its center, $\boldsymbol{I}_c$, coordinatized in the $\boldsymbol{b}$ frame are I_1, I_2, I_3.

The Gibbs function can now be formed using Eq. 3.5.

$$\begin{aligned}
\tilde{S} = {} & 1/2M\left[(\dot{u}_4 + u_2u_6 - u_3u_5)^2 + (\dot{u}_5 + u_3u_4 - u_1u_6)^2 + (\dot{u}_6 + u_1u_5 - u_2u_4)\right] \\
& + 1/2m\big[\{\dot{u}_4 + \dot{u}_7\cos\theta - \dot{u}_3\left(c - r - b\cos\theta\right) - u_7^2\sin\theta/b - u_3u_8 \\
& + u_2(u_6 + u_1\left(c - r - b\cos\theta\right) - u_2b\sin\theta) - u_3(u_5 + u_8 + u_3b\sin\theta)\}^2 \\
& + \{\dot{u}_5 + \dot{u}_8 + \dot{u}_3b\sin\theta + u_3u_7\cos\theta + u_3(u_4 + u_7\cos\theta - u_3\left(c - r - b\cos\theta\right)) \\
& - u_1(u_6 + u_1\left(c - r - b\cos\theta\right) - u_2b\sin\theta)\}^2 \\
& + \{\dot{u}_6 + \dot{u}_1\left(c - r - b\cos\theta\right) - \dot{u}_2b\sin\theta + u_1u_8 - u_2u_7\cos\theta \\
& + u_1(u_5 + u_8 + u_3b\sin\theta) - u_2(u_4 + u_7\cos\theta - u_3\left(c - r - b\cos\theta\right))\}^2\big] \\
& + 1/2(I_1\dot{u}_1^2 + I_2\dot{u}_2^2 + I_3\dot{u}_3^2) \\
& + \dot{u}_1u_2u_3(I_3 - I_2) + \dot{u}_2u_1u_3(I_1 - I_3) + \dot{u}_3u_1u_2(I_2 - I_1)
\end{aligned} \tag{3.34}$$

As the problem is presented in Ref. [26], there are no potential forces (i.e., no forces are explicitly given as a function of the coordinates). Here an equilibrium configuration is assumed to exist: $q_i = q_i^*$. Applying direct linearization, $z_{ij} = 0$, $k_{ij} = 0$, and the following nonzero m_{ij} components are found.

$$\begin{gathered}
m_{11} = I_1 + m(c - q_7^* - b\cos(q_8^*))^2 \quad ; \quad m_{22} = I_2 + m(b\sin(q_8^*))^2 \\
m_{33} = I_3 + m(b\sin(q_8^*))^2 + m(c - q_7^* - b\cos(q_8^*))^2 \\
m_{44} = m_{55} = m_{66} = M + m \quad ; \quad m_{88} = m_{58} = m \\
m_{77} = m(\cos(q_8^*))^2 \quad ; \quad m_{35} = m_{38} = mb\sin(q_8^*) \\
m_{26} = -mb\sin(q_8^*) \quad ; \quad m_{47} = m\cos(q_8^*) \\
m_{12} = -mb\sin(q_8^*)(c - q_7^* - b\cos(q_8^*)) \\
m_{16} = -m_{34} = m(c - q_7^* - b\cos(q_8^*)) \\
m_{37} = -m\cos(q_8^*)(c - q_7^* - b\cos(q_8^*))
\end{gathered} \tag{3.35}$$

Furthermore, the coefficients a_{ij} are simply A evaluated at the equilibrium configuration. Substituting the coefficients into Eq. 3.22, the linearized equations of motion are directly formed. For example, the first of the eight kinetic equations is as follows.

$$\begin{aligned}\big[I_1 + m(c - q_7^* - b\cos(q_8^*))^2\big]\dot{u}_1 + \big[- mb\sin(q_8^*)(c - q_7^* - b\cos(q_8^*))\big]\dot{u}_2 \\ + \big[m(c - q_7^* - b\cos(q_8^*))\big]\dot{u}_6 = U_1 \end{aligned} \tag{3.36}$$

Comparing each of the linearized equations to the full, nonlinear equations provided in Eqs. 63-70 of Ref. [26] shows them to be the correctly linearized equations of motion.

D. Summary

Direct linearization via the Gibbs function allows one to construct the first order linearized equations of motion about equilibrium for a system directly from a scalar augmented Gibbs function. This augmented function is akin to the Lagrangian in that it accounts for the contributions to the governing equations of potential forces in addition to the kinematics. If the full Gibbs equations, Eq. 3.4, are employed with $S = \tilde{S}$ and $U = U^P$, the same full nonlinear equations result as would have with the traditional Gibbs function and forces. This result is similar to the use of the Lagrangian versus the kinetic energy alone in Lagrange's equations. Note that the direct linearization methods of Refs. [9, 12, 19] use the Lagrangian, L, in the direct linearization formulation, rather than the kinetic energy alone. In a similar manner, the augmented Gibbs function accounts for nonlinearity of the generalized coordinates in potential forces during the direct linearization process. It is also of interest to note that the term appended to the Gibbs function is similar to the power rate of the potential forces, $\dot{\mathcal{P}} = \ddot{\mathcal{W}} = \mathrm{d}/\mathrm{d}t(P_i A_{ij}\eta_j)$. Two terms result from the time derivative, yet only one term contains $\dot{\eta}_i$ and subsequently can contribute to the equations of motion.

The power of direct linearization is that it forgoes computing the full nonlinear equations of motion prior to linearization and, as a result, is efficient and can be easily implemented in software. This work extends these features of direct linearization methods to the Gibbs/Appell dynamic modeling approach, the additional advantages of which are well-known. Particularly, these methods handle both holonomic and nonholonomic constraints directly and employ quasi-velocities, which often have important physical meanings themselves. Furthermore, the method can be implemented in systems with infinite-dimensional coordinates by first discretizing the domain. Thus, direct linearization can also be extended to continuous and hybrid dynamic systems.

Recall the relation between the Gibbs and Appell equations and Kane's equations. The existing Kanian direct linearization method is one particularly useful aspect of Kane's equations [27, 28]. Kane's linearization method can be broken down into the following steps [20, 21, 28].

1. Form nonlinear velocity vector.
2. Form partial velocities.
3. Linearize partial velocities.
4. Linearize velocity vector.
5. Form acceleration vector using linearized velocity vector.
6. Linearize acceleration vector.
7. Apply Kane's equations.
8. Linearize resulting equations of motion.

Here, note that steps 6 and 8 may or may not be necessary, depending on the preceding steps. That is, nonlinear terms may arise, perhaps due to accounting for rotating reference frames in step 5 or employing the dot product in step 7, that require additional work in order to form the final linearized equations. For example, for the complex spacecraft problem, the velocity of the point mass, $\boldsymbol{v}_P$, is written in a rotating frame. Even if this velocity is linearized in step 4, nonlinear terms arise through the kinematic transport theorem and must be ignored (in step 6), or, alternatively, their effect can be discarded after applying Kane's equations (in step 8). Furthermore, forming the generalized inertia torque for step 6 begets nonlinear terms that must be discarded (in step 8). (Note that these steps are not explicitly stated in the linearization description given by Kane, et al. in Ref. [21], but are included as a single, additional step by Kane, et al. in Ref. [20].)

The direct linearization method presented in this chapter provides an alternative to Kane's method. The steps can be enumerated as follows.

1. Form nonlinear velocity vector.
2. Form partial velocities.
3. Form nonlinear acceleration vector.
4. Form Gibbs function.
5. Form partial derivatives (m_{ij}, z_{ij}, k_{ij}, a_{ij}).
6. Form linearized equations of motion (Eqs. 3.22 and 3.23).

Although there may be fewer "steps" to this method, steps 4 and 5 may be cumbersome for large, multi-body systems. However, implicitly differentiating S (rather than completing the square and then explicitly differentiating) is recommended to ease

this burden. The advantage of this direct linearization method is that the linearization effort occurs in a single step in a simple "turn the crank" fashion, albeit using a more complex function beforehand. This method also provides a natural analogy to those available from a Lagrangian perspective without the explicit understanding of projection methods (yet arriving at the same result). Overall, both methods provide the advantages of using quasi-velocities, handling nonholonomic constraints, and forming the linearized equations of motion without requiring the construction of the full nonlinear equations.

CHAPTER IV

REDUNDANT COORDINATE ESTIMATION STRATEGY

The increased utilization of multi-body systems in space and robotic applications has brought significant attention to the use of redundant coordinate representations. Redundant coordinates lend themselves to multi-body system applications because they ease the derivation of the governing differential equations and usually better reflect the physical system, including system geometry, control effectors, and sensor locations, than a minimal coordinate description. However, the introduction of excess coordinates also necessitates subjecting the governing equations to holonomic constraints in order to reflect the actual system dynamics.

Employing the resulting system of differential algebraic equations (DAEs) in an estimation algorithm is less straightforward. Existing methods have been proposed to capture system constraints in the structure of the Kalman filter [29]. For this research, retaining the original structure of the CDEKF is desired, so the system model must be transformed to accommodate this framework. Constrained system DAEs can be transformed into ordinary differential equations (ODEs) via several methods. A nonlinear coordinate transformation or quasi-velocity approach is effective, but these approaches move away from coordinates and velocities that intuitively correlate with the physical geometry and motion of the system. As described in Ch. II, introduction and computation of Lagrange multipliers is another path with which many analytical and numerical methods are available.

For this estimation strategy, the process of developing the estimator is simplified by treating the forces arising from constraints (those terms associated with the Lagrange multipliers) as just that—constraint forces—rather than as part of the system

kinematic description.

A. Methodology

Here, the structure of the state matrix F for a dynamical system utilizing redundant coordinates (and consequently subject to holonomic constraints) is developed. Recall the definition of F and H from Ch. II, reprinted below.

$$\dot{\hat{\boldsymbol{x}}} = \boldsymbol{f}(\hat{\boldsymbol{x}}(t), \boldsymbol{u}(t), t) \quad ; \quad F(\hat{\boldsymbol{x}}(t), t) = \left.\frac{\partial \boldsymbol{f}}{\partial \boldsymbol{x}}\right|_{\hat{\boldsymbol{x}}(t)} \tag{4.1}$$

$$\tilde{\boldsymbol{y}}_k = \boldsymbol{h}_k(\boldsymbol{x}_k) + \boldsymbol{v}_k \quad ; \quad H_k(\hat{\boldsymbol{x}}_k^-) = \left.\frac{\partial \boldsymbol{h}}{\partial \boldsymbol{x}}\right|_{\hat{\boldsymbol{x}}_k^-} \tag{4.2}$$

In this chapter, the index associated with the discrete time step, k, is dropped for readability. Also recall consider the form of the equations of motion derived from a Lagrangian approach as also introduced in Ch. II.

$$[\dot{\boldsymbol{x}}] = \begin{bmatrix} \dot{\boldsymbol{q}} \\ \ddot{\boldsymbol{q}} \end{bmatrix} = \begin{bmatrix} \dot{\boldsymbol{q}} \\ M^{-1}\left[-\boldsymbol{g} + C^T\boldsymbol{\lambda} + \boldsymbol{Q}\right] \end{bmatrix} \tag{4.3}$$

Here the motion is described with $j = 1 \ldots n$ generalized coordinates q_j and velocities $\dot{q}_j$, subjected to $k = 1 \ldots m$ constraints ϕ_k, and influenced by nonpotential forces Q_j acting on the system (including control inputs). Together, $\boldsymbol{q}$ and $\dot{\boldsymbol{q}}$ are the states to be estimated, $\boldsymbol{x}$. By partitioning the strictly kinematics-based terms from the forces (constraint, potential, nonpotential, control, etc.), one can then make the assumption that either (1) $M^{-1}C^T\boldsymbol{\lambda}$ and $M^{-1}\boldsymbol{Q}$ or (2) $C^T\boldsymbol{\lambda}$ and $\boldsymbol{Q}$ are not functions of the states to simplify the process further.

In this work, assumption (1) is utilized, and the dynamic contribution of M is also neglected elsewhere in the governing equations. The resulting form for the

$2n \times 2n$ state matrix F then has a simple form.

$$F(\hat{\boldsymbol{x}}(t), t) = \begin{bmatrix} 0 & I \\ -M^{-1}\frac{\partial(\boldsymbol{g})}{\partial \boldsymbol{x}}\Big|_{\hat{\boldsymbol{x}}(t)} & \end{bmatrix} \tag{4.4}$$

Note that I is a identity matrix of dimension n. This perspective provides a straightforward approximation for a matrix that can be cumbersome to compute for constrained systems. The following examples show that the CDEKF can work well even with these simplifications.

B. Example 1: Classic Pendulum

First, a simple system is used to verify the methodology. The classic pendulum problem can be represented with a minimal coordinate (angle θ) or redundant rectilinear coordinates (x and y). The coordinate systems are shown in Fig. 3.

For this simulation, the length, L, of the massless rod is 1, the mass of the bob is 1, the initial velocity is $\sqrt{2}/10$, and the initial angle is 45 deg for the simulations. Gravity, $g = 10$, acts on the system. Also, it is assumed that the sensors available measure position and velocity in the rectilinear coordinates, the measurements have noise with $\sigma = .1$, and the initial guess error is 10%. Three cases are then considered.

First, the traditional approach of using a minimal coordinate description to develop the filter is applied. This system representation is governed by a single equation of motion.

$$\ddot{\theta} + \frac{g}{L}\sin\theta = 0 \tag{4.5}$$

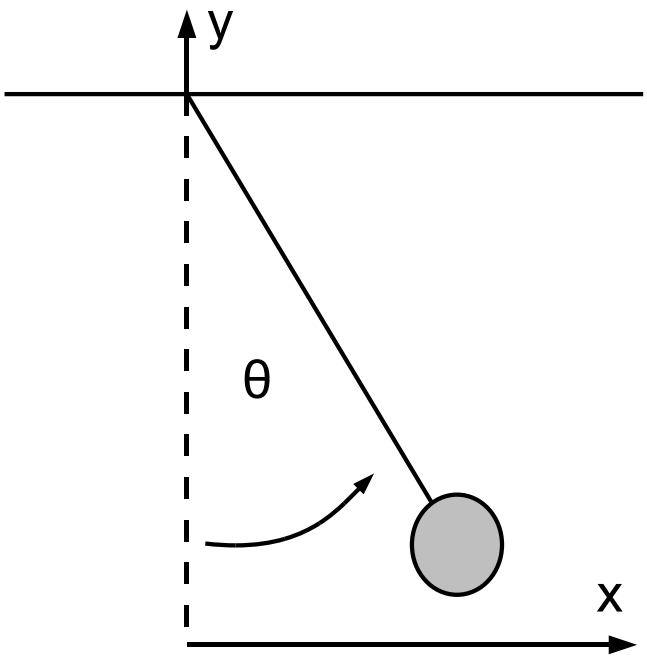

Fig. 3. Classic Pendulum Illustration.

Equations 4.1 and 4.2 yield the F and H matrices for this system.

$$F = \begin{bmatrix} 0 & 1 \\ -\frac{g}{L}\cos\theta & 0 \end{bmatrix} \qquad H = \begin{bmatrix} L\cos\theta & 0 \\ L\sin\theta & 0 \\ -L\dot{\theta}\sin\theta & L\cos\theta \\ L\dot{\theta}\cos\theta & L\sin\theta \end{bmatrix} \tag{4.6}$$

Note that this approach results in confidence intervals for the minimal coordinates and a nonlinear transformation must be derived to develop confidence intervals for the rectilinear states. The minimal description state estimate errors and confidence bounds constructed from the state covariance matrix are shown in Fig. 4.

Second, a conventional approach of using rectilinear coordinates and eliminating the Lagrange multipliers is considered. Recall that the set of governing differential

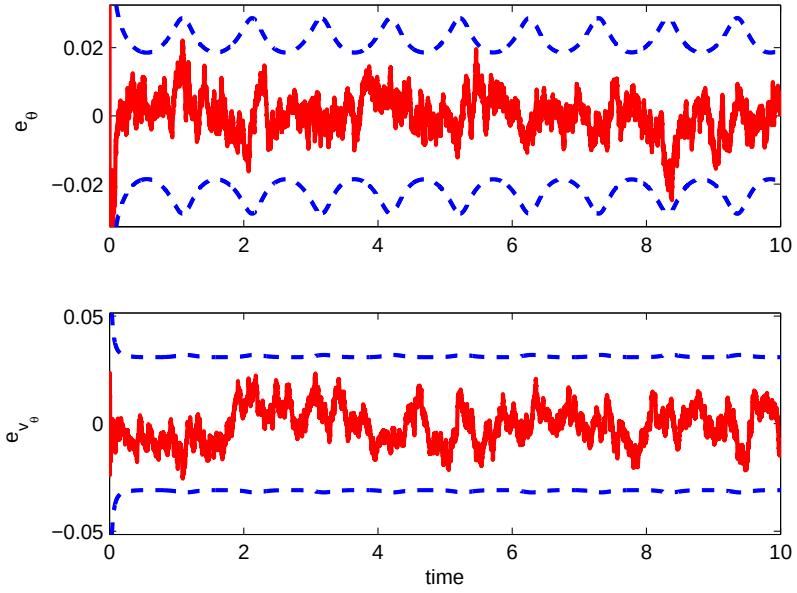

Fig. 4. Example 1: Minimal Coordinate State Estimate Error.

equations are subject to an algebraic constraint.

$$m\ddot{x} = \frac{\partial \phi}{\partial x}\lambda \tag{4.7}$$

$$m\ddot{y} = \frac{\partial \phi}{\partial y}\lambda - mg \tag{4.8}$$

$$\phi = x^2 + (L-y)^2 - L^2 = 0 \tag{4.9}$$

Using the range space method, a solution for λ can be obtained.

$$\lambda = \frac{m}{L^2}\left(g(y-L) - (\dot{x}^2 + \dot{y}^2)\right) \tag{4.10}$$

Substituting this solution into Eqs. 4.7 and 4.8, one can construct the F and H

matrices.

$$F = \begin{bmatrix} 0 & 0 & 1 & 0 \\ 0 & 0 & 0 & 1 \\ \frac{g(y-L)}{L^2} & \frac{gx}{L^2} & -\frac{2x\dot{x}}{L^2} & -\frac{2x\dot{y}}{L^2} \\ 0 & \frac{2g(y-L)}{L^2} & \frac{-2\dot{x}(y-L)}{L^2} & -\frac{2\dot{y}(y-L)}{L^2} \end{bmatrix} \qquad H = \begin{bmatrix} 1 & 0 & 0 & 0 \\ 0 & 1 & 0 & 0 \\ 0 & 0 & 1 & 0 \\ 0 & 0 & 0 & 1 \end{bmatrix} \tag{4.11}$$

The results from using this coordinate description with Lagrange multiplier elimination are presented in Figs. 5 and 6.

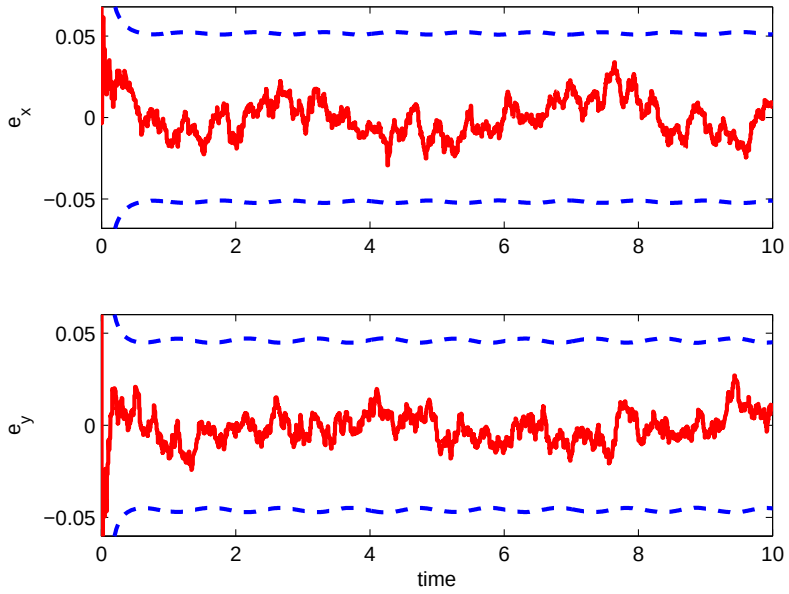

Fig. 5. Example 1: Redundant Coordinate Position State Estimate Error with Lagrange Multiplier Elimination.

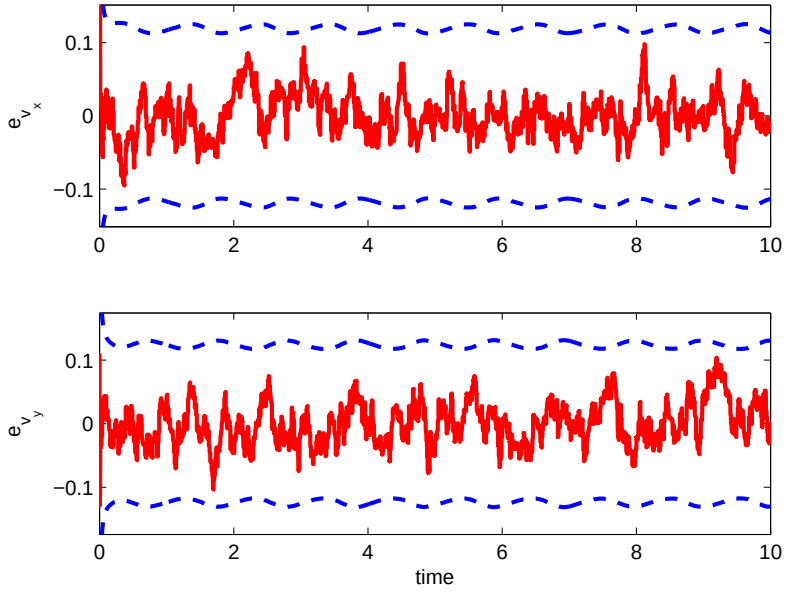

Fig. 6. Example 1: Redundant Coordinate Velocity State Estimate Error with Lagrange Multiplier Elimination.

Finally, consider the proposed approach of treating the Lagrange multiplier as independent from the coordinates. Simple forms of the F and H matrices result.

$$F = \begin{bmatrix} 0 & 0 & 1 & 0 \\ 0 & 0 & 0 & 1 \\ 0 & 0 & 0 & 0 \\ 0 & 0 & 0 & 0 \end{bmatrix} \qquad H = \begin{bmatrix} 1 & 0 & 0 & 0 \\ 0 & 1 & 0 & 0 \\ 0 & 0 & 1 & 0 \\ 0 & 0 & 0 & 1 \end{bmatrix} \tag{4.12}$$

Note that the state matrix F does not directly account for the effect of the constraints, though the state estimate propagation equation (Eq. 2.29) does. Figures 7 and 8 show that the state covariance error bounds are similar to those for the constraint elimination case.

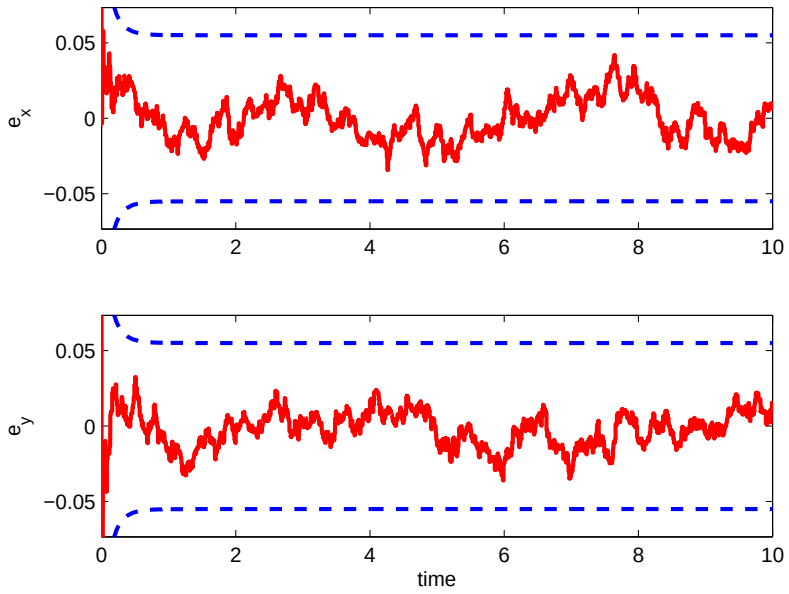

Fig. 7. Example 1: Redundant Coordinate Position State Estimate Error with Constraint Force Perspective.

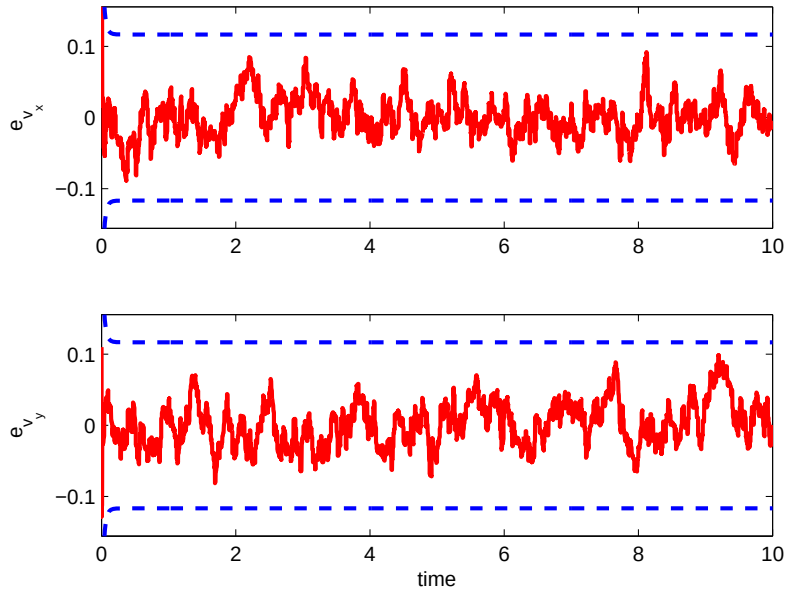

Fig. 8. Example 1: Redundant Coordinate Velocity State Estimate Error with Constraint Force Perspective.

C. Example 2: Two-Arm Robot

Now consider the more complex example of the two-arm manipulator robot with rigid payload in a gravity-free environment, as shown in Fig. 9. The position and attitude of the payload can be described by the coordinates (x, y, α). Since the system has only three degrees of freedom, this minimal set of coordinates is sufficient to describe the motion of the system. However, the controls for the manipulator arms are located at the manipulator joints and use the angles θ_i, $i = 1 \ldots 4$, in the control laws, so it is desired to instead describe this system with a set of seven coordinates (θ_1, θ_2, θ_3, θ_4, α, x, y) subject to four constraints. This coordinate description results in a 14-element state vector.

$$\boldsymbol{x} = [\theta_1, \theta_2, \theta_3, \theta_4, \alpha, x, y, \dot{\theta}_1, \dot{\theta}_2, \dot{\theta}_3, \dot{\theta}_4, \dot{\alpha}, \dot{x}, \dot{y}]^T \tag{4.13}$$

Let the coordinate states be described with $\boldsymbol{q}$ and the velocity states with $\dot{\boldsymbol{q}}$.

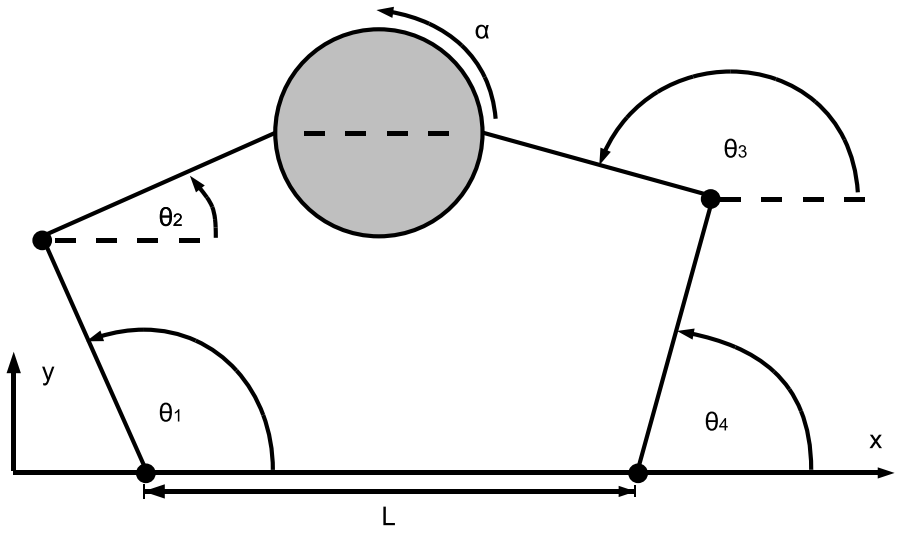

Fig. 9. Two-Arm Robot Illustration.

The 2nd-order differential equations of motion are now developed for this system. For the simulation results, the payload has mass $m_p = 6$, inertia $I_p = 1$, and diameter $L_p = 1$. The manipulator arms are numbered counterclockwise from the lower left hand side and have mass $m_i = 12$, inertia $I_i = 1$, and length $L_i = 1$ for $i = 1 \ldots 4$. The shoulders of the two arms are separated by a distance $L = 1 + 2\sqrt{2}$, and the arms are connected to the payload at fixed points, which constrains the motion of the system.

$$\begin{aligned}
\phi_1 = 0 &= L_1 \cos\theta_1 + L_2 \cos\theta_2 - x + \frac{L_p}{2}\cos\alpha \\
\phi_2 = 0 &= L_1 \sin\theta_1 + L_2 \sin\theta_2 - y + \frac{L_p}{2}\sin\alpha \\
\phi_3 = 0 &= L_3 \cos\theta_3 + L_4 \cos\theta_4 + L - x - \frac{L_p}{2}\cos\alpha \\
\phi_4 = 0 &= L_3 \sin\theta_3 + L + 4\sin\theta_4 - y + \frac{L_p}{2}\sin\alpha
\end{aligned} \tag{4.14}$$

The mass matrix, M, of Eq. 2.12 can be written as a block diagonal matrix.

$$M = \begin{bmatrix} M_L & 0 & 0 \\ 0 & M_R & 0 \\ 0 & 0 & M_P \end{bmatrix} \tag{4.15}$$

Here M_L denotes the sub-matrix of M associated with the left-hand arm, M_R with the right-hand arm, and M_P with the payload.

$$M_L = \begin{bmatrix} \frac{1}{4}m_1 L_1^2 + I_1 + m_2 L_1^2 & \frac{1}{2}m_2 L_1 L_2 \cos\theta_{21} \\ \frac{1}{2}m_2 L_1 L_2 \cos\theta_{21} & \frac{1}{4}m_2 L_2^2 + I_2 \end{bmatrix} \tag{4.16}$$

$$M_R = \begin{bmatrix} \frac{1}{4}m_3 L_3^2 + I_3 + m_4 L_3^2 & \frac{1}{2}m_4 L_3 L_4 \cos\theta_{43} \\ \frac{1}{2}m_4 L_3 L_4 \cos\theta_{43} & \frac{1}{4}m_4 L_4^2 + I_4 \end{bmatrix} \tag{4.17}$$

$$M_p = \begin{bmatrix} I_p & 0 & 0 \\ 0 & m_p & 0 \\ 0 & 0 & m_p \end{bmatrix} \tag{4.18}$$

Note that $\theta_{ij} = \theta_i - \theta_j$, and that the Lagrangian for this system, equal to the kinetic energy, is $L = 1/2\dot{\boldsymbol{q}}M\dot{\boldsymbol{q}}$. The control inputs form the nonpotential force vector.

$$\boldsymbol{Q} = \begin{bmatrix} u_1 - u_2 & u_2 & u_3 - u_4 & u_4 & 0 & 0 & 0 \end{bmatrix}^T \tag{4.19}$$

Next, applying Lagrange's equations to the system, the resulting governing equations presented in Eq. 4.3 are shown again here.

$$[\dot{\boldsymbol{x}}] = \begin{bmatrix} \dot{\boldsymbol{q}} \\ \ddot{\boldsymbol{q}} \end{bmatrix} = \begin{bmatrix} \dot{\boldsymbol{q}} \\ M^{-1}\left[-\boldsymbol{g} + C^T\boldsymbol{\lambda} + \boldsymbol{Q}\right] \end{bmatrix} \tag{4.20}$$

Velocity- and position-level terms unrelated to the generalized and constraint forces are captured in $\boldsymbol{g}$.

$$\boldsymbol{g} = \begin{bmatrix} -\frac{1}{2}m_2L_1L_2\dot{\theta}_2^2\sin\theta_{21} \\ \frac{1}{2}m_2L_1L_2\dot{\theta}_1^2\sin\theta_{21} \\ -\frac{1}{2}m_4L_3L_4\dot{\theta}_4^2\sin\theta_{43} \\ \frac{1}{2}m_4L_3L_4\dot{\theta}_3^2\sin\theta_{43} \\ [0]_{3\times1} \end{bmatrix} \tag{4.21}$$

The constraint influence matrix is constructed using the constraints of Eq. 4.14.

$$C = \begin{bmatrix} -L_1\sin\theta_1 & -L_2\sin\theta_2 & 0 & 0 & -\frac{1}{2}L_p\sin\alpha & -1 & 0 \\ L_1\cos\theta_1 & L_2\cos\theta_2 & 0 & 0 & \frac{1}{2}L_p\cos\alpha & 0 & -1 \\ 0 & 0 & -L_3\sin\theta_3 & -L_4\sin\theta_4 & \frac{1}{2}L_p\sin\alpha & -1 & 0 \\ 0 & 0 & L_3\cos\theta_3 & L_4\cos\theta_4 & \frac{1}{2}L_p\cos\alpha & 0 & -1 \end{bmatrix} \tag{4.22}$$

The state matrix is then given by Eq. 7.8, and the H matrix is I, since all states are

assumed to be measured.

With the estimation algorithm now constructed in this manner, the system motion can be simulated by choosing a method for eliminating the Lagrange multipliers in the state propagation equation. For the following results, the measurement error standard deviation is .1 and the initial guess error is 10%. The system, initially at rest, is driven by a prescribed control sequence and has the following initial constraint-compatible coordinates.

$$\boldsymbol{q}(t_0) = [\ 1/2 + \sqrt{2} \quad 0 \quad 0 \quad 45\,\text{deg} \quad -45\,\text{deg} \quad 135\,\text{deg} \quad 225\,\text{deg}\ ]^T \tag{4.23}$$

The simulation results for the proposed method show that the Kalman filter is able to successfully converge and bound the error residuals below the prescribed measurement error. Figures 10 and 11 show the residuals and error bounds for the coordinate states, whereas Figs. 12 and 13 show the errors associated with the velocity states.

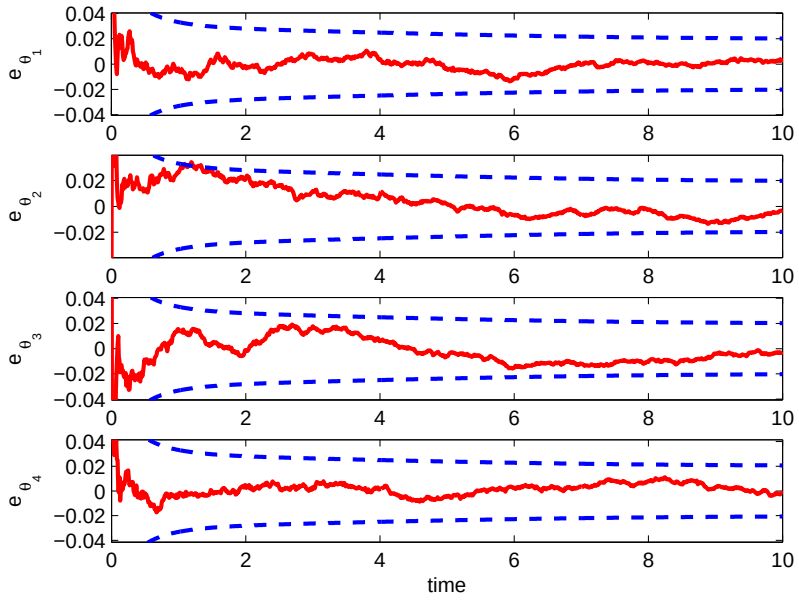

Fig. 10. Example 2: Arm Configuration State Estimate Error.

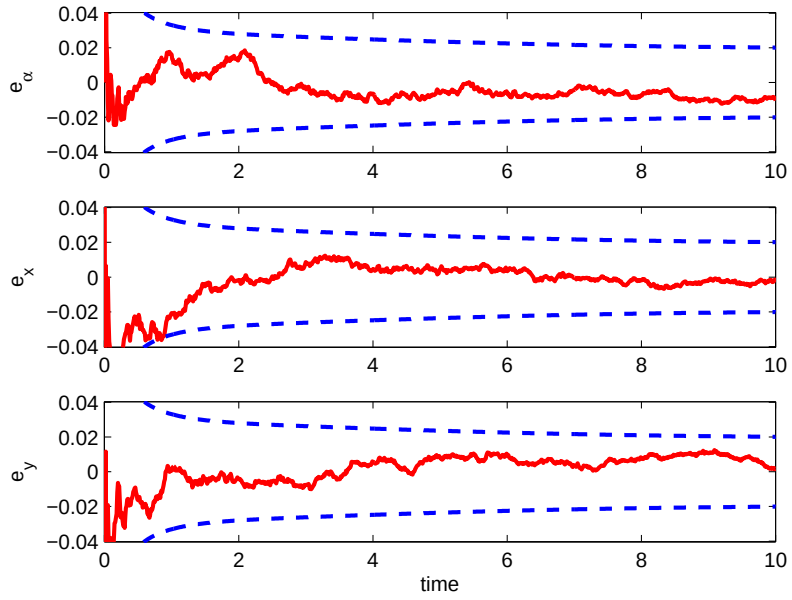

Fig. 11. Example 2: Payload Configuration State Estimate Error.

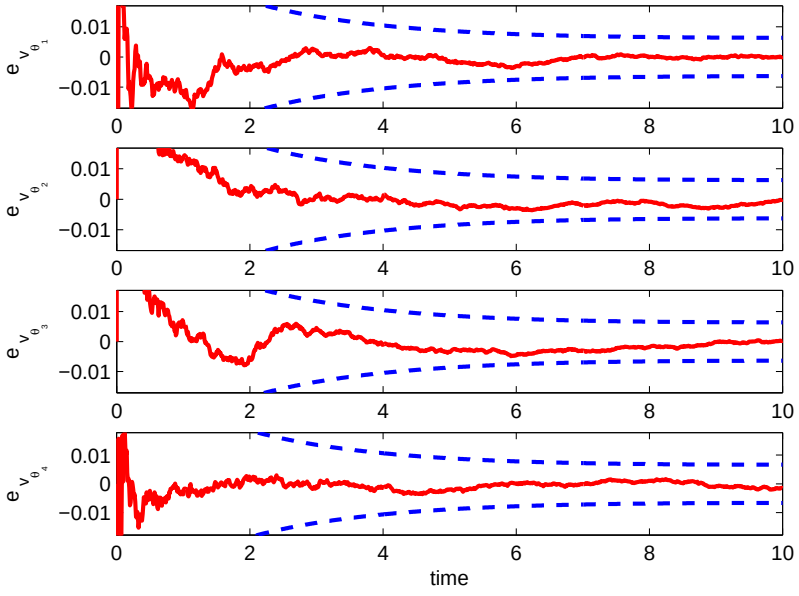

Fig. 12. Example 2: Arm Velocity State Estimate Error.

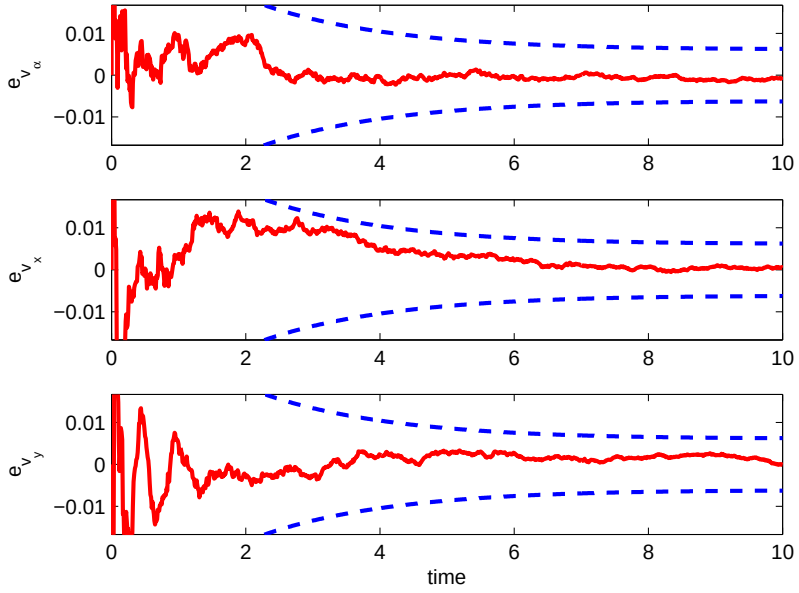

Fig. 13. Example 2: Payload Velocity State Estimate Error.

D. Approximation Error

For the two examples presented, the system states are fully observable ($H_k = H = I$) and the measurement sampling frequencies are much higher than those of the system dynamics. Of interest, though, is how the "constraint force" perspective fares when this is not the case. Here, two redundant coordinate estimation strategies are compared for the pendulum of Example 1 over a range of measurement sampling frequencies for three cases.

- Measure all states (fully observable).
- Measure position only ($\boldsymbol{y}_m = [x, y]$).
- Measure x-position and y-velocity ($\boldsymbol{y}_m = [x, \dot{y}]$).

The first strategy considered is that in which the constraint force is written as an explicit function of the system states, $f_c = f_c(\boldsymbol{x}, t)$, and the second strategy is that

proposed in this chapter (the approximation in which it is not, $f_c = f_c(t)$). Using the same source of measurements with error $\sigma_{\boldsymbol{y}_m} = .1$, the state estimate error at each time step, $\boldsymbol{e}_k$, is calculated as the difference between the true states and the state estimates. The measure selected to evaluate the total error is the sum square of the errors.

$$J = \boldsymbol{e}_k^T \boldsymbol{e}_k \tag{4.24}$$

The simulation results for this exercise are shown in Fig. 14. For the two cases in which a subset of states are measured, the approximation admits a greater steady-state error. For this specific example, the governing equations are linear in the states from the $f_c(t)$ perspective. Investigation of the observability matrix, $\mathcal{O} = [H; HF]$, reveals that $\mathcal{O}$ is not full rank and the system subsequently has unobservable states, which supports the simulation results [1].

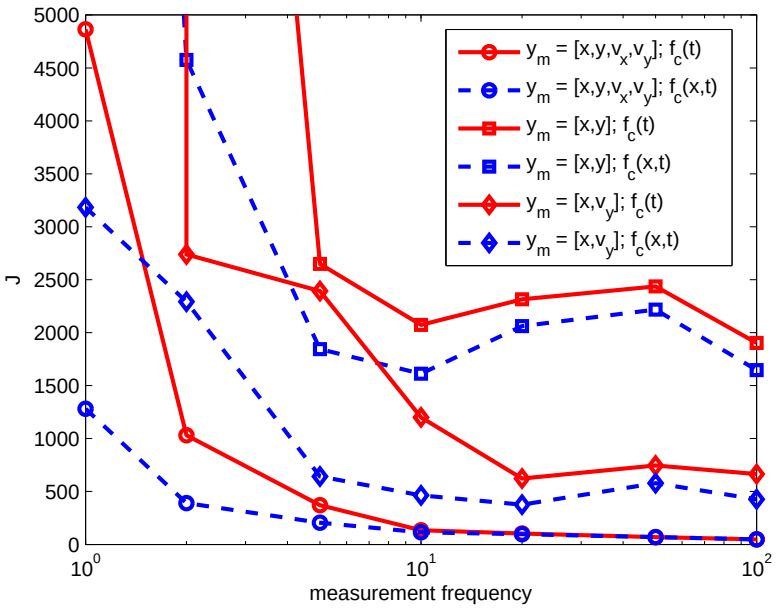

Fig. 14. Observability and Measurement Frequency Error.

With respect to measurement frequency alone, the approximation strategy performs similarly to the full redundant coordinate model. As shown in Fig. 14, the methods exhibit comparable error at higher frequencies and both significantly increase in error at smaller measurement sampling intervals. For this system, the approximate natural frequency (i.e. small angle θ) is $\omega_n \approx \sqrt{g/L} = \sqrt{10}$. As both strategies approach this value in measurement frequency, the CDEKF accuracy decreases. However, the error does increase more rapidly for the approximation in this lower-frequency range. This greater sensitivity to measurement sampling frequency is important, but is not so much greater that than for the full model as to overcome other advantages of neglecting the state-dependence of the constraint force.

Note that, for this example, of interest may be a measurement frequency sensitivity comparison between each redundant coordinate strategy and the minimal coordinate representation (which implicity accounts for the constraint). In this chapter, however, the goal is to more easily admit the use of redundant coordinates. Even if the minimal coordinate representation can be shown less sensitive to measurement frequency, this advantage alone may not be sufficient to overcome the advantages of the redundant coordinate representations outlined herein.

E. Summary

In this chapter, a straightforward approach for developing a Kalman filter for dynamic systems with redundant coordinates and, subsequently, holonomic constraints is presented. The proposed simplification facilitates the construction of an estimation algorithm by decreasing the amount of partial differentiation necessary to implement the continuous-discrete extended Kalman filter. Furthermore, this method does not require a specific solution method for calculating the Lagrange multipliers; this choice is left to the engineer. A simple classic pendulum example shows that the proposed

approach can result in error residuals comparable to those of the full version of the Kalman filter. The two arm robot manipulator example shows a more complex system for which the control effector locations make the use of redundant coordinates particularly desirable. These results show that, with the simplification presented here, the estimator converges and reduces the error residuals and confidence bounds below that of the measurement error. Simulation results also show that, for less ideal measurements, the approximation is more sensitive to reduced observability and sampling frequency. For many systems, however, this sensitivity may not be much greater than that of the full redundant coordinate formulation. Overall, the examples show how this approach can be effectively utilized to build a straightforward estimator for systems described with redundant coordinates.

CHAPTER V

CONSTRAINT MONITORING ESTIMATION STRATEGY

Sometimes a dynamical system subject to a constraint is configured or undergoes motion such that the constraint is not held for some period of time, often unintentionally. For example, a tether connecting two spacecraft may fail. For intervals where the constraint is not held, a different dynamical model of the system may be more appropriate. In order to determine whether a constraint is violated, a qualitative measure of the constraint and an associated confidence bound is needed. Furthermore, this measure must be updated frequently to monitor changes in the system associated with a constraint violation. Here, a sequential estimate of the constraint itself is the measure employed. Two methods for estimating the constraint are presented: first, construction of the constraint using state estimates and second, estimation of the constraint via the Kalman Filter framework.

A. Methodology

Two approaches for estimating the constraint and associated variance are investigated. Recall that ϕ represents either a holonomic or a nonholonomic (scleronomic) constraint and $\boldsymbol{x}$ represents the state vector of generalized coordinates and velocities. Each of the proposed approaches use the current estimates of the states to construct an "estimate" or a "measurement" for ϕ.

$$\hat{\phi} = \phi(\hat{\boldsymbol{x}}) \tag{5.1}$$

The two methods vary, however, in how this value is utilized and how the associated variance is constructed.

1. Method 1: Construct Constraint and Variance

The first estimation strategy utilizes the property that expectation, $E\{x\}$, is a linear operator [1].

$$E\{ax_1 + bx_2\} = aE\{x_1\} + bE\{x_2\} \tag{5.2}$$

Here, a and b are not functions of the states and are usually constant coefficients. The constraint error covariance is based on the constraint error, which is the difference between the true value of the constraint, ϕ_t, and the estimated value, $\hat{\phi}$.

$$\tilde{\phi} = \hat{\phi} - \phi_t \tag{5.3}$$

Note that if the constraint is held, the estimate for ϕ_t should equal zero (within some confidence bound associated with the constraint error covariance). For a constraint linear in the states, $\phi = a_i x_i$, the variance associated with this bound can be constructed in the following manner with $i \neq j$.

$$\begin{aligned} \sigma_\phi^2 = E\{\tilde{\phi}^2\} &= a_i^2 E\{\tilde{x}_i^2\} + 2a_i a_j E\{\tilde{x}_i \tilde{x}_j\} \\ &= a_i^2 \sigma_i^2 + 2a_i a_j \sigma_{ij} \end{aligned} \tag{5.4}$$

Here, a_i represents the coefficient of x_i, σ_i^2 is the variance associated with x_i, and σ_{ij} is the covariance associated with x_i and x_j. These values can be extracted from the state error covariance matrix. For a nonlinear constraint, this relationship can be approximated by first linearizing the constraint estimate about the true value of the constraint ($\phi_t = \phi(\boldsymbol{q}_t)$).

$$\begin{aligned} \bar{\hat{\phi}} &\approx \phi\Big|_{\boldsymbol{x}_t} + \frac{\partial \phi}{\partial x_i}\Big|_{\boldsymbol{x}_t} (\hat{x}_i - x_{i_t}) + \dots \\ &\approx \phi_t + \frac{\partial \phi}{\partial x_i}\Big|_{\hat{\boldsymbol{x}}} (\tilde{x}_i) + \dots \end{aligned} \tag{5.5}$$

The constraint error can then be approximated.

$$\tilde{\phi} \approx \bar{\tilde{\phi}} - \phi_t = \left.\frac{\partial \phi}{\partial x_i}\right|_{\hat{\boldsymbol{x}}} \tilde{x}_i \tag{5.6}$$

An approximation for the constraint error variance can then be constructed in a similar manner as for linear constraints.

$$\begin{aligned}
\sigma_\phi^2 = E\{\tilde{\phi}\} &\approx E\left\{ \left[\frac{\partial \phi}{\partial x_i}\right]_{\hat{\boldsymbol{x}}}^2 \tilde{x}_i^2 + 2\left[\frac{\partial \phi}{\partial x_i}\frac{\partial \phi}{\partial x_j}\right]_{\hat{\boldsymbol{x}}} \tilde{x}_i \tilde{x}_j \right\} \\
&\approx \left[\frac{\partial \phi}{\partial x_i}\right]_{\hat{\boldsymbol{x}}}^2 E\left\{\tilde{x}_i^2\right\} + 2\left[\frac{\partial \phi}{\partial x_i}\frac{\partial \phi}{\partial x_j}\right]_{\hat{\boldsymbol{x}}} E\left\{\tilde{x}_i \tilde{x}_j\right\} \\
&\approx \left[\frac{\partial \phi}{\partial x_i}\right]_{\hat{\boldsymbol{x}}}^2 \sigma_i^2 + 2\left[\frac{\partial \phi}{\partial x_i}\frac{\partial \phi}{\partial x_j}\right]_{\hat{\boldsymbol{x}}} \sigma_{ij}
\end{aligned} \tag{5.7}$$

In this approach, both $\hat{\phi}$ and σ_ϕ^2 are constructed in the propagation/prediction step of the CDEKF using the values $\hat{\boldsymbol{x}} = \hat{\boldsymbol{x}}_k^+$ from the most recent update step. The logic employed for both methods is later described. Note that the variance terms along the diagonal, σ_i^2, tend to dominate the state error covariance matrix.

2. Method 2: Estimate Constraint and Variance

A second approach for estimating both the constraint and variance is to append ϕ to the state vector within the Kalman Filter framework. The computational complexity of this approach can be reduced by building a secondary constraint filter that essentially runs parallel to the state filter and uses the state estimates to construct constraint "measurements," $y_{m_\phi}(t_k) = \hat{\phi}(\boldsymbol{x}_k^-)$. Within the CDEKF framework, the following matrices subsequently result.

$$H_{\phi_k} = 1 \quad ; \quad F_\phi = 0 \tag{5.8}$$

The constraint measurement covariance matrix, R_{k_ϕ}, is constructed using Eq. 5.7, and $Q_\phi(t) > 0$ is tuned to provide a small perturbation to the covariance matrix propaga-

tion via process noise. To propagate the constraint estimate itself in the "prediction" step of the Kalman Filter, the time derivative of the constraint is employed.

$$\dot{\phi} = \frac{\partial \phi}{\partial x_i} \dot{x}_i \tag{5.9}$$

The remaining equations of the CDEKF can be applied for the constraint as written in Ch. II. However, note that unlike in Method 1, the constraint "measurements" are constructed in the update/correction step of the CDEKF.

3. Employing the Constraint Variance

The constraint variance provides a measure of the uncertainty of the constraint estimate. Taking the square root of the variance provides the $1-\sigma$ bound for the constraint estimate. By assuming that the "truth" value for the constraint is equal to zero, constraint violation can be detected when the constraint estimate leaves the $1-\sigma$, $2-\sigma$, $3-\sigma$, etc. bound, as determined most appropriate by the user.

Given two potential system models, $\dot{\boldsymbol{q}}_c = \boldsymbol{f}_c(\boldsymbol{q}, t)$ and $\dot{\boldsymbol{q}}_u = \boldsymbol{f}_u(\boldsymbol{q}, t)$, where c and u indicate "constrained" or "unconstrained," the uncertainty bound can then be combined with conditional logic to allow the estimation algorithm to autonomously choose the more appropriate dynamic model for the system.

If $|\hat{\phi}_k| > \sigma_{\phi_k}$,

$\dot{\boldsymbol{q}}_u = \boldsymbol{f}_u(\boldsymbol{q}, t)$

Else

$\dot{\boldsymbol{q}}_c = \boldsymbol{f}_c(\boldsymbol{q}, t)$

End

Here the $1-\sigma$ bound is used. Note that, for systems subject to more than one constraint, both approaches can be modified to accommodate multiple constraints using vector notation. The most difficult accommodation is the logic employed to

switch between candidate system models.

B. Simulation Results

Two candidate systems are simulated using each of the two proposed methods. The first system is a two-dimensional disk rolling without slip along a straight, horizontal surface. The linear constraint associated with this system is violated when the wheel begins to slip for a specified time interval. Example 2 consists of a planar pendulum with an obstacle in the right-hand plane.

The simulation results from the first two examples indicate that Method 1 is both more effective and less computationally expensive. Two additional, more complex examples are simulated using only Method 1. The third example is a planar vehicle, such as a sled or ice skate, and the final example is a tethered satellite system orbiting the Earth.

1. Example 1: Rolling Disk

In this section, the simulation results for a disk of radius R and mass m rolling initially without slip, and for some time with slip, are presented. Figure 15 illustrates this system. The states for this system are the displacement, x, translational velocity, $\dot{x}$, disk angle, θ, and disk angular velocity, $\dot{\theta}$.

If the constraint $\phi = \dot{x} - R\dot{\theta}$ is held, the dynamics of this system can be described with Model 1.

$$\dot{\boldsymbol{q}} = \begin{bmatrix} \dot{\theta} \\ \ddot{\theta} \\ \dot{x} \\ \ddot{x} \end{bmatrix} = \begin{bmatrix} 0 & 1 & 0 & 0 \\ 0 & 0 & 0 & 0 \\ 0 & 0 & 0 & 1 \\ 0 & 0 & 0 & 0 \end{bmatrix} \begin{bmatrix} \theta \\ \dot{\theta} \\ x \\ \dot{x} \end{bmatrix} + \begin{bmatrix} 0 \\ 1/Rm \\ 0 \\ 1/m \end{bmatrix} [u] \tag{5.10}$$

However, if the constraint is violated and the disk begins to slide rather than roll

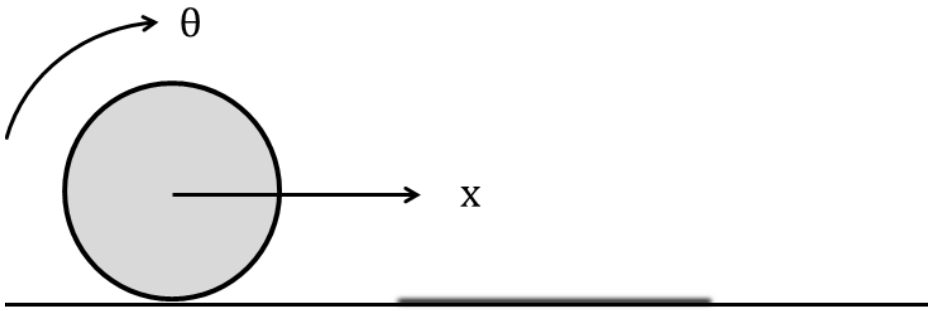

Fig. 15. Rolling Disk Illustration.

without slip, the more appropriate model is Model 2.

$$\dot{\boldsymbol{q}} = \begin{bmatrix} \dot{\theta} \\ \ddot{\theta} \\ \dot{x} \\ \ddot{x} \end{bmatrix} = \begin{bmatrix} 0 & 1 & 0 & 0 \\ 0 & 0 & 0 & 0 \\ 0 & 0 & 0 & 1 \\ 0 & 0 & 0 & 0 \end{bmatrix} \begin{bmatrix} \theta \\ \dot{\theta} \\ x \\ \dot{x} \end{bmatrix} + \begin{bmatrix} 0 \\ 0 \\ 0 \\ 1/m \end{bmatrix} [u] + \begin{bmatrix} 0 \\ 0 \\ 0 \\ 1/m \end{bmatrix} [-\mu m g] \qquad (5.11)$$

For the following simulations, $R = m = 1$, $g = 10$, $u = 2$ and $\mu = .1$ for the time interval $0 < t < 10$. The measurements are the configuration coordinates x and θ, and are constructed with measurement error $\sigma_{y_m} = 2$, which is not insignificant. The measurement covariance matrix is $R_k = \sigma_{y_m}^2 I$ where I is a 2×2 identity matrix. The process noise covariance matrix is a 4×4 diagonal matrix with entries [0.0025, 0.5, 0.0025, 0.5], and the states are initialized with 10% error.

The true system experiences slip between $t = 1$ and $t = 5$. At $t = 3$, $u = 0$ until the constraint is again held. Also note that, although this constraint is holonomic and can be integrated, the constraint is used "as-is" with velocity-level states that are estimated (i.e., not measured directly). Integration of this constraint with respect

to time requires initial conditions at time t_0.

$$\int_{t_0}^{t} (\dot{x}(\tau) - R\dot{\theta}(\tau))\mathrm{d}\tau = [x(t) - R\theta(t)] - [x(t_0) - R\theta(t_0)] \tag{5.12}$$

Here t_0 refers to the point where the constraint is initially engaged, which may occur at several points in the time interval. Thus, using the velocity-level constraint with instantaneous state estimates is more easily facilitated in the estimation framework.

The simulation results show that both methods are able to track the constraint violation, albeit with some delay, as shown in Figs. 16 and 17. The time delay is likely related to the uncertainty bound, as the non-zero constraint estimate must pass this bound for constraint violation to be detected with a set level of certainty. Note that, in order for the Method 2 CDEKF to perform comparably to the Method 1 CDEKF, a very large amount of process noise, i.e. $Q_\phi = 15$, must be applied to the constraint covariance propagation equation. Typically, the process noise is increased to accommodate modeling errors and to drive the CDEKF to more heavily weight the measurements. Here, the large amount of process noise indicates that driving Method 2 to behave "more like" Method 1 increases its effectiveness.

Figures 18-21 show that the constraint estimate leaves the $1 - \sigma$ error bound in the "slip" region and Model 2 is successfully implemented. With Method 2, however, the constraint estimate drifts and Model 2 is incorrectly applied when the constraint is not violated. Even though only position-level states are sensed, all four states are well-tracked with Method 1. Method 2 tracks effectively until Model 2 is incorrectly employed late in the time interval. The measurements and state estimates for both methods are shown in Figs. 22-27.

Note that the estimates and errors are shown in red, whereas the truth, measurements, and error bounds are shown in blue.

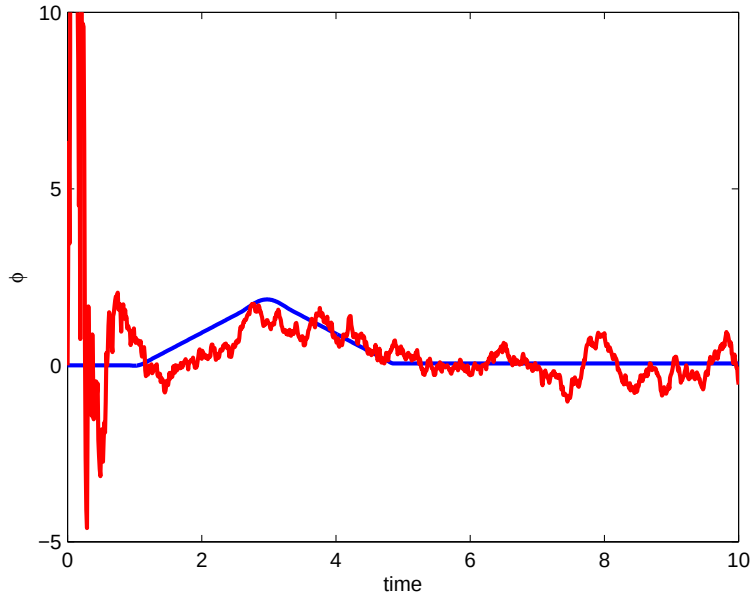

Fig. 16. Example 1: True and Estimated Constraint Value Using Method 1.

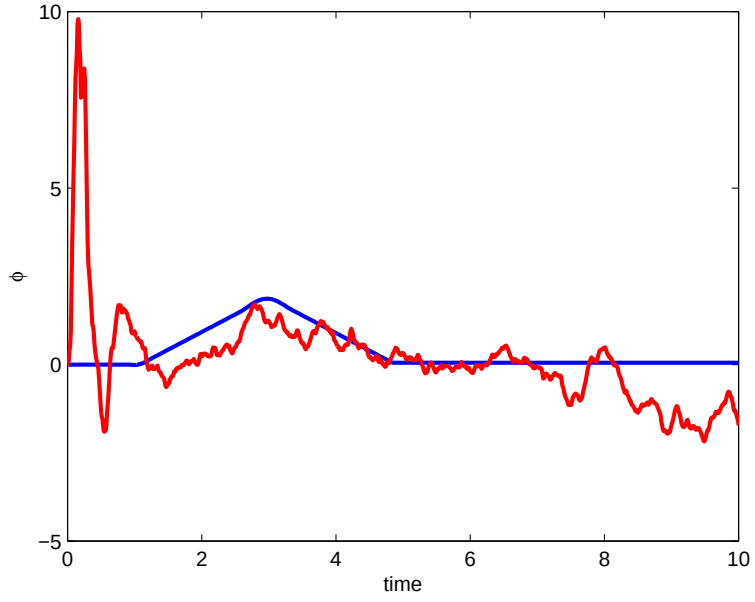

Fig. 17. Example 1: True and Estimated Constraint Value Using Method 2.

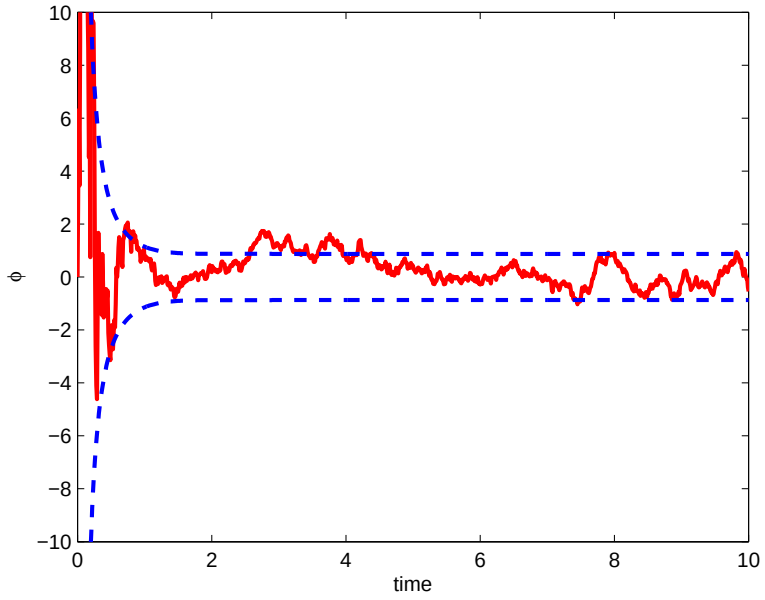

Fig. 18. Example 1: Constraint Estimate with $1-\sigma$ Error Bounds Using Method 1.

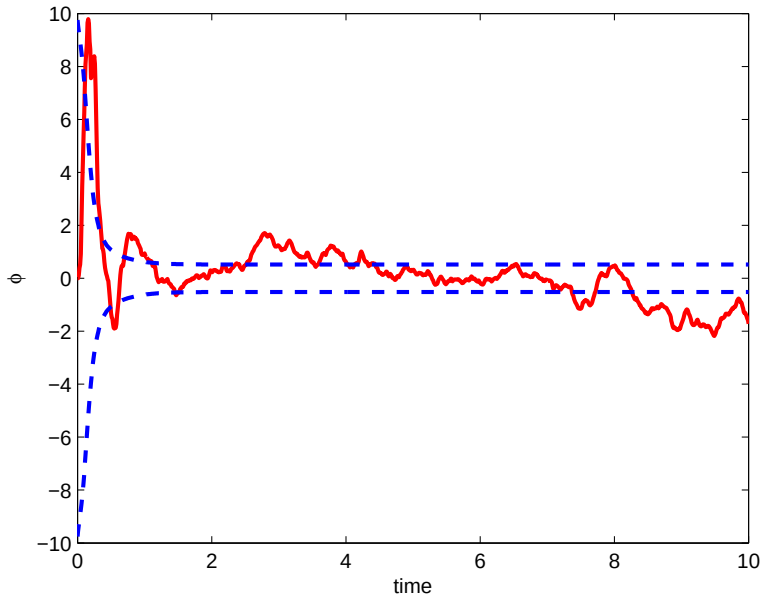

Fig. 19. Example 1: Constraint Estimate with $1-\sigma$ Error Bounds Using Method 2.

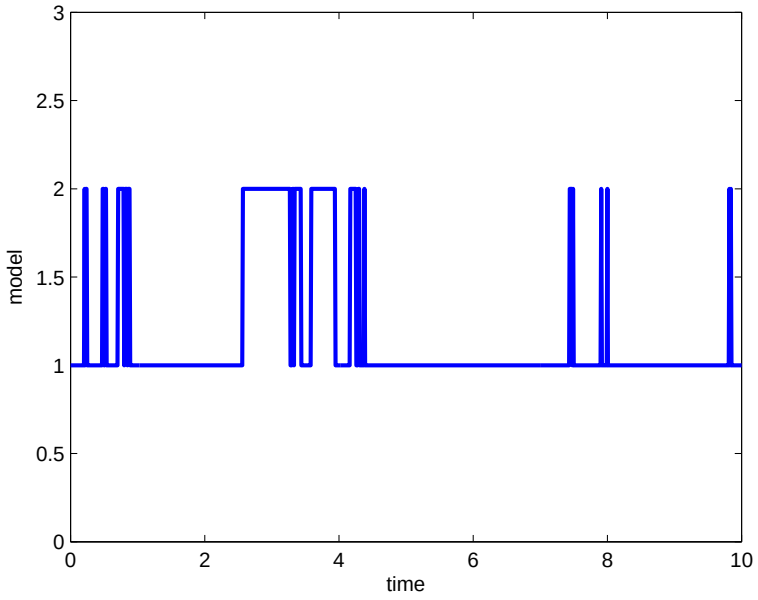

Fig. 20. Example 1: Model Time History Using Method 1.

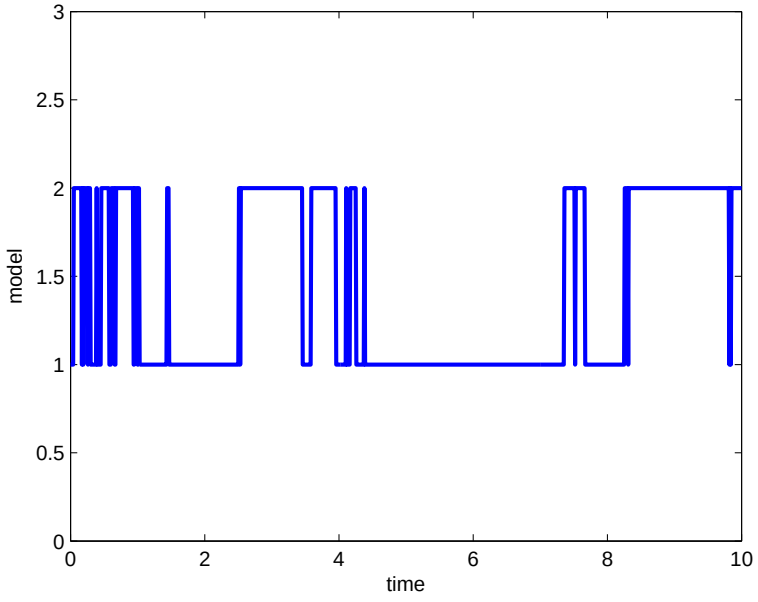

Fig. 21. Example 1: Model Time History Using Method 2.

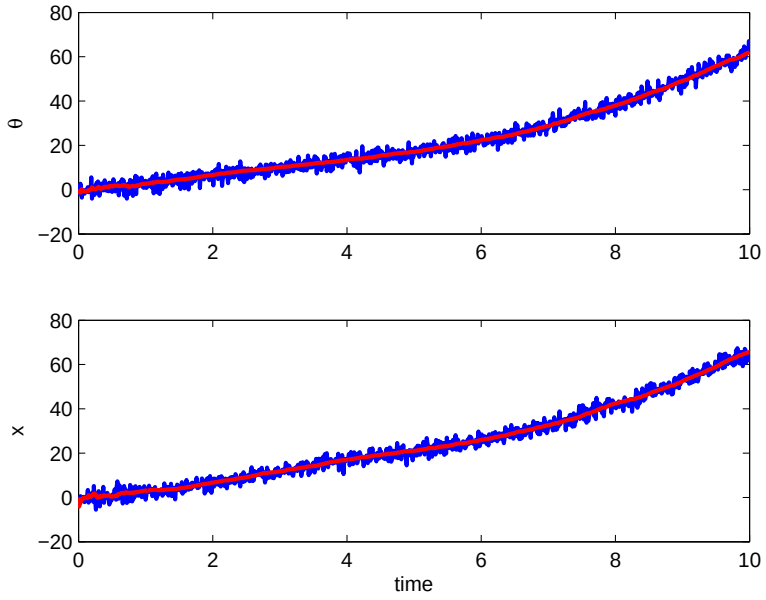

Fig. 22. Example 1: Measurements and Estimates Using Method 1.

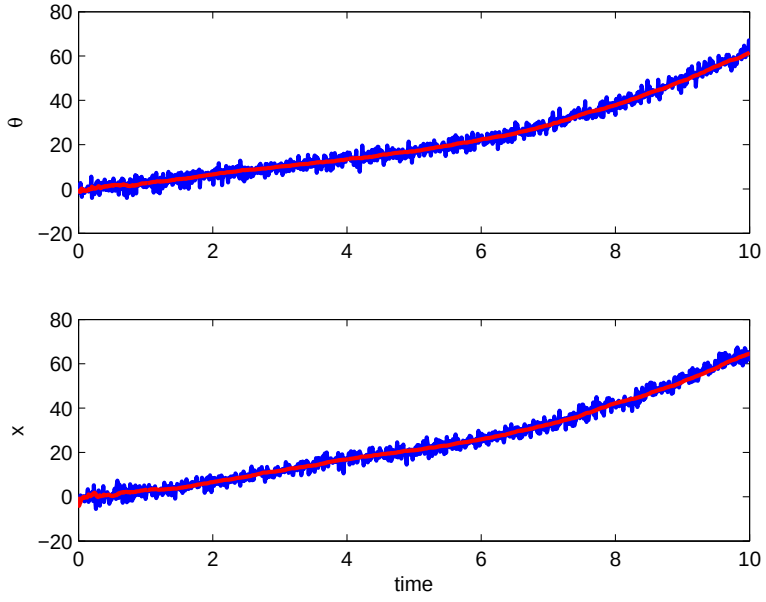

Fig. 23. Example 1: Measurements and Estimates Using Method 2.

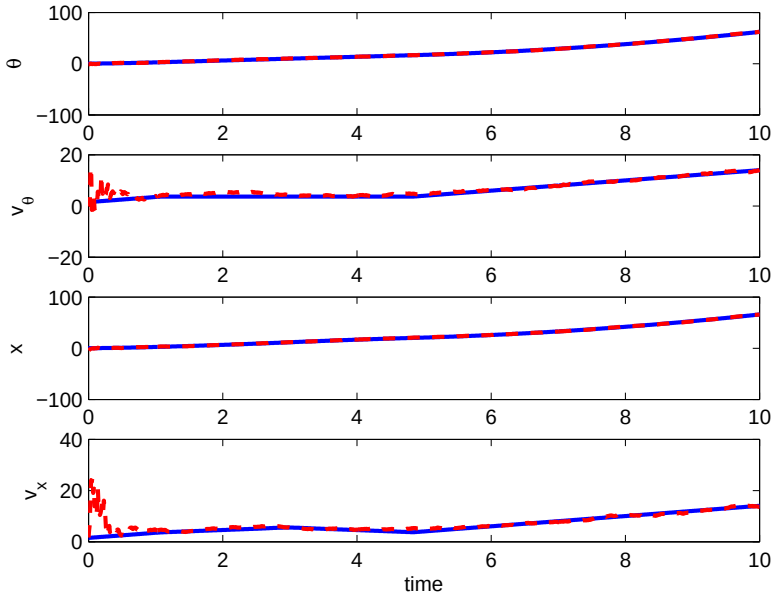

Fig. 24. Example 1: True and Estimated States Using Method 1.

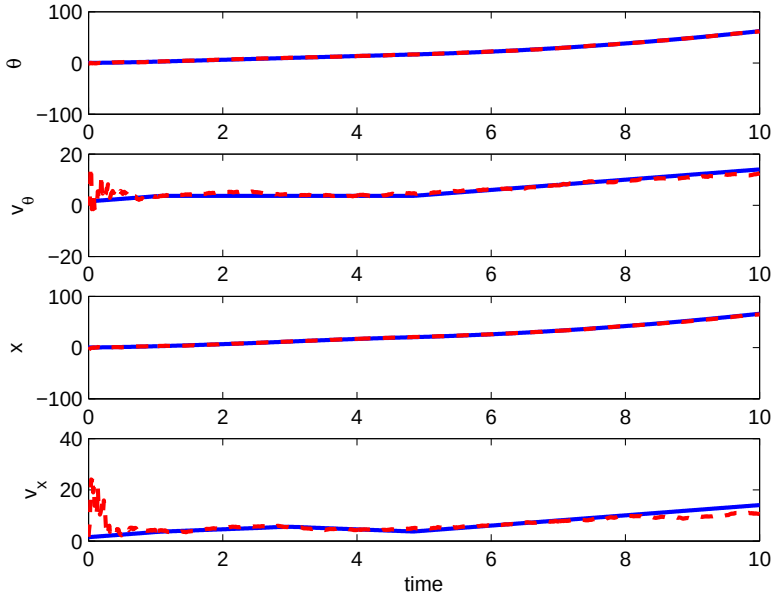

Fig. 25. Example 1: True and Estimated States Using Method 2.

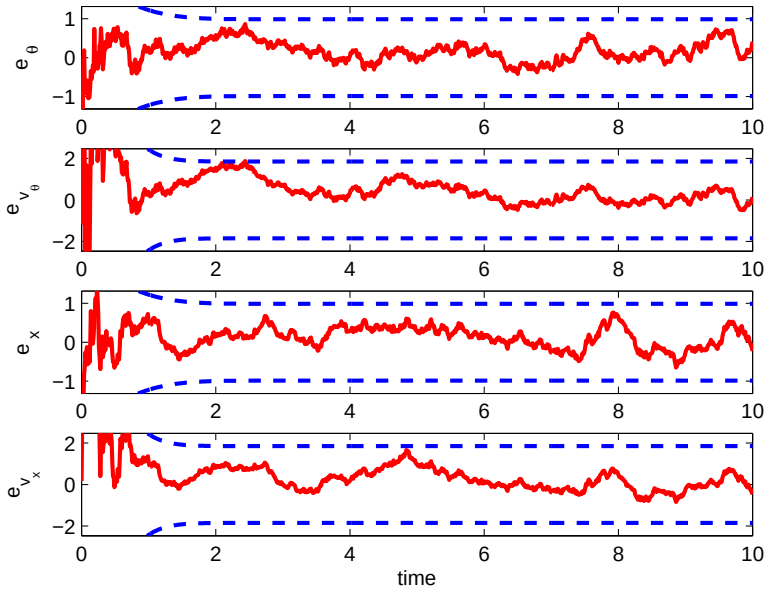

Fig. 26. Example 1: State Estimate Error with $3-\sigma$ Error Bounds Using Method 1.

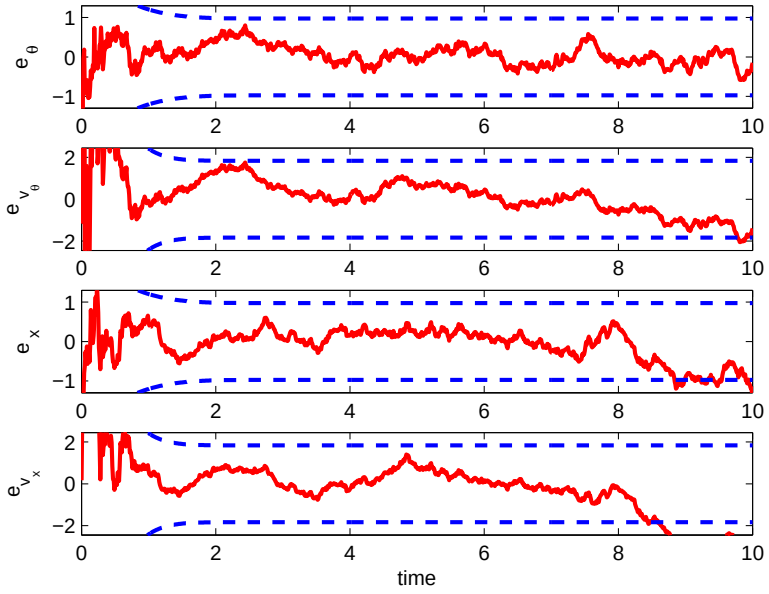

Fig. 27. Example 1: State Estimate Error with $3-\sigma$ Error Bounds Using Method 2.

2. Example 2: Asymmetric Pendulum

The second constrained system example is a variation of the classic pendulum moving in the plane under the influence of gravity. In this version, an obstacle of a semicircle is placed in the right-hand plane, as shown in Fig. 28.

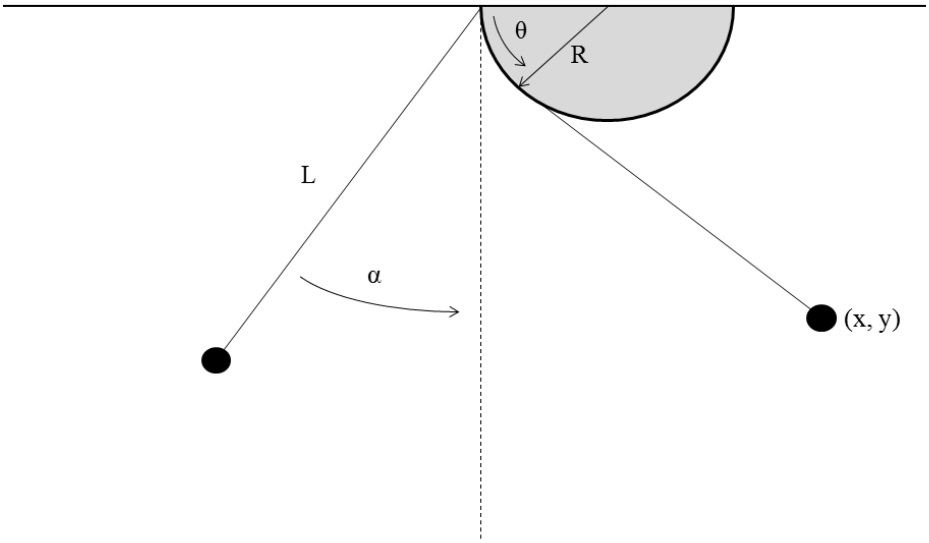

Fig. 28. Asymmetric Pendulum Illustration.

The kinematics for each half-plane are different, so the dynamics of this system must be modeled separately for each side. First, the right-hand side is considered. The pendulum position in the right-half plane can be described with the following vector.

$$\begin{aligned} \boldsymbol{r} &= (R - R\cos\theta + (L - R\theta)\sin\theta)\,\hat{\boldsymbol{i}} + (-R\sin\theta - (L - R\theta)\cos\theta)\,\hat{\boldsymbol{j}} \\ &= x\hat{\boldsymbol{i}} + y\hat{\boldsymbol{j}} \end{aligned} \tag{5.13}$$

Equating the terms along the horizontal and vertical axes results in two holonomic constraints.

$$\begin{aligned}\phi_1 =& x - R + R\cos\theta - (L - R\theta)\sin\theta = 0\\ \phi_2 =& y + R\sin\theta + (L - R\theta)\cos\theta = 0\end{aligned} \tag{5.14}$$

Employing the range space method described in Ch. II with these constraints gives the equations of motion.

$$\begin{aligned}\ddot{x} =& -(L - R\theta)\dot{\theta}^2\sin\theta - g\sin\theta\cos\theta\\ \ddot{y} =& (L - R\theta)\dot{\theta}^2\cos\theta - g\sin^2\theta\\ \ddot{\theta} =& \frac{1}{L - R\theta}\left(R\dot{\theta}^2 - g\sin\theta\right)\end{aligned} \tag{5.15}$$

In the left-hand plane, the position vector is as follows.

$$\begin{aligned}\boldsymbol{r} =& L\sin\alpha\hat{\boldsymbol{i}} - L\cos\alpha\hat{\boldsymbol{j}}\\ =& x\hat{\boldsymbol{i}} + y\hat{\boldsymbol{j}}\end{aligned} \tag{5.16}$$

Again equating the terms along the $\hat{\boldsymbol{i}}$ and $\hat{\boldsymbol{j}}$ axes yields two different holonomic constraints for the left-hand plane.

$$\begin{aligned}\phi_1 =& x - L\sin\alpha = 0\\ \phi_2 =& y + L\cos\alpha = 0\end{aligned} \tag{5.17}$$

These constraints can be combined into a single constraint: $x^2 + y^2 = L^2$. Applying Lagrange's equations for constrained systems, the governing equations for the left-

hand side result.

$$\begin{aligned} \ddot{x} &= -\frac{x}{L^2}\left(\dot{x}^2+\dot{y}^2\right)+\frac{gxy}{L^2} \\ \ddot{y} &= -\frac{y}{L^2}\left(\dot{x}^2+\dot{y}^2\right)-\frac{gx^2}{L^2} \\ \ddot{\alpha} &= \frac{-g\sin\alpha}{L} \end{aligned} \tag{5.18}$$

Note that, as the two angles θ and α approach zero, the two dynamical models converge to the same equations with $\alpha = \theta$. For the simulations, this property is utilized to simplify the transition between models. Thus $\theta = \alpha$ for $\theta < 0$ in the forthcoming plots. One additional consideration is nature of the term $(L - R\theta)$, which dominates the expressions for the constraint and constraint variance. When the pendulum first enters the left-half plane and constraint violation has not yet been detected, θ becomes negative and a consequence is $(L - R\theta) > L$, which is physically impossible for this system. Thus, in implementation, $(L - R|\theta|)$ is used to compute the values for the constraint and constraint variance for both methods.

For these numerical results, $R = 1$, $L = 3$, and $g = 10$. The initial position and velocity estimates are constructed using the constraints with $\theta(t_0) = \pi/3$ rad and $\dot{\theta}(t_0) = 1.5$ rad/s. A small amount of error, 5%, is applied to allow the configuration coordinates to remain nearly "constraint compatible", but still be imperfect guesses. The two measurement sources are only the x and y coordinates, but all six states are filtered. The initial state estimate covariance matrix is $P_k(t_0) = 50I$, where I is the identity matrix, and the process error covariance matrix is a diagonal matrix with entries $\text{diag}(Q) = [0.0025,\ 0.1,\ 0.05,\ 0.01,\ 0.05,\ 0.01]$. The measurement error for both states is $\sigma_{y_m} = 0.05$, and R_k is constructed as in Example 1.

For this example, two constraints are being considered. The logic employed to account for multiple constraints is modified accordingly with L and R indicating the left- and right-hand side models.

$|\hat{\phi}_k| = \text{mean}([|\hat{\phi}_{1k}|, |\hat{\phi}_{1k}|])$

$\sigma_{\phi_k} = \text{mean}([\sigma_{\phi_{1k}}, \sigma_{\phi_{1k}}])$

If $|\hat{\phi}_k| > \sigma_{\phi_k}$,

$$\dot{\boldsymbol{q}}_L = \boldsymbol{f}_L(\boldsymbol{q}, t)$$

Else

$$\dot{\boldsymbol{q}}_R = \boldsymbol{f}_R(\boldsymbol{q}, t)$$

End

The simulation results in Figs. 29-48 show that both Method 1 and Method 2 can successfully switch between the two models and effectively filter the six states. Through significant process noise tuning effort, the performance of Method 2 can be increased to be nearly comparable to that of Method 1. Note that Method 2 is again found to be very sensitive to the values of the process noise chosen for Q_{ϕ_1} and Q_{ϕ_2}. Here, each is equal to one. The combination of (1) less computational complexity and (2) less sensitivity to process noise recommends Method 1 as a more advantageous approach to constraint monitoring in the CDEKF estimation framework than Method 2. For the remaining examples of greater complexity, Method 1 alone is applied.

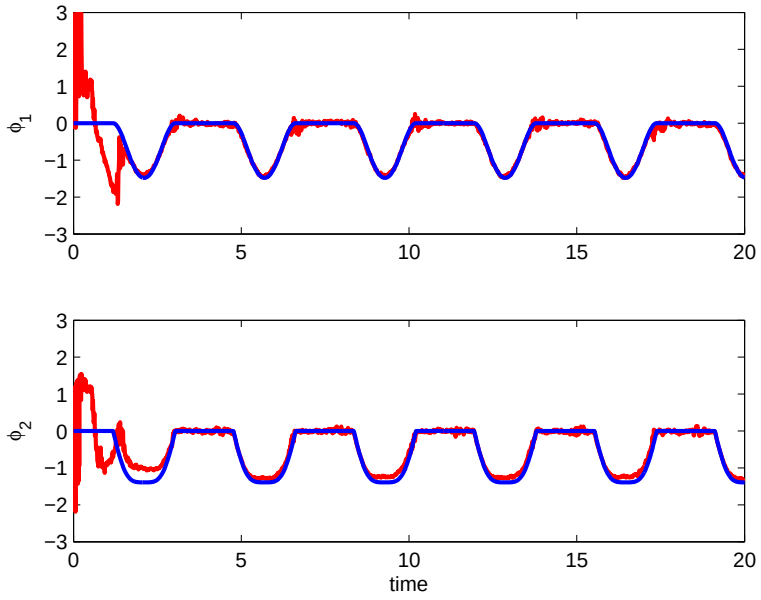

Fig. 29. Example 2: True and Estimated Constraint Value Using Method 1.

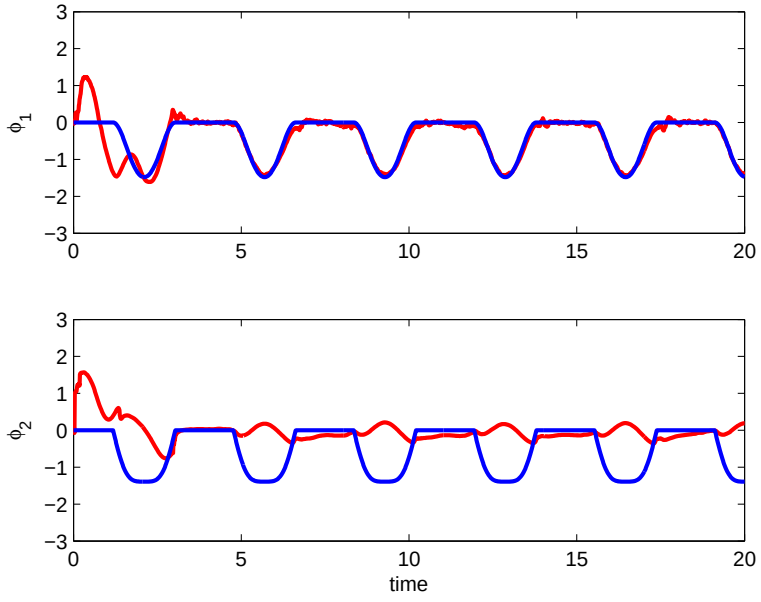

Fig. 30. Example 2: True and Estimated Constraint Value Using Method 2.

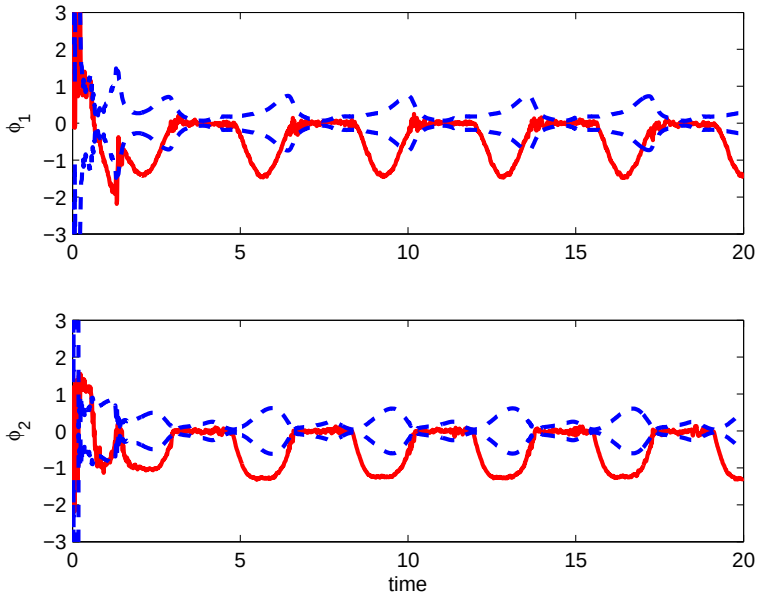

Fig. 31. Example 2: Constraint Estimate with $1-\sigma$ Error Bounds Using Method 1.

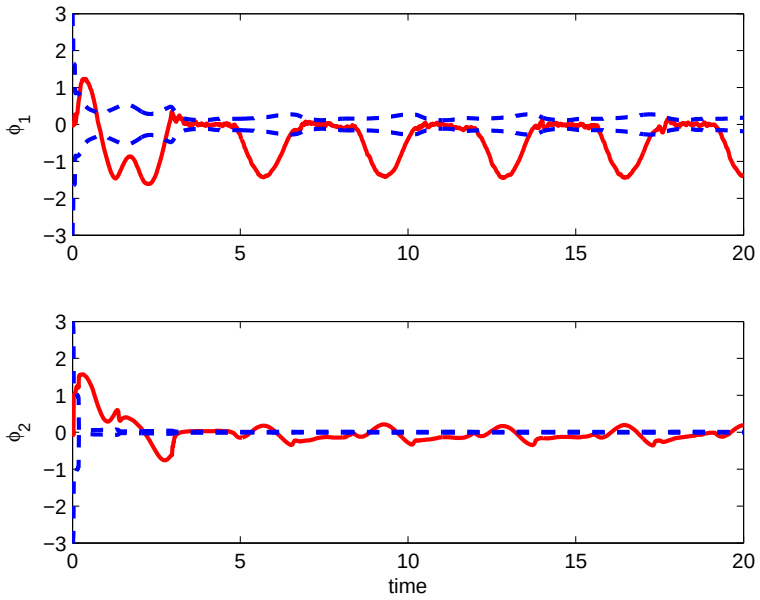

Fig. 32. Example 2: Constraint Estimate with $1-\sigma$ Error Bounds Using Method 2.

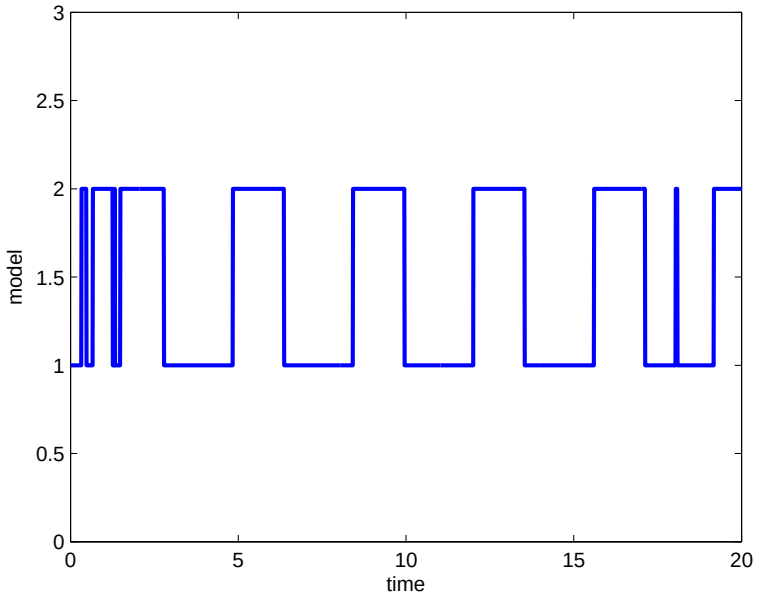

Fig. 33. Example 2: Model Time History Using Method 1.

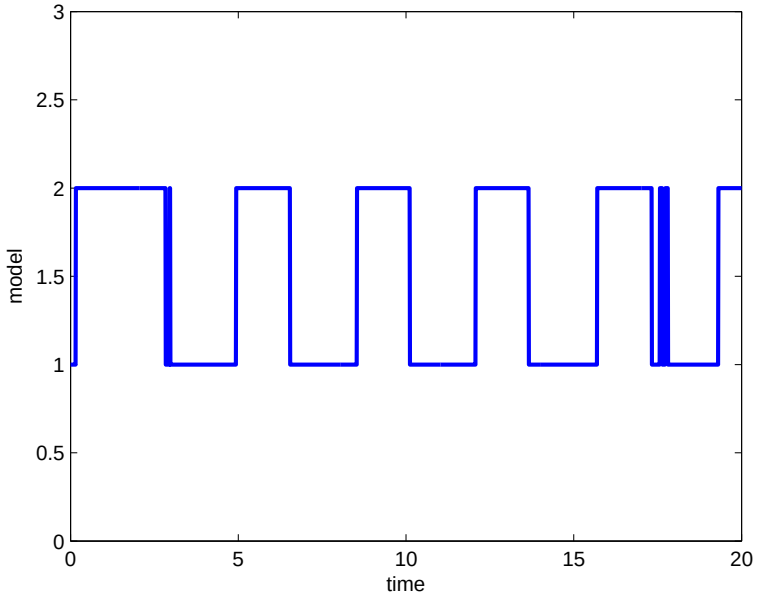

Fig. 34. Example 2: Model Time History Using Method 2.

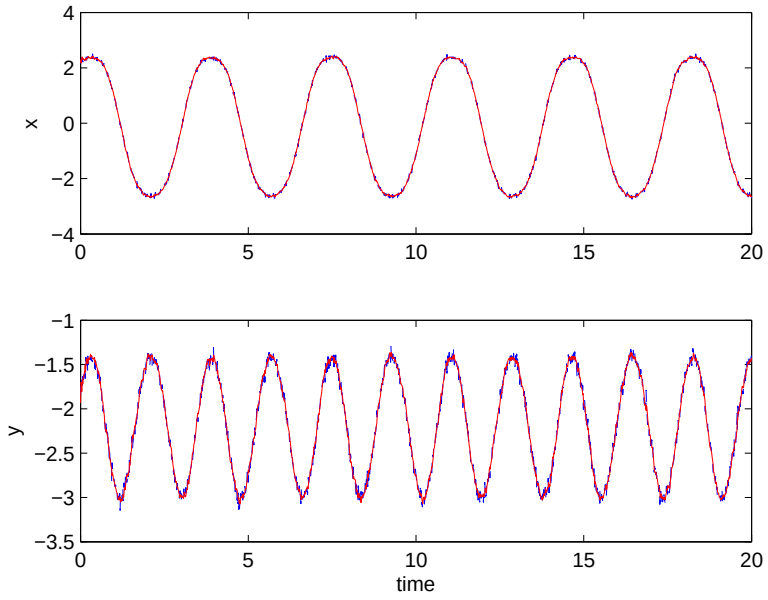

Fig. 35. Example 2: Measurements and Estimates Using Method 1.

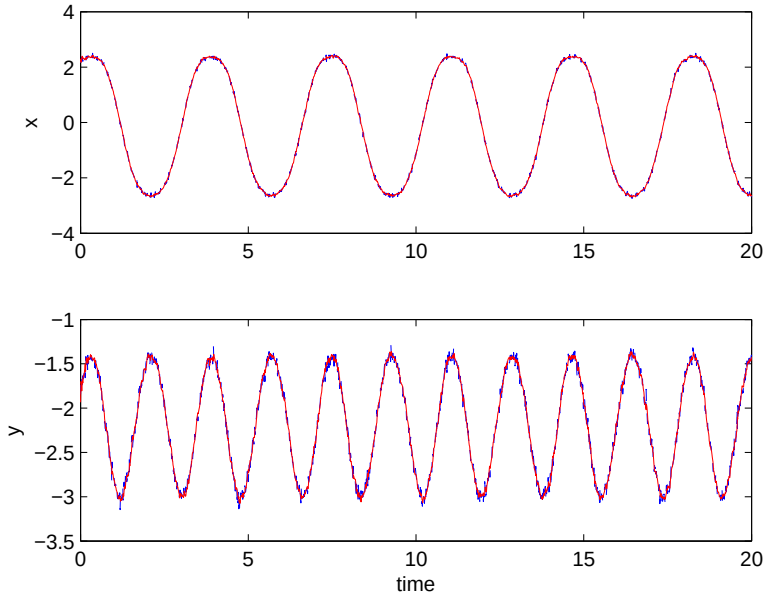

Fig. 36. Example 2: Measurements and Estimates Using Method 2.

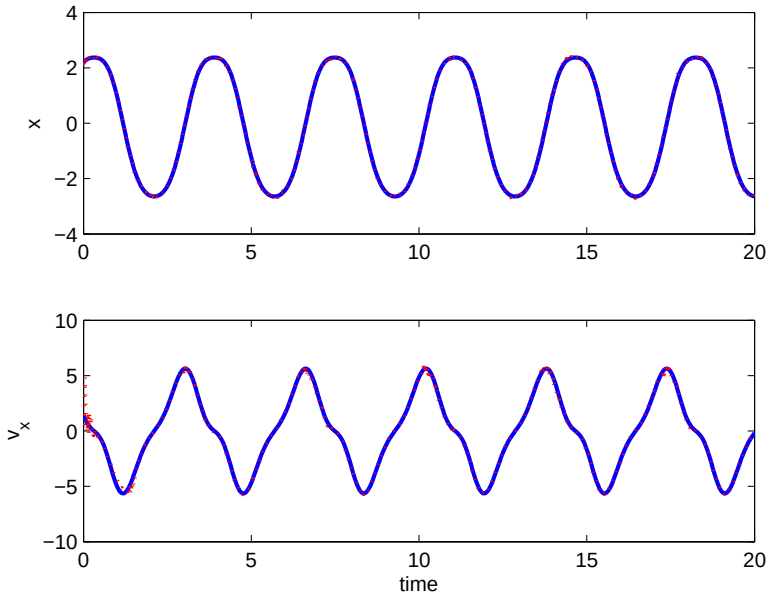

Fig. 37. Example 2: True and Estimated x States Using Method 1.

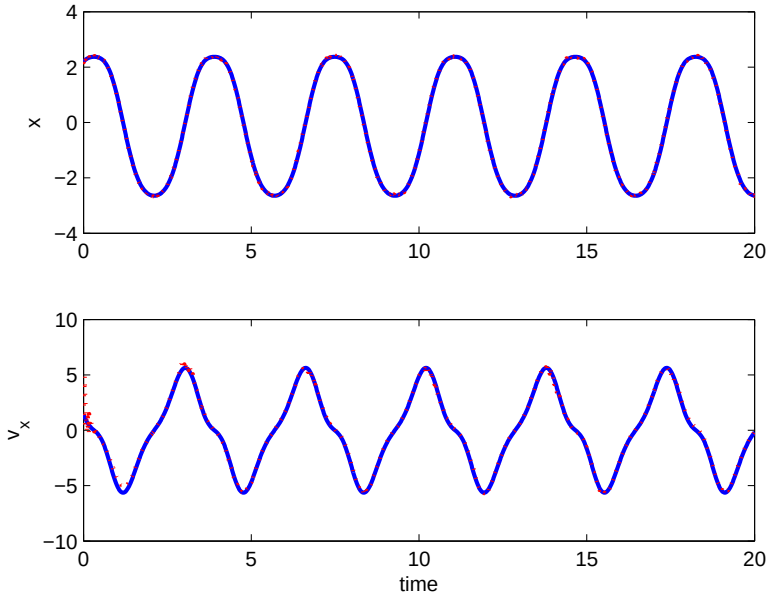

Fig. 38. Example 2: True and Estimated x States Using Method 2.

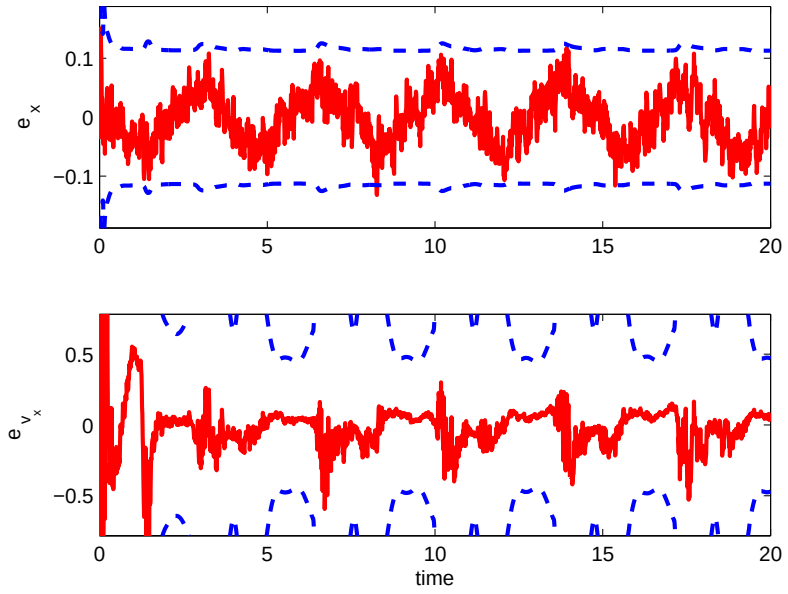

Fig. 39. Example 2: x State Estimate Error with $3-\sigma$ Error Bounds Using Method 1.

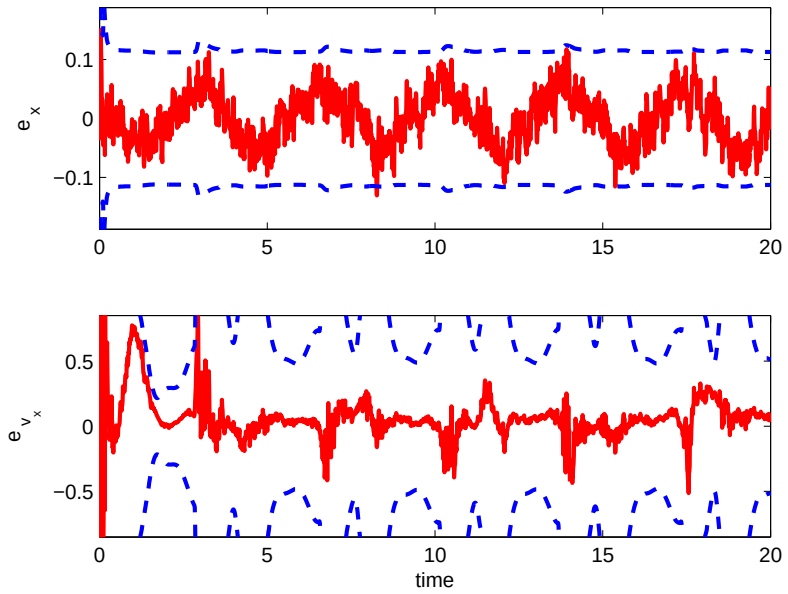

Fig. 40. Example 2: x State Estimate Error with $3-\sigma$ Error Bounds Using Method 2.

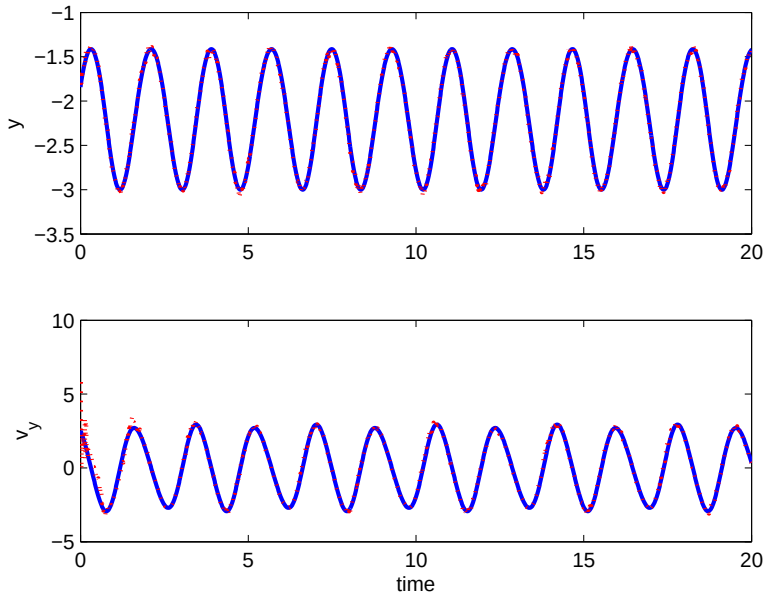

Fig. 41. Example 2: True and Estimated y States Using Method 1.

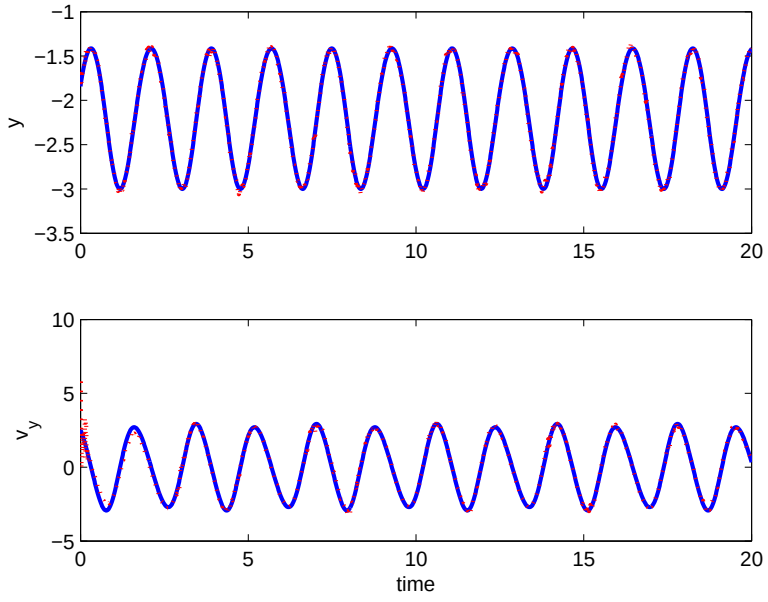

Fig. 42. Example 2: True and Estimated y States Using Method 2.

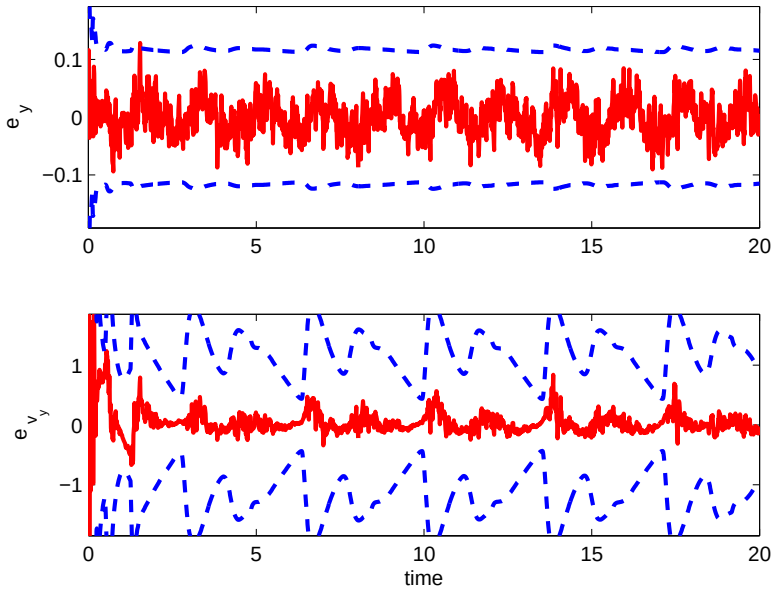

Fig. 43. Example 2: y State Estimate Error with $3-\sigma$ Error Bounds Using Method 1.

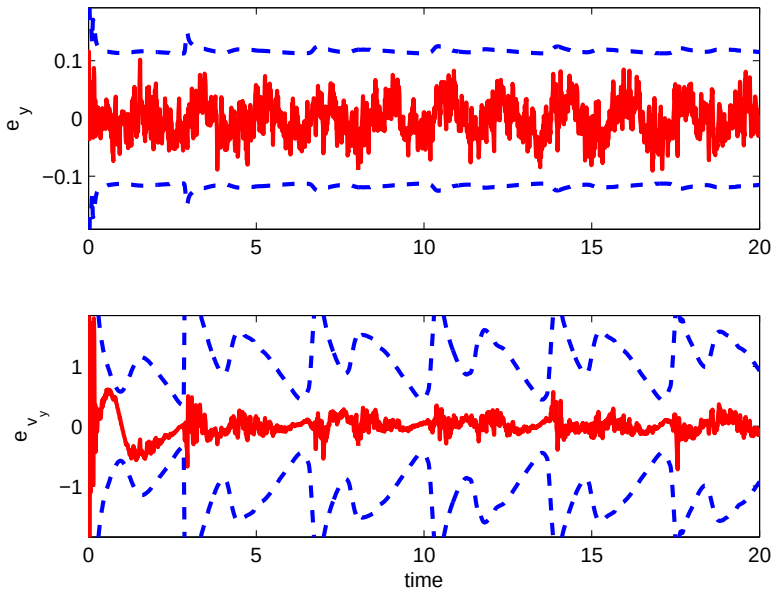

Fig. 44. Example 2: y State Estimate Error with $3-\sigma$ Error Bounds Using Method 2.

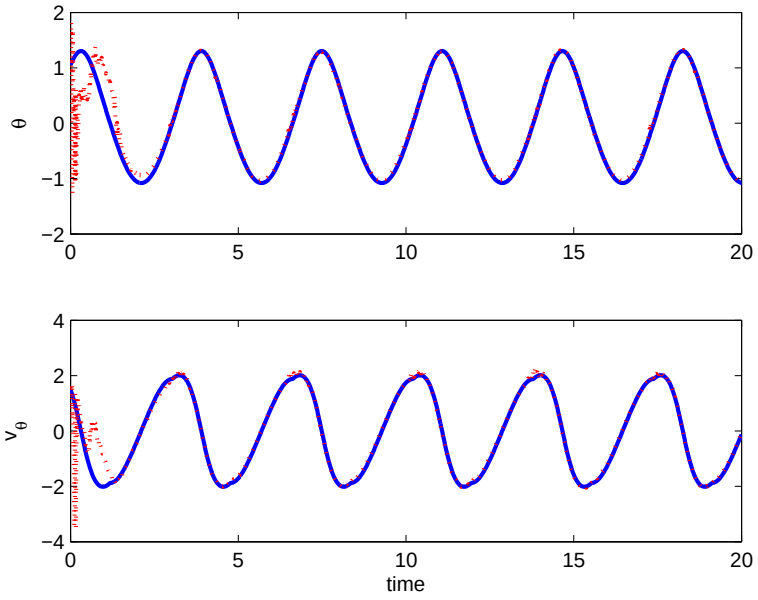

Fig. 45. Example 2: True and Estimated θ States Using Method 1.

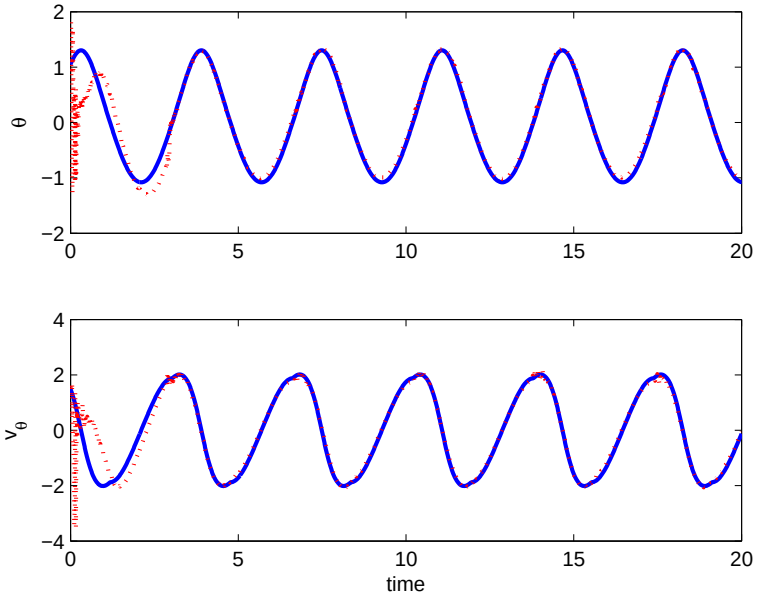

Fig. 46. Example 2: True and Estimated θ States Using Method 2.

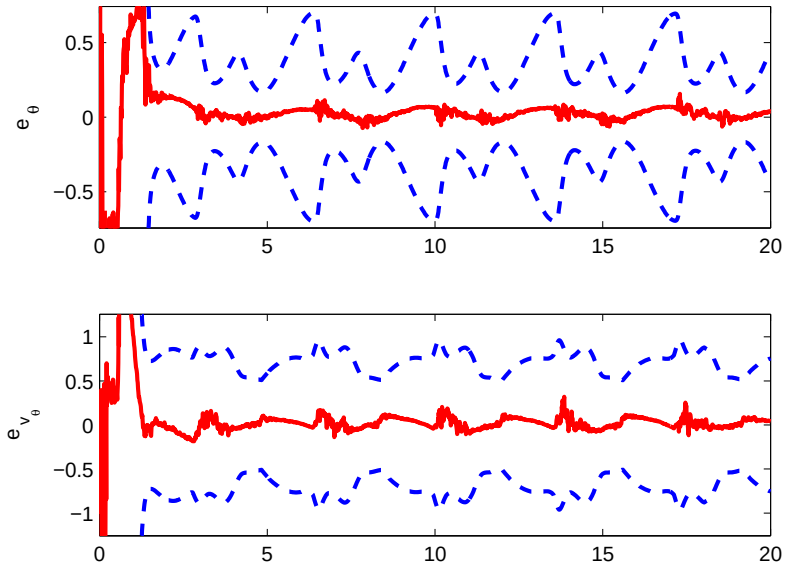

Fig. 47. Example 2: θ State Estimate Error with $3-\sigma$ Error Bounds Using Method 1.

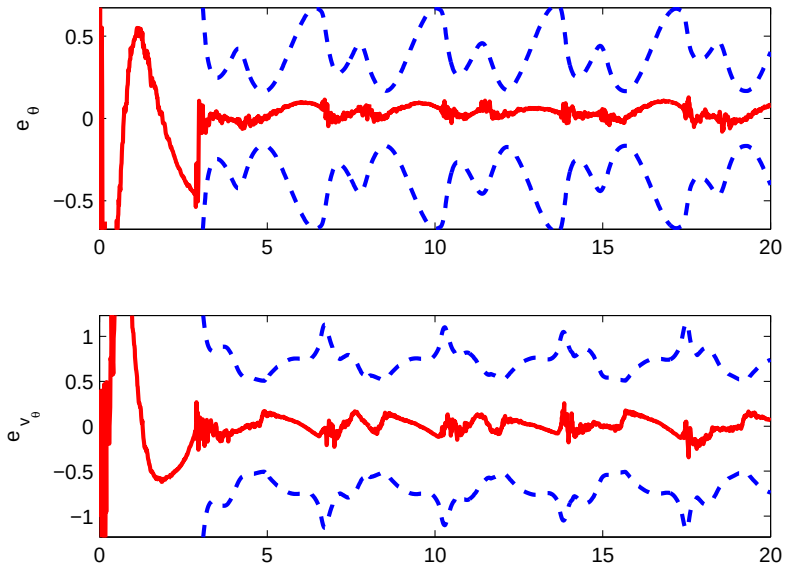

Fig. 48. Example 2: θ State Estimate Error with $3-\sigma$ Error Bounds Using Method 2.

3. Example 3: Planar Vehicle

For example 3, consider a planar vehicle subject to a "no sideslip" constraint, such as an ice skate or the sled of Fig. 1 from Ch. III. For this problem, recall the position-level kinematics in both cartesian and polar coordinates.

$$\boldsymbol{r} = x\hat{\boldsymbol{i}} + y\hat{\boldsymbol{j}} = r\hat{\boldsymbol{b}}_1 \tag{5.19}$$

The frame-independent time derivative gives the velocity-level kinematics.

$$\begin{aligned}\dot{\boldsymbol{r}} &= \dot{x}\hat{\boldsymbol{i}} + \dot{y}\hat{\boldsymbol{j}} \\ &= \dot{r}\hat{\boldsymbol{b}}_1 + r\dot{\theta}\hat{\boldsymbol{b}}_2 \\ &= (\dot{x}\cos\theta + \dot{y}\sin\theta)\,\hat{\boldsymbol{b}}_1 + (\dot{y}\cos\theta - \dot{x}\sin\theta)\,\hat{\boldsymbol{b}}_2\end{aligned} \tag{5.20}$$

Here, the body-fixed axis $\hat{\boldsymbol{b}}_1$ is aligned with the forward motion of the vehicle, and $\hat{\boldsymbol{b}}_2$ is in the plane and orthogonal to this motion. Setting the velocity along the $\hat{\boldsymbol{b}}_2$ axis equal to zero to enforce no sideslip, the following form of the constraint results.

$$\phi = \dot{y}\cos\theta - \dot{x}\sin\theta = 0 \tag{5.21}$$

The following equations of motion result by applying Lagrange's equations for constrained systems.

$$\begin{aligned} m\ddot{x} &= T\cos\theta + C_x\lambda \\ m\ddot{y} &= T\sin\theta + C_y\lambda \\ I\ddot{\theta} &= u + C_\theta\lambda \end{aligned} \tag{5.22}$$

The constraint influence matrix relates the constraints and generalized velocities.

$$C = [-\sin\theta,\, \cos\theta,\, 0]^T \tag{5.23}$$

Using the range space method outlined in Ch. II, the solution for the Lagrange multiplier can be found.

$$\lambda = m\dot{\theta}\left(\dot{y}\sin\theta + \dot{x}\cos\theta\right) \tag{5.24}$$

When the constraint is violated, it is assumed that sliding friction, modeled as $F = -\mu mg$, opposes the motion in the $\hat{\boldsymbol{b}}_2$ direction, but the vehicle can still move without opposing friction in the $\hat{\boldsymbol{b}}_1$ direction. The unconstrained equations of motion can be derived using the familiar form of Lagrange's equations.

$$\begin{aligned} m\ddot{x} &= T\cos\theta + F\sin\theta \\ m\ddot{y} &= T\sin\theta - F\cos\theta \\ I\ddot{\theta} &= u \end{aligned} \tag{5.25}$$

For the following simulation results, the thrust T along the $\hat{\boldsymbol{b}}_1$ axis and torque u about the out of plane axis are designed to first accelerate the vehicle and then cause it to turn sharply. During this turn, the vehicle "loses traction" and experiences sideslip before decelerating and re-engaging the constraint. The vehicle has mass $m = 50$ and inertia $I = 50$. The sliding friction coefficient is $\mu = 0.05$, and gravity has the value $g = 10$. The initial coordinates are $x = 10$, $y = 10$, and $\theta = 0$ with no initial angular velocity and initial forward velocity of 5.

The initial guesses of the state estimates are given 10% error. The measurements x, y, and θ for $0 < t < 200$ have measurement error $\sigma_{y_m} = [1.5,\ 1.5,\ .01]$, respectively. The square of these values are the elements of the diagonal matrix R_k. The process noise covariance matrix applied is given by $Q = \text{diag}[.2,\ .1,\ .2,\ .1,\ .001,\ .001]$, and the initial state estimate covariance matrix is $P_k(t_0) = 100I$, where I is the identity matrix.

The estimation results show that Method 1 works very well for this system, as shown in Fig. 49-58. The slight differential from the initial error bounds that occurs after the constraint is re-engaged (see Fig. 54, 56 and 58) is likely due to the system model (rather than Method 1 or the CDEKF). One difficulty of simulating multi-model systems (i.e., constrained $\rightarrow$ unconstrained $\rightarrow$ constrained) for use as measurements is the design of a simple open-loop control that drives the system states back to a constraint-compatible configuration after the constraint has been violated. For these measurements, the system is driven to a *nearly* constraint-compatible configuration ($\phi < 10^{-6}$).

Though the physical system is difficult to model well mathematically, this model of the system is a particularly good candidate for constraint monitoring because (1) the average non-zero constraint value is much greater than the associated error bound and (2) the system is unconstrained for a substantial time period, as shown in Fig. 49 and 50. These characteristics allow the unconstrained model to be utilized more quickly and to subsequently lend greater effectiveness to the CDEKF by providing a more appropriate model of the true dynamics for the time period that the system is unconstrained.

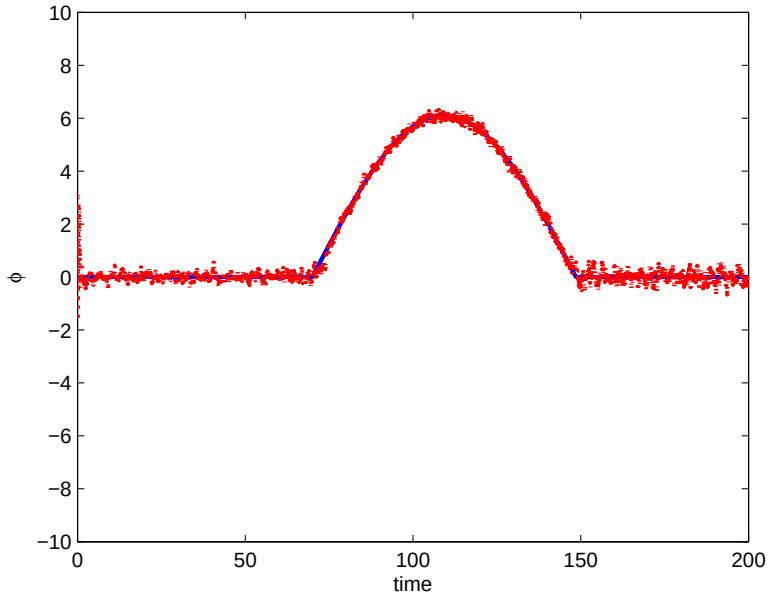

Fig. 49. Example 3: True and Estimated Constraint Value.

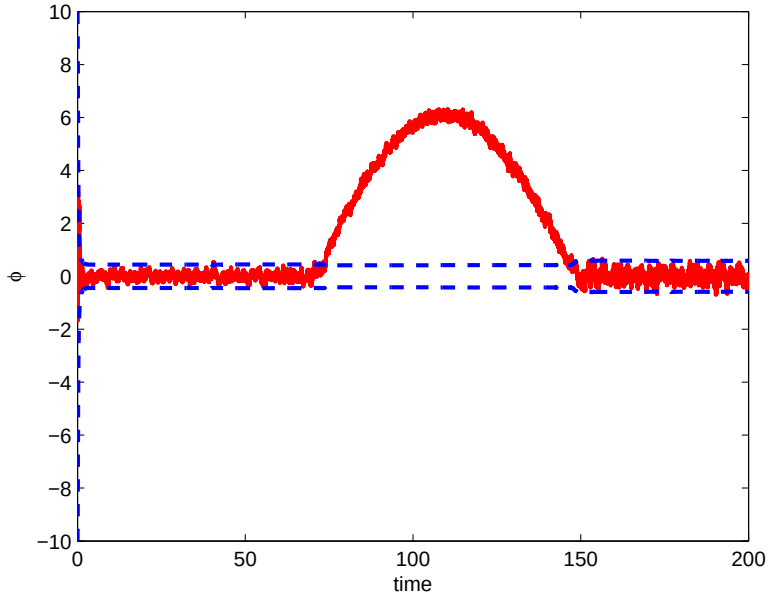

Fig. 50. Example 3: Constraint Estimate with $1 - \sigma$ Error Bounds.

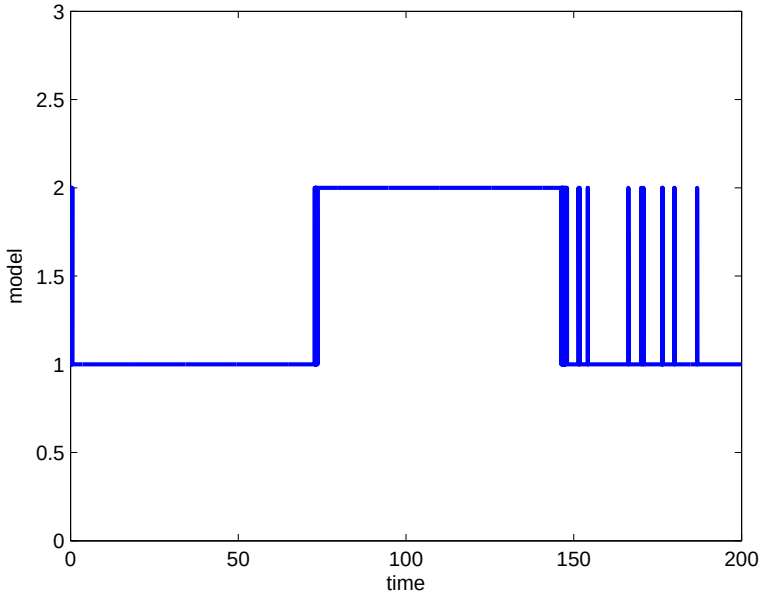

Fig. 51. Example 3: Model Time History.

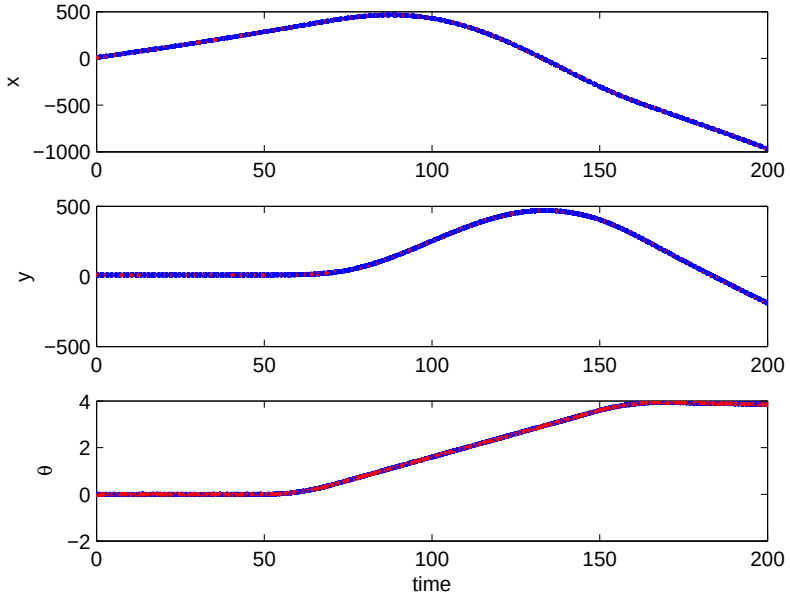

Fig. 52. Example 3: Measurements and Estimates.

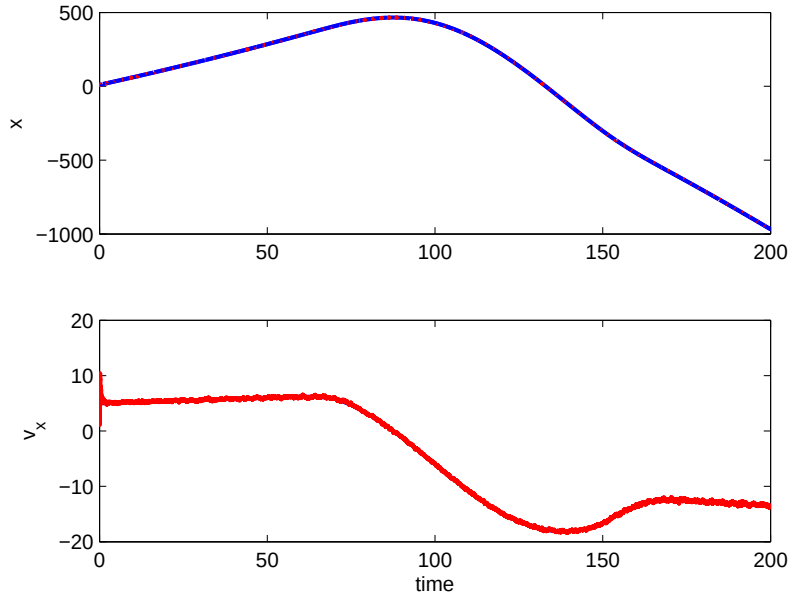

Fig. 53. Example 3: True and Estimated x States.

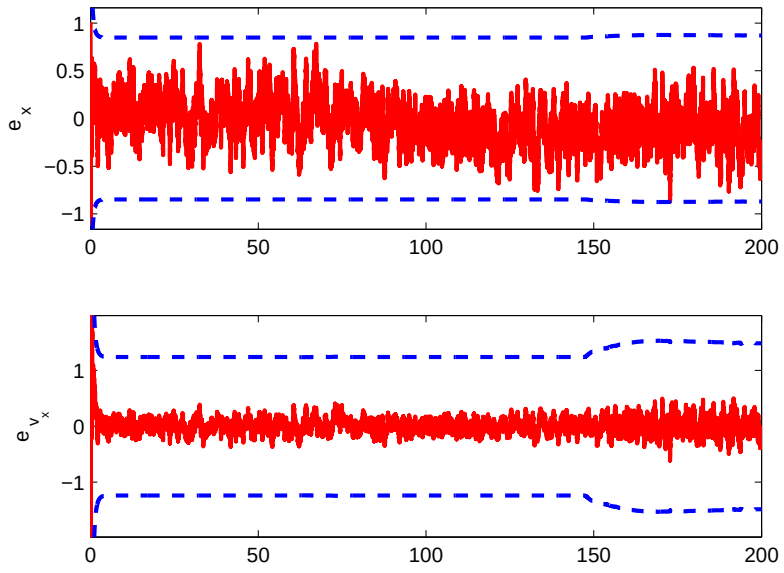

Fig. 54. Example 3: x State Estimate Error with $3-\sigma$ Error Bounds.

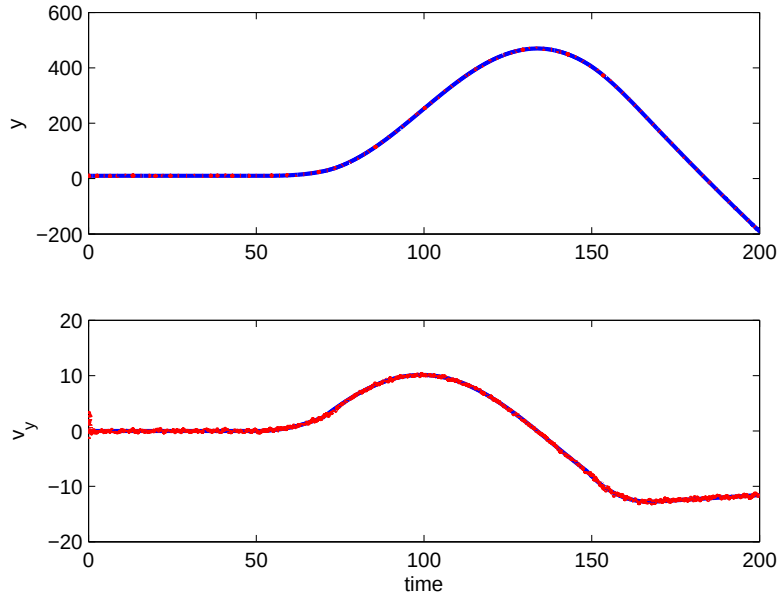

Fig. 55. Example 3: True and Estimated y States.

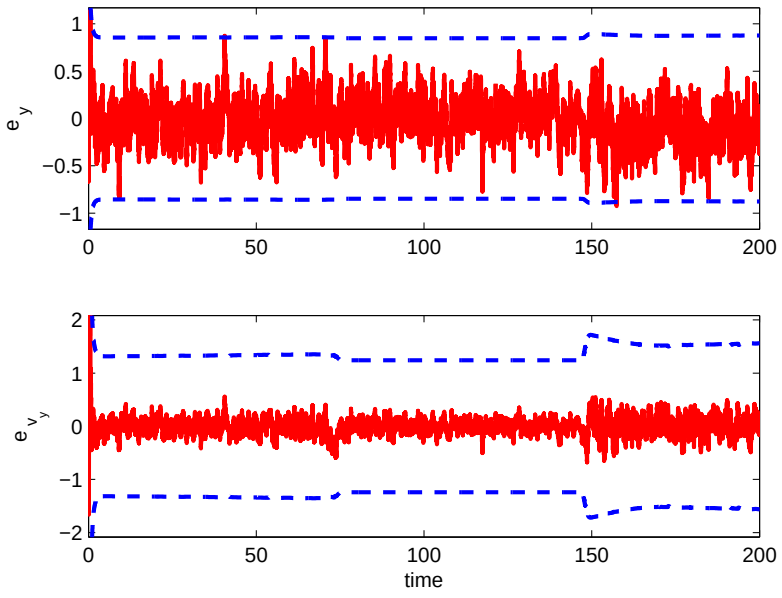

Fig. 56. Example 3: y State Estimate Error with $3-\sigma$ Error Bounds.

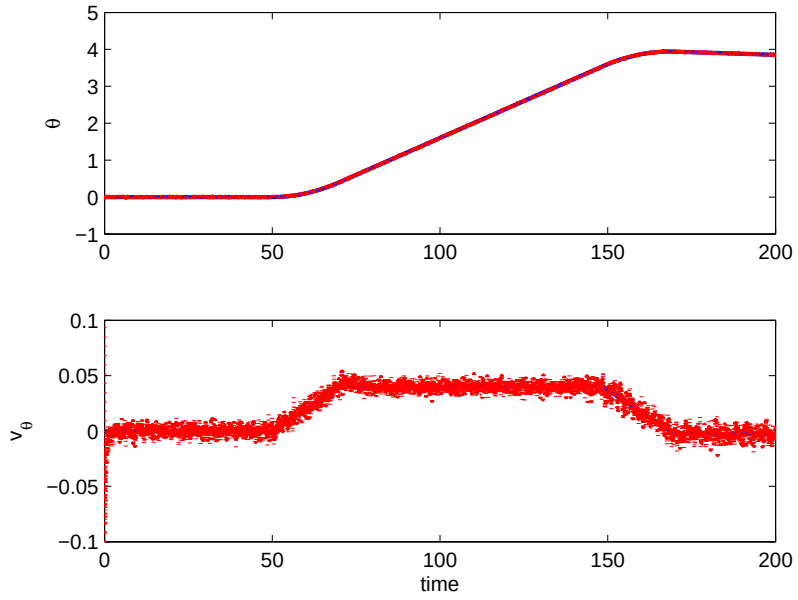

Fig. 57. Example 3: True and Estimated θ States.

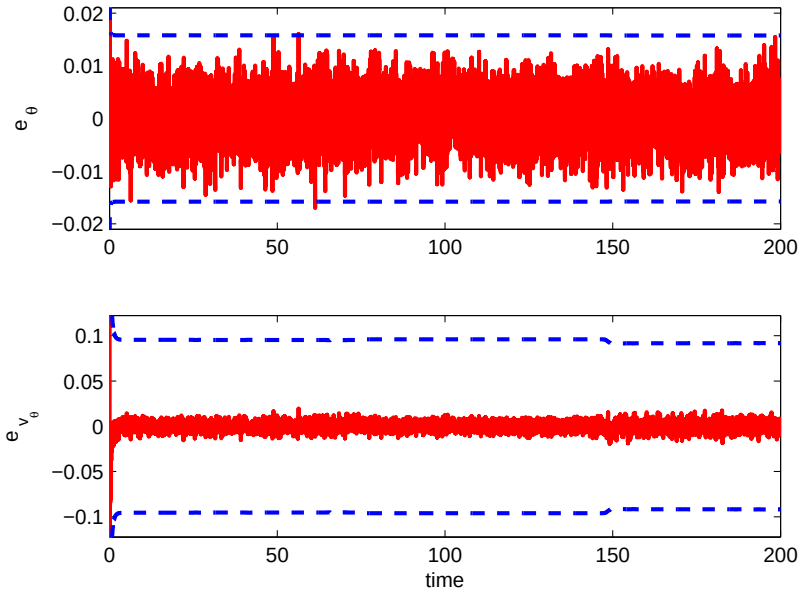

Fig. 58. Example 3: θ State Estimate Error with $3-\sigma$ Error Bounds.

4. Example 4: Tethered Satellite System

For a more complex example with a nonlinear constraint, a tethered satellite system is investigated. This system consists of two satellites orbiting the Earth that are connected by a tether. Here, the tether is modeled as a massless, rigid rod of length L and gravitational effects other than that of the Earth are neglected. The polar coordinates used to describe the kinematics of the two satellites are shown in Fig. 59.

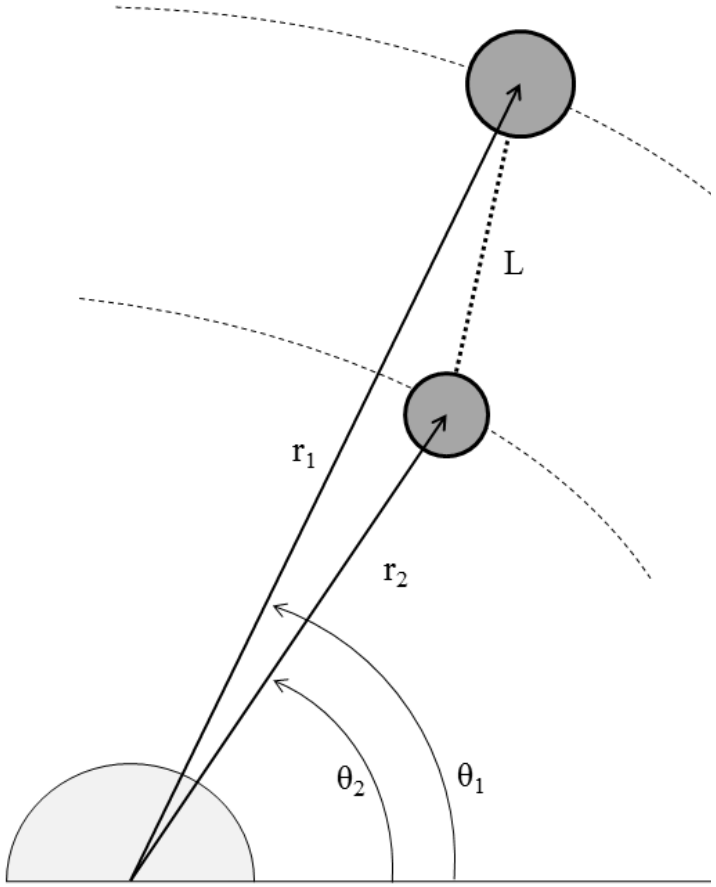

Fig. 59. Tethered Satellite System Illustration.

For each of the $i = 1, 2$ satellites, the position, velocity, and acceleration can be described using these polar coordinates.

$$\begin{aligned} \boldsymbol{r}_i &= r_i \hat{\boldsymbol{e}}_{r_i} \\ \dot{\boldsymbol{r}}_i &= \dot{r}_i \hat{\boldsymbol{e}}_{r_i} + r_i \dot{\theta}_i \hat{\boldsymbol{e}}_{\theta_i} \\ \ddot{\boldsymbol{r}}_i &= \left(\ddot{r}_i - r_i \dot{\theta}_i^2 \right) \hat{\boldsymbol{e}}_{r_i} + \left(r_i \ddot{\theta}_i + 2 \dot{r}_i \dot{\theta}_i \right) \hat{\boldsymbol{e}}_{\theta_i} \end{aligned} \tag{5.26}$$

The tether alters the satellite system motion according to the following nonlinear holonomic constraint.

$$\phi = r_1^2 + r_2^2 - 2 r_1 r_2 \cos(\theta_1 - \theta_2) - L^2 = 0 \tag{5.27}$$

The associated constraint influence matrix can be written with $\theta_{ij} = \theta_i - \theta_j$.

$$C = \begin{bmatrix} r_1 - r_2 \cos \theta_{12} \\ r_1 r_2 \sin \theta_{12} \\ r_2 - r_1 \cos \theta_{12} \\ -r_1 r_2 \sin \theta_{12} \end{bmatrix} \tag{5.28}$$

Using Lagrange's equations (with Newton's law of gravitation to construct the potential energy) yields the equations of motion.

$$\begin{aligned} \ddot{r}_1 &= r_1 \dot{\theta}_1^2 - \frac{G m_E}{m_1 r_1^2} + \frac{C_{11}}{m_1} \lambda_1 \\ \ddot{\theta}_1 &= -2 \frac{\dot{r}_1 \dot{\theta}_1}{r_1} + \frac{C_{21}}{m_1 r_1^2} \lambda_1 \\ \ddot{r}_2 &= r_2 \dot{\theta}_2^2 - \frac{G m_E}{m_2 r_2^2} + \frac{C_{31}}{m_2} \lambda_1 \\ \ddot{\theta}_2 &= -2 \frac{\dot{r}_2 \dot{\theta}_2}{r_2} + \frac{C_{41}}{m_2 r_2^2} \lambda_1 \end{aligned} \tag{5.29}$$

The range-space method can again be implemented to find the Lagrange multiplier

as a function of the states.

$$\begin{aligned}\lambda_1 = &- \frac{m_1 m_2}{L^2(m_1+m_2)}\big(r_1^2\dot{\theta}_1^2 + r_2^2\dot{\theta}_2^2 + \dot{r}_1^2 + \dot{r}_2^2 \\ &- 2(r_1\dot{\theta}_1 r_2\dot{\theta}_2 + \dot{r}_1\dot{r}_2)\cos\theta_{12} + 2(r_1\dot{\theta}_1\dot{r}_2 - r_2\dot{\theta}_2\dot{r}_1)\sin\theta_{12}\big) \\ &+ \frac{G m_E m_1 m_2}{L^2(m_1+m_2)r_1^2 r_2^2}\left(r_1^2(r_2 - r_1\cos\theta_{12} + r_2^2(r_1 - r_2\cos\theta_{12}\right)\end{aligned} \tag{5.30}$$

For this system, the unconstrained equations of motion equal the constrained equations of motion with $\lambda = 0$.

In simulation, the tethered satellite system is released, in a constraint-compatible configuration, at perigee. The parameters chosen for this study are outlined in Table I.

Table I. Tethered Satellite System Parameter Values.

Parameter	Value
c	10^4
G	6.67300×10^{-20} km^3/kg/s^2
m_{Earth}	5.9722×10^{24} kg
r_{Earth}	6371 km
L	5 km
m_1	500 kg
m_2	5 kg
$r_1(t_0)$	8376 km
$r_2(t_0)$	8371 km
$\theta_i(t_0)$	0 rad
$\dot{r}_i$	0 km/s
$\dot{\theta}_i$	8.238×10^{-4} rad/s

The orbit of the satellite system is monitored for time 0s $< t <$ 1500s, and the tether breaks at time $t = 500$s. The four configuration-level states (r_i, θ_i) are sensed, and all eight (configuration and velocity) states are estimated. The measurement noise covariance matrix is constructed as before with $\sigma_{y_m} = [1, .0001, 1, .0001]$, and the diagonal elements of the process noise covariance matrix are $Q = 10^{-10} \times$ diag[400, 400, 500, 0.04, 400, 400, 500, 0.04]. The initial state covariance matrix is $P_k(t_0) = 100I$, and the state estimates are initialized with approximately 5% error. Note that the difference in magnitudes between the radial and angular measures for this system required a scaling factor, c, to efficiently integrate the equations in the state estimate propagation equation of the CDEKF.

The plots in Figs. 60- 71 demonstrate that implementation of Method 1 constraint monitoring is effective for this system. Figures 60 and 61 show that there is some time delay in switching models as the constraint estimate moves out of the uncertainty bound. For this example, a $1.5 - \sigma$ uncertainty bound is selected due to a small bias in the constraint estimate, which is apparent in Fig. 60. A similar and potentially related bias is reflected in the θ_i estimate error in Figs. 67 and 71. This bias reflects the angular difference θ_{ij} that appears throughout the system model equations of motion (i.e., the angles do not appear independently). The bias is therefore likely a consequence of the coordinate choice for the system model and not a reflection on the proposed method or the CDEKF.

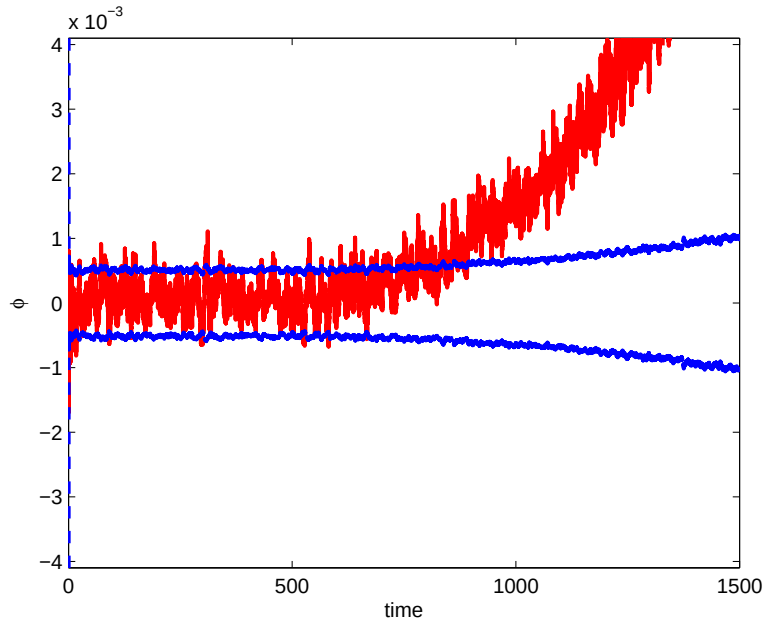

Fig. 60. Example 4: Constraint Estimate with $1-\sigma$ Error Bounds.

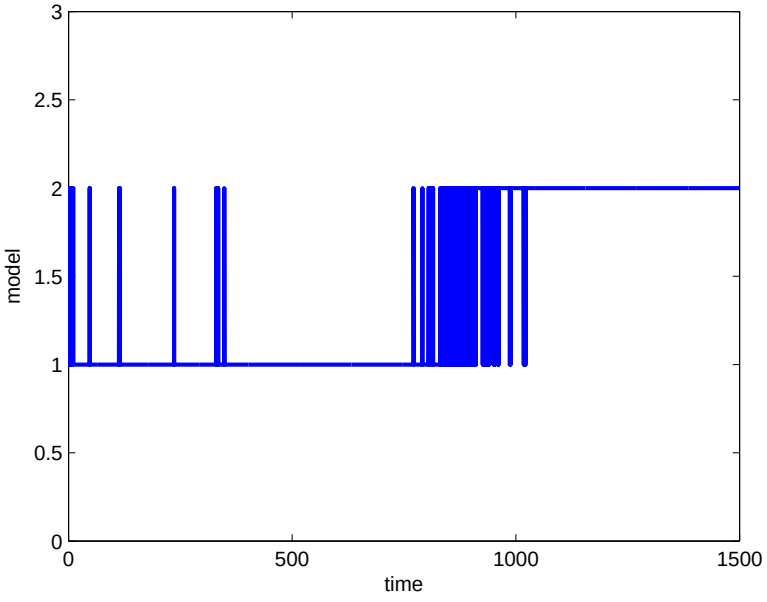

Fig. 61. Example 4: Model Time History

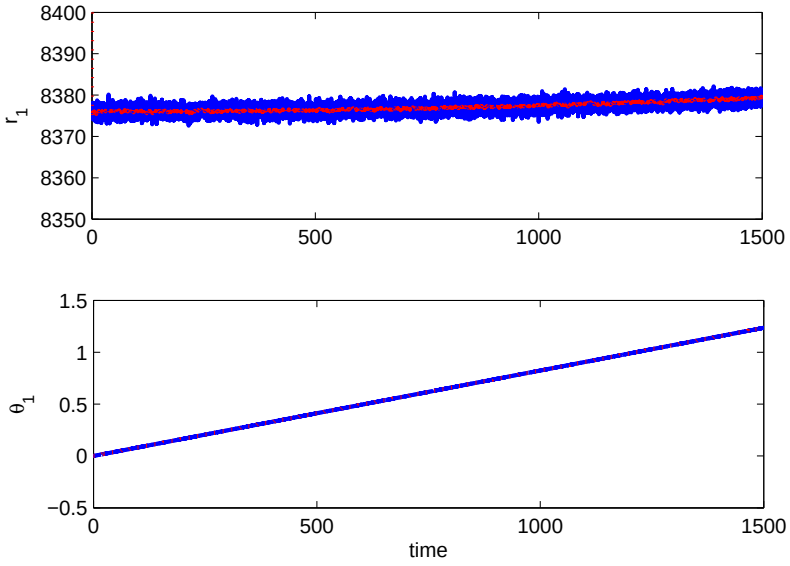

Fig. 62. Example 4: Measurements and Estimates for Satellite 1.

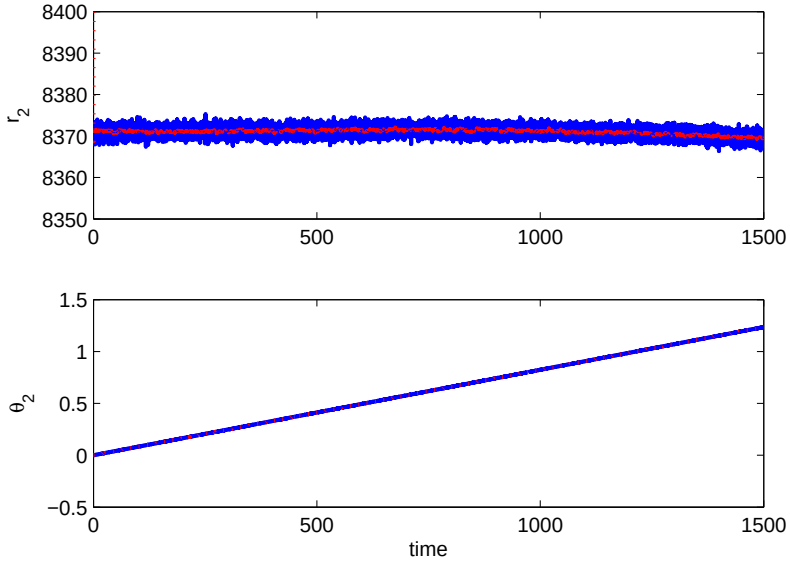

Fig. 63. Example 4: Measurements and Estimates for Satellite 2.

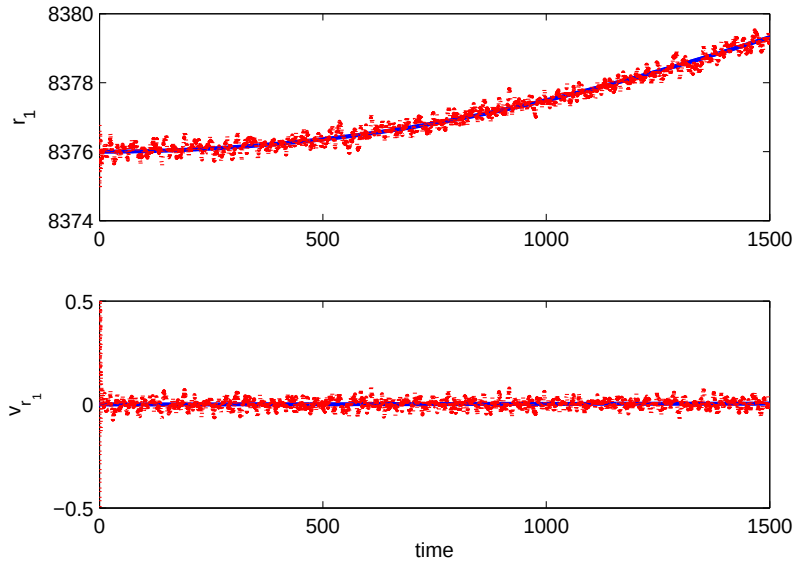

Fig. 64. Example 4: True and Estimated r_1 States.

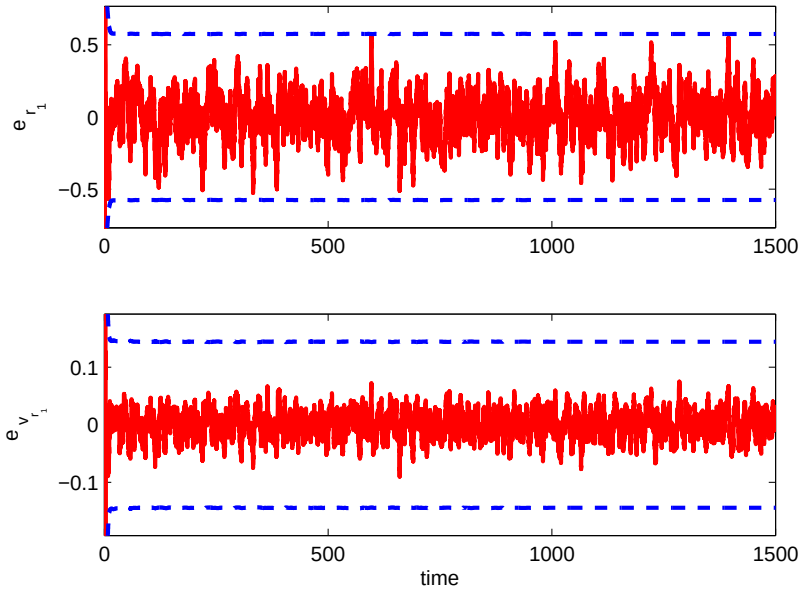

Fig. 65. Example 4: r_1 State Estimate Error with $3-\sigma$ Error Bounds.

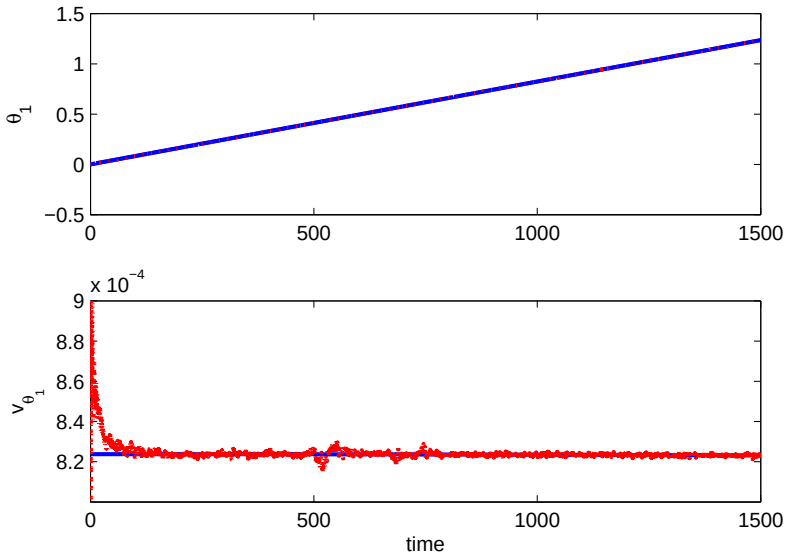

Fig. 66. Example 4: True and Estimated θ_1 States.

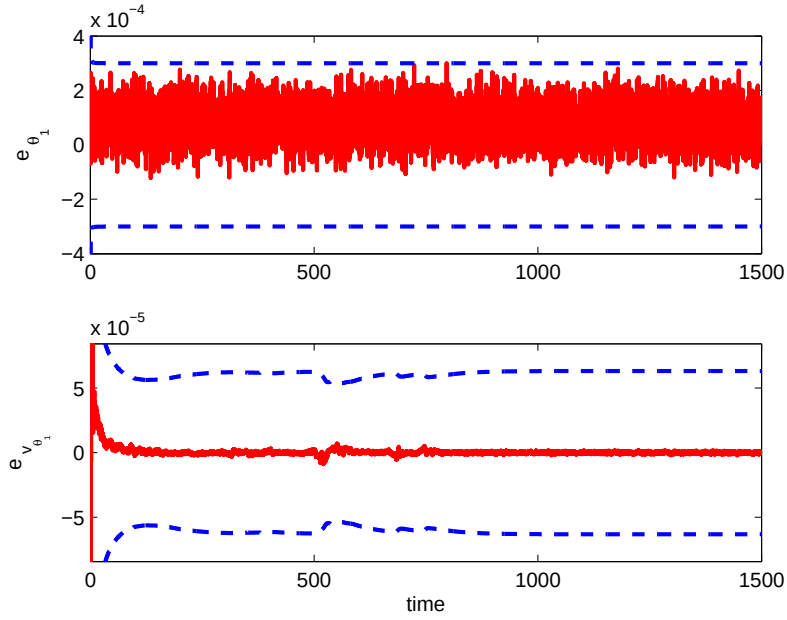

Fig. 67. Example 4: θ_1 State Estimate Error with $3-\sigma$ Error Bounds.

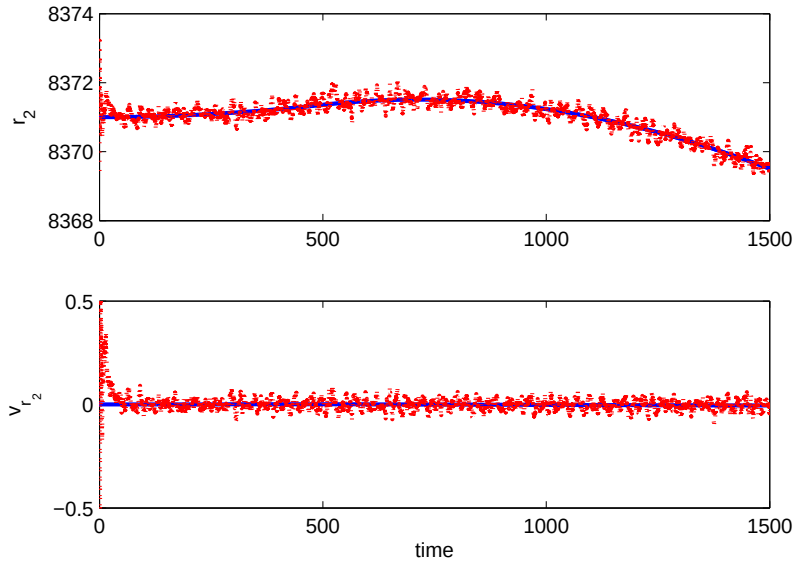

Fig. 68. Example 4: True and Estimated r_2 States.

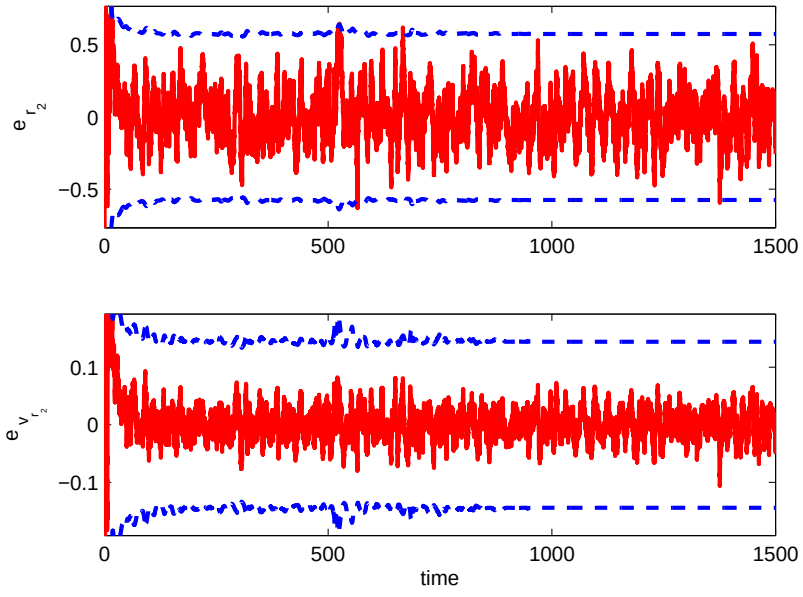

Fig. 69. Example 4: r_2 State Estimate Error with $3-\sigma$ Error Bounds.

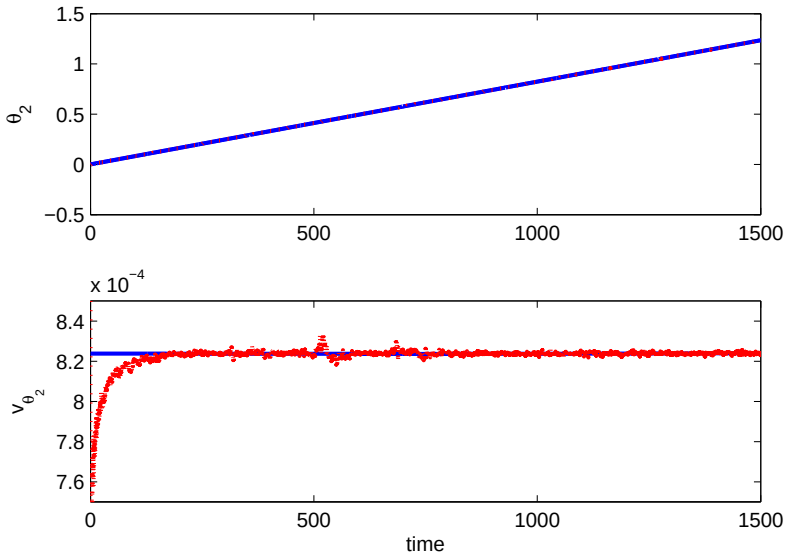

Fig. 70. Example 4: True and Estimated θ_2 States.

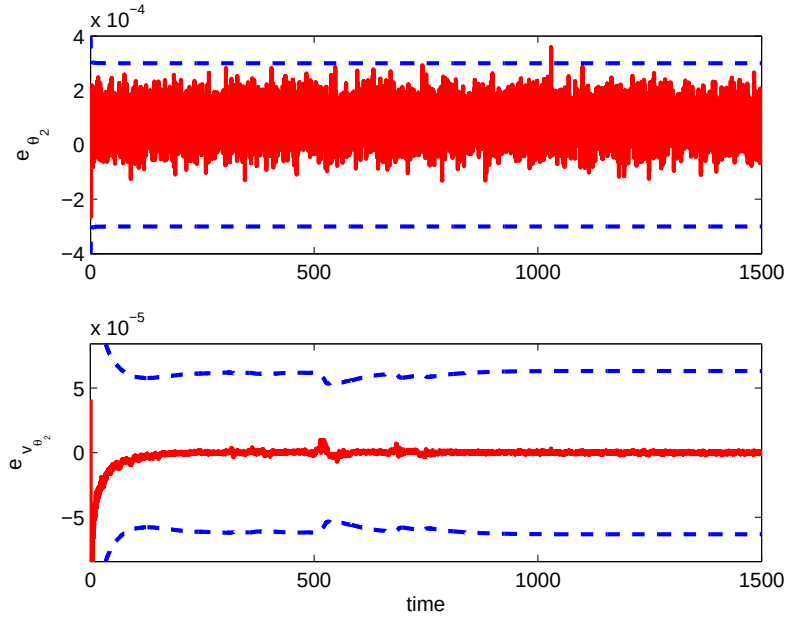

Fig. 71. Example 4: θ_2 State Estimate Error with $3-\sigma$ Error Bounds.

C. Summary

The general strategy presented in this chapter is useful for designing a constrained system that can autonomously monitor its constrained motion, detect constraint violation, and make estimation and control decisions accordingly. Each of the two strategies outlined are shown to successfully detect constraint violation with respect to an associated confidence bound and automatically select the dynamical model that better reflects the unconstrained motion. In order to detect constraint violation with some degree of certainty, a measure is needed to bound the estimate of the constraint value. Here, the measure selected is the variance associated with the constraint estimate. This measure can be approximated by linearizing the constraint about the "true" constraint value and then evaluating the partial derivative coefficients with the estimated state values. Using this linearized constraint relationship, the linear property of the expectation operator can be utilized to approximate the variance associated with the constraint. It is then up to the user to impose switching logic that accounts for the certainty of constraint violation via the constant coefficient (i.e., 1-, 2-, 3-, etc.) of the constraint σ_ϕ bound.

The plots and analysis from the numerical results show that the two methods presented can be successfully implemented in the CDEKF. These simulations also indicate that Method 1 is the more advantageous approach due to the additional complexity and sensitivity to process noise of Method 2. Through several examples, this approach is shown to work for both holonomic and nonholonomic constraints, as well as for multiple constraints. Overall, this method allows multi-model (constrained and unconstrained) estimation for systems subject to broken constraints.

CHAPTER VI

HYBRID SYSTEM ESTIMATION STRATEGY

For hybrid dynamical systems, integration with respect to both space and time are required to construct the states of the system over a specified interval of time. For some linear systems, a separation of variables approach can be employed to partition the equations into time-varying and space-varying components [7]. For simple systems, the resulting differential Eigenvalue problem can be solved: highly accurate numerical approximations for the Eigenvalues of the spatial component can be calculated and a solution (truncated series of infinite Eigenfunction terms) can be constructed. For more complex systems, this differential Eigenvalue problem is less straightforward, and a finite-dimensional approximation of the governing equations is commonly implemented (though, recently, a generalized frequency domain state-space model has been presented) [30]. Common approaches for transforming the infinite-dimensional problem to a finite-dimensional one include the assumed modes method and finite element method [7, 12].

In this chapter, the assumed modes method is investigated as a means for implementing the continuous-discrete extended Kalman filter for hybrid dynamical systems with a single spatial domain. Typically, references to the assumed modes method implies *linear* assumed modes. Here, both *linear* and *quadratic* assumed modes methods is explored. For estimation, these methods are preferred over the finite element method, which is more appropriate for complex geometries but requires a greater number of finite-dimensional coordinates to accurately approximate the system Eigenvalues [7]. The spatially-dependent terms in both the linear and quadratic assumed modes methods are computed prior to the implementation of the estimation

scheme. After applying a finite-dimensional treatment to the flexible domain, the resulting ODE form of the equations of motion are then used within the CDEKF structure.

A. Linear Assumed Modes Method

In the linear assumed modes method, the transverse deflection, $\mathbf{w}$, of an elastic body is approximated by a series of n products of space- and time- dependent functions [7, 31].

$$\mathbf{w}(x,t) = \sum_{i=1}^{n} \phi_i(x) q_i(t) = \phi_i q_i \tag{6.1}$$

The time-dependent functions, $q_i(t)$ serve as time-varying amplitudes for the space-dependent functions, $\phi(x)$, and can be considered generalized coordinates of the finite-dimensional model of the system. The space-dependent functions, called the "assumed modes," are divided into three categories of linearly independent functions: admissible functions, comparison functions, and Eigenfunctions.

Admissible functions, which are most commonly employed, satisfy the geometric boundary conditions and are differentiable at least half as many times as the order of the system. Comparison functions additionally satisfy the physical/natural boundary conditions and are differentiable as many times as the order of the system. In addition to the boundary conditions, Eigenfunctions also satisfy the governing partial differential equation for $\mathbf{w}(x,t)$. These functions and the associated Eigenvalues can be difficult to find, even for simple geometries. Once the n spatial functions are either chosen or calculated, Eq. 6.1 can be used to rewrite the kinetic and potential energies of the system as a function of the finite-dimensional generalized coordinates. After this substitution, Lagrange's equations for finite-dimensional systems (see Ch. II) can be applied to find the governing equations for the generalized coordinates $q_i(t)$.

B. Quadratic Assumed Modes Method

With linear assumed modes, no accommodation is explicitly made for the coupling between the transverse deflection, $\mathrm{w}(x,t)$, and longitudinal displacement, $\mathrm{u}(x,t)$, of a differential element [31, 32, 33]. Quadratic assumed modes accounts for displacement along the longitudinal axis arising from the transverse motion of the body. Imposing that each differential element is inextensible and assuming that the change in longitudinal displacement with respect to x is small, the following relation can be established.

$$\mathbf{u}(x,t) = -\frac{1}{2}\int_{l_0}^{x}\left(\frac{\mathrm{d}\mathbf{w}}{\mathrm{d}x}\right)^2 \mathrm{dx} = -q_i q_j \int_{l_0}^{x}\left(\phi_i'\phi_j'\right) = \Psi_{ij} q_i q_j \tag{6.2}$$

As with linear assumed modes, Eqs. 6.1 and 6.2 are applied in the kinetic and potential energies before employing Lagrange's equations for finite-dimensional generalized coordinates. Whether linear or quadratic assumed modes in applied, n equations of motion result for the approximation of the flexible body coordinate, as well as a governing equation for each of the original discrete coordinates.

C. Assumed Modes and Estimation

Unlike the integro-partial differential equations of Eqs. 2.17-2.23 in Ch. II, the finite-dimensional ordinary differential equation approximations resulting from implementation of linear or quadratic assumed modes method can be used in Eqs. 2.29 and Eq. 2.31 of the CDEKF propagation step. However, the measurement model utilized in the update/correction step must also be considered. For the flexible body components of the system, a mapping between the sensor measurements and the displacement is typically available. The m measurement locations along the undeformed longitudinal axis must first be determined. Then, using Eq. 6.1 as the model for the m deformable body measurements, the first n rows of H_k at time $t = t_k$ in Eq. 2.31

can be formed.

$$\boldsymbol{y}_k = \begin{bmatrix} \mathbf{w}(x_1, t_k) \\ \vdots \\ \mathbf{w}(x_m, t_k) \end{bmatrix} = \begin{bmatrix} \phi_1(x_1) & \dots & \phi_n(x_1) \\ \vdots & \ddots & \vdots \\ \phi_1(x_m) & \dots & \phi_n(x_m) \end{bmatrix} \begin{bmatrix} q_1(t_k) \\ \vdots \\ q_n(t_k) \end{bmatrix} = H_k \boldsymbol{q}_k \tag{6.3}$$

Measurements of $\dot{\mathbf{w}}(x_i, t_k)$, $\mathbf{w}'(x_i, t_k)$, etc. can be similarly arranged. If the number of unique measurements equals or exceeds the number of assumed modes, $m \geq n$, then an initial guess of the measurements (or an actual initial measurement) in most cases can be used to calculate an initial guess for the configuration-level states, velocity-level states, or both, using the inverse relationship.

D. Example: Rotating Hub with Flexible Appendage

Both linear and quadratic assumed modes are now applied to a planar hybrid dynamical system example, a rotating satellite, to show how each can be incorporated into the CDEKF. Consider the problem of a slewing satellite composed of a rigid hub with flexible appendage, as shown in Fig. 72. The axes $\hat{\boldsymbol{b}}_i$, $i = 1 \dots 3$ shown in the figure are body fixed with $\hat{\boldsymbol{b}}_3$ out of the page. The hub has mass m, radius R, and axial inertia J. The appendage has mass density ρ, modulus of elasticity E, second moment of inertia of the bending section I, and length L. The displacement of the flexible body is described relative to its undeformed longitudinal axis and is associated with a location, x, along this axis. Longitudinal deformation is denoted by $\mathbf{u}(x, t)$, whereas transverse deformation is described with $\mathbf{w}(x, t)$.

Using the center of the hub as the origin with $0 < x < L$, the position of a differential element along the flexible body can be written in vector form.

$$\boldsymbol{r} = (R + x)\hat{\boldsymbol{b}}_1 + \mathbf{w}\hat{\boldsymbol{b}}_2 \tag{6.4}$$

Note that, for now, longitudinal deformation is neglected. Taking the frame-independent

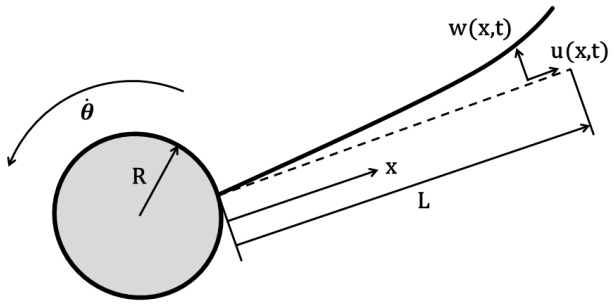

Fig. 72. Slewing Satellite Illustration.

time derivative with a hub rotation rate of $\boldsymbol{\omega} = \dot{\theta}\hat{\boldsymbol{b}}_3$, the velocity vector can be found.

$$\dot{\boldsymbol{r}} = -\mathbf{w}\dot{\theta}\hat{\boldsymbol{b}}_1 + \left((R+x)\dot{\theta} + \dot{\mathbf{w}}\right)\hat{\boldsymbol{b}}_2 \tag{6.5}$$

The kinetic energy is the sum of the rotational kinetic energy of the hub and the integral over the body of the differential element kinetic energy.

$$\begin{aligned} T &= \frac{1}{2}\boldsymbol{\omega}\cdot J\boldsymbol{\omega} + \frac{1}{2}\int_0^L \rho\left(\dot{\boldsymbol{r}}\cdot\dot{\boldsymbol{r}}\right)\mathrm{d}x \\ &= \frac{1}{2}J\dot{\theta}^2 + \frac{1}{2}\int_0^L \rho\left((R+x)^2\dot{\theta}^2 + 2(R+x)\dot{\mathbf{w}}\dot{\theta} + \dot{\mathbf{w}}^2 + \mathbf{w}^2\dot{\theta}^2\right)\mathrm{d}x \\ &= \frac{1}{2}\left(J + \int_0^L \rho(R+x)^2\mathrm{d}x\right)\dot{\theta}^2 + \frac{1}{2}\int_0^L \rho\left(2(R+x)\dot{\mathbf{w}}\dot{\theta} + \dot{\mathbf{w}}^2 + \mathbf{w}^2\dot{\theta}^2\right)\mathrm{d}x \\ &= \frac{1}{2}\hat{J}\dot{\theta}^2 + \frac{1}{2}\int_0^L \rho\left(2(R+x)\dot{\mathbf{w}}\dot{\theta} + \dot{\mathbf{w}}^2 + \mathbf{w}^2\dot{\theta}^2\right)\mathrm{d}x \end{aligned} \tag{6.6}$$

Similarly, the potential energy over the flexible body is found with the following equation.

$$V = \int_0^L EI(\mathbf{w}'')^2\mathrm{d}x \tag{6.7}$$

Applying Eqs. 2.17 and 2.18 of Lagrange's equations for hybrid dynamical systems

yields the governing equations.

$$\hat{J}\ddot{\theta} + \int_0^L \rho\left((R+x)\ddot{\mathbf{w}} + \mathbf{w}^2\ddot{\theta} + 2\mathbf{w}\dot{\mathbf{w}}\dot{\theta}\right)\mathrm{d}x = u \tag{6.8}$$

$$\rho\left(\ddot{\mathbf{w}} + (R+x)\ddot{\theta}\right) - \rho\mathbf{w}\dot{\theta}^2 + EI\mathbf{w}'''' = 0 \tag{6.9}$$

Eqs. 2.20 and 2.21 give the natural boundary conditions.

$$\mathbf{w}''(L,t) = 0 \quad ; \quad \mathbf{w}'''(L,t) = 0 \tag{6.10}$$

The geometric boundary conditions arise from the physical constraints of the system.

$$\mathbf{w}(0,t) = 0 \quad ; \quad \mathbf{w}'(0,t) = 0 \tag{6.11}$$

1. Hybrid Example: Linear Assumed Modes

The finite-dimensional equations of motion are now derived using linear assumed modes. Substituting Eq. 6.1 into the kinetic energy yields the following finite-dimensional form.

$$\begin{aligned} T &= \frac{1}{2}\hat{J}\dot{\theta}^2 + \frac{1}{2}\int_0^L \rho\phi_i\dot{q}_i\phi_j\dot{q}_j\mathrm{d}x + \frac{1}{2}\int_0^L \rho\phi_i q_i\phi_j q_j\dot{\theta}^2\mathrm{d}x + \int_0^L \rho(R+x)\phi_i\dot{q}_i\dot{\theta}\mathrm{d}x \\ &= \frac{1}{2}\hat{J}\dot{\theta}^2 + \frac{1}{2}M_{ij}\dot{q}_i\dot{q}_j + \frac{1}{2}M_{ij}q_iq_j\dot{\theta}^2 + N_i\dot{q}_i\dot{\theta} \end{aligned} \tag{6.12}$$

Here, the following time-independent matrices can be constructed using the assumed modes.

$$M_{ij} = \int_0^L \rho\phi_i\phi_j\mathrm{d}x \quad ; \quad N_i = \int_0^L \rho(R+x)\phi_i\mathrm{d}x \tag{6.13}$$

Similarly, the potential energy can be written in a finite-dimensional form.

$$V = q_iq_j\int_0^L EI\phi_i''\phi_j''\mathrm{d}x = K_{ij}q_iq_j \tag{6.14}$$

The stiffness matrix can also be independently constructed using the assumed modes.

$$K_{ij} = \int_0^L EI\phi_i''\phi_j'' \mathrm{d}x \tag{6.15}$$

The equations of motion for q_i that result from applying Lagrange's equations for finite-dimensional systems, Eq. 2.4, typically have a form linear in the generalized coordinates and accelerations, but not in the generalized velocities.

$$M\ddot{\boldsymbol{q}} + K\boldsymbol{q} + \ldots = 0 \tag{6.16}$$

A damping term is not present in this model, so proportional damping is often appended to the dynamics to better reflect observations of physical system behavior.

$$C = \alpha M + \beta K \quad ; \quad \alpha > 0,\, \beta > 0 \tag{6.17}$$

Similarly, a damping coefficient can be employed for the equation governing the rotation of the hub. Once Lagrange's equations and proportional damping are applied, the following equations result.

$$(\hat{J} + \boldsymbol{q}^T M \boldsymbol{q})\ddot{\theta} + N^T\ddot{\boldsymbol{q}} + C_\theta\dot{\theta} + 2\boldsymbol{q}^T M\dot{\boldsymbol{q}}\dot{\theta} = u \tag{6.18}$$

$$M\ddot{\boldsymbol{q}} + N\ddot{\theta} + C\dot{\boldsymbol{q}} + (K - M\dot{\theta}^2)\boldsymbol{q} = 0 \tag{6.19}$$

Here, note that the equation of motions for the approximations to the flexible body dynamics exhibit "softening" in the stiffness matrix, $(K - M\dot{\theta}^2)$, as the angular velocity of the hub increases. The method of *quadratic* assumed modes is motivated by the contradiction of this behavior to that observed in physical systems [32].

State time histories are numerically simulated for $\boldsymbol{x}(t) = [q_i,\, \dot{q}_i,\, \theta,\, \dot{\theta}]$ using a Runge-Kutta routine (MATLAB function *ode45*) for the unforced governing equations

given above with the following admissible functions as the assumed modes.

$$\phi_i(x) = \left(\frac{x}{L}\right)^{i+1} \tag{6.20}$$

The system parameters are shown in Table II, and the initial values for the discrete states are $\theta = 0$ rad and $\dot{\theta} = .3$ rad/s.

Table II. Slewing Satellite Parameter Values.

Parameter	Value
L	45.52 in
E	$161.6e10^(6)$ oz/in^2
I	0.000813 in^4
ρ	0.003007 oz-s^2/in
R	5.5470 in
m	31.59 oz
α	0.25
β	0.0025
C_θ	1000
n_{modes}	5

Gaussian noise ($\sigma_{w_j} = 0.5$, $\sigma_\theta = 0.01$) is added to $m = 5$ simulated "true" measurements constructed with Eq. 6.1 and the simulated states. The measurement locations are chosen to be equidistant along the undeformed longitudinal axis such that $\triangle x = L/m$ and $x_j = j \triangle x$, $j = 1 \ldots m$. The initial state covariance matrix is $P_0 = 500I$, where I is the identity matrix. The following measurement noise

covariance and process noise covariance matrices are used.

$$R_k = \begin{bmatrix} \sigma_{w_1}^2 & 0 & \dots & 0 \\ 0 & \ddots & & \vdots \\ \vdots & & \sigma_{w_m}^2 & 0 \\ 0 & \dots & 0 & \sigma_\theta^2 \end{bmatrix} \tag{6.21}$$

$$Q(t) = \begin{bmatrix} .001 & 0 & \dots & & 0 \\ 0 & .001 & & & \vdots \\ \vdots & & 10^{-4} & & \\ & & & \ddots & 0 \\ 0 & \dots & & 0 & 10^{-4} \end{bmatrix} \tag{6.22}$$

The simulation results employ these "actual" measurements with Eqs. 6.3, 6.18, and 6.19 in the structure of the CDEKF presented in Ch. II. Note that the coordinate dependence in the effective inertia coefficient of $\ddot{\theta}$ in Eq. 6.18 is neglected to prevent poor conditioning of the matrix F. The initial state guesses are the true initial states with approximately 20% error. Figures 73-74 show the actual measurements with "reconstructed" measurements calculated using Eq. 6.3 and the state estimates. Figures 75-86 compare the "true" states with the state estimates and show the associated error between them. In the plots of this chapter, red lines indicate the reconstructed measurements, estimates, or estimate errors and the blue lines indicate the actual measurements, true measurements, or $3-\sigma$ bounds (respectively). These results show that the CDEKF performs as expected with measurements constructed and states estimated using the linear assumed modes method. After performing a similar verification with quadratic assumed modes, both methods are compared using measurements constructed from a third source.

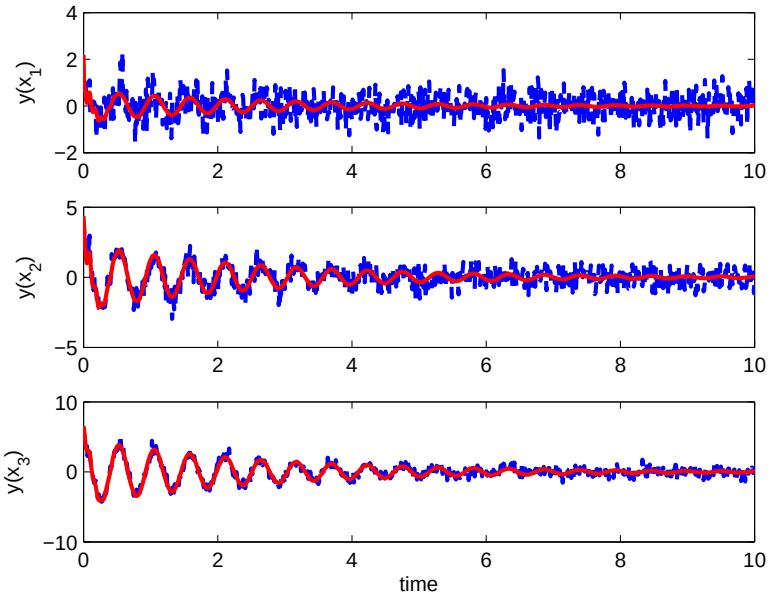

Fig. 73. Actual and Reconstructed Measurements Using Linear Assumed Modes: $y(x_1) - y(x_3)$.

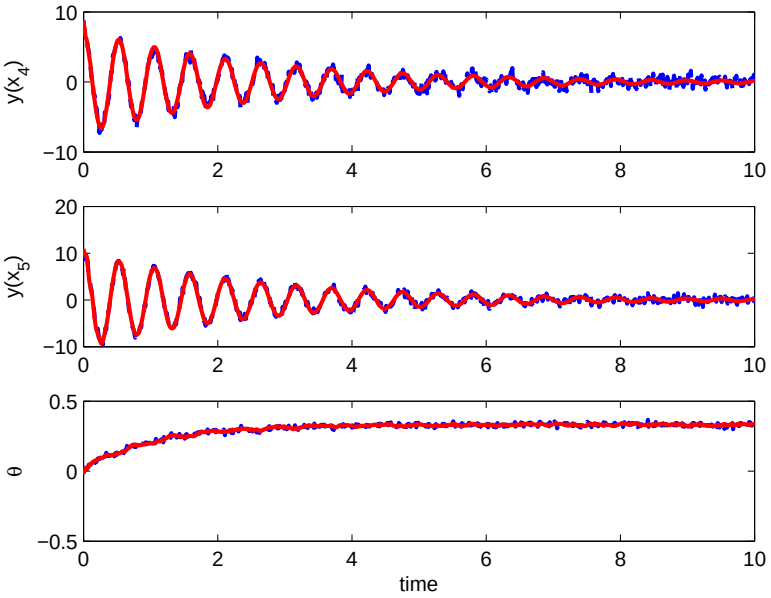

Fig. 74. Actual and Reconstructed Measurements Using Linear Assumed Modes: $y(x_4) - y(x_5)$ and θ.

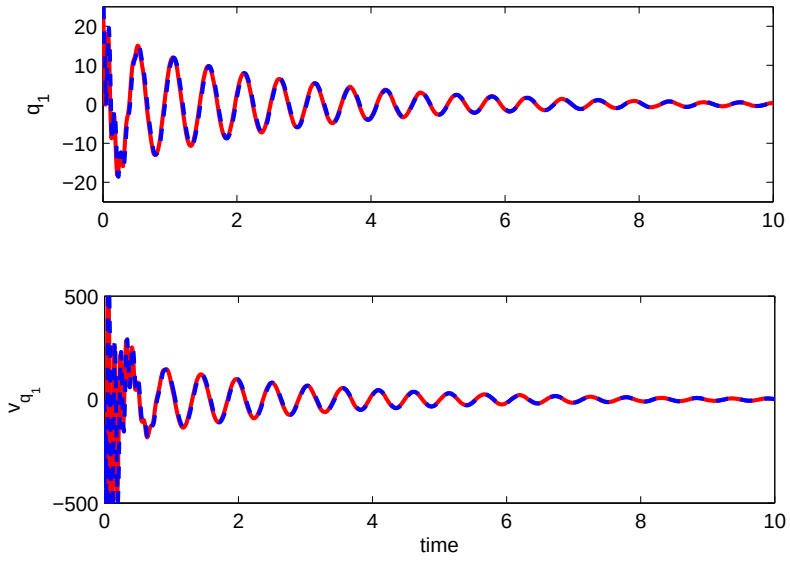

Fig. 75. Actual and Estimated Modal Amplitudes Using Linear Assumed Modes: q_1 and $\dot{q}_1$.

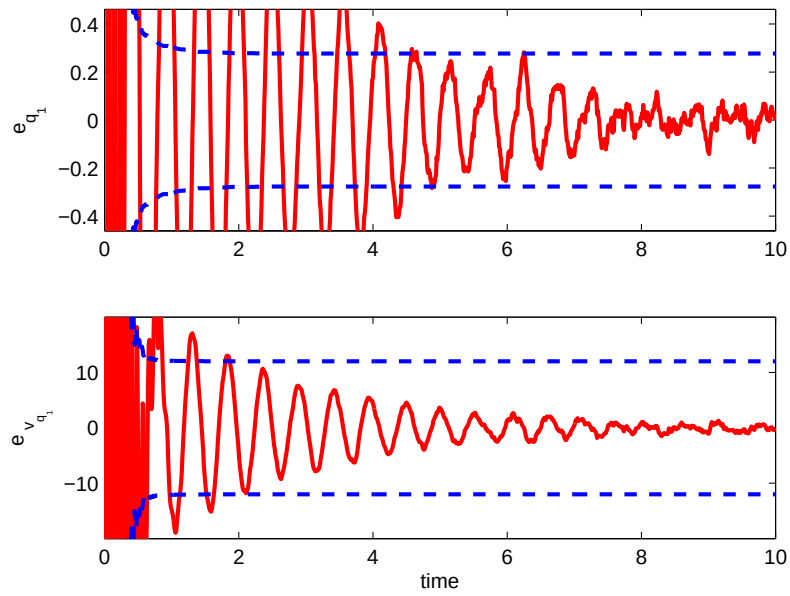

Fig. 76. Error in Estimated Modal Amplitudes Using Linear Assumed Modes: q_1 and $\dot{q}_1$.

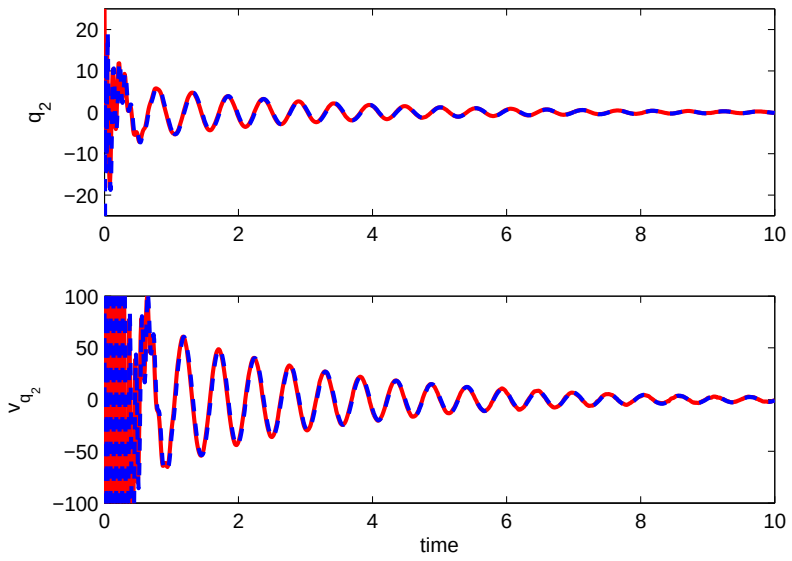

Fig. 77. Actual and Estimated Modal Amplitudes Using Linear Assumed Modes: q_2 and $\dot{q}_2$.

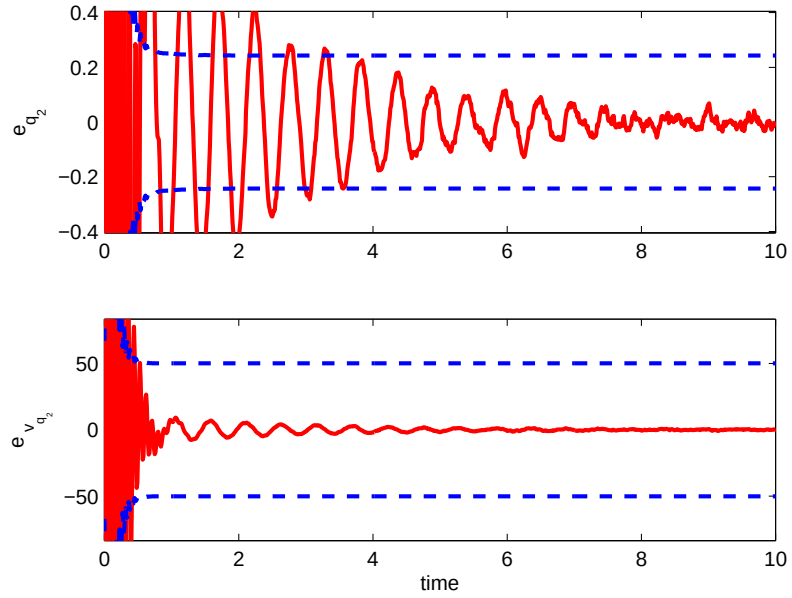

Fig. 78. Error in Estimated Modal Amplitudes Using Linear Assumed Modes: q_2 and $\dot{q}_2$.

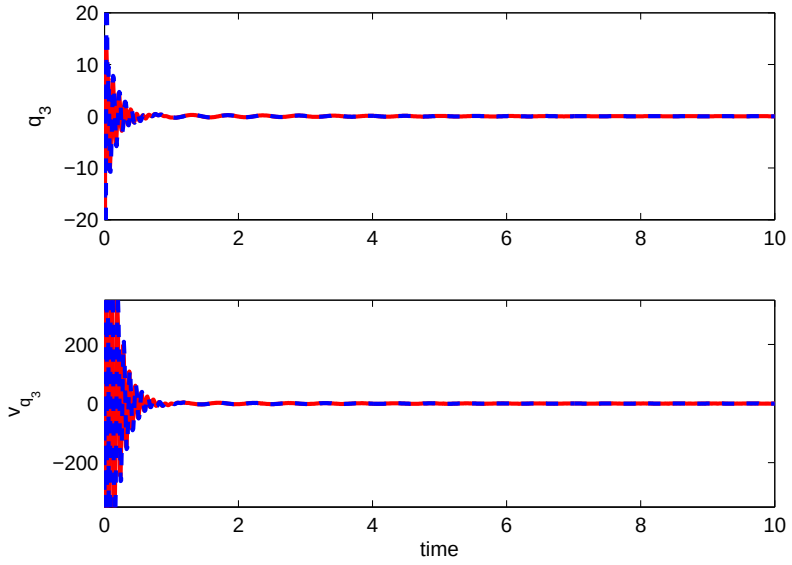

Fig. 79. Actual and Estimated Modal Amplitudes Using Linear Assumed Modes: q_3 and $\dot{q}_3$.

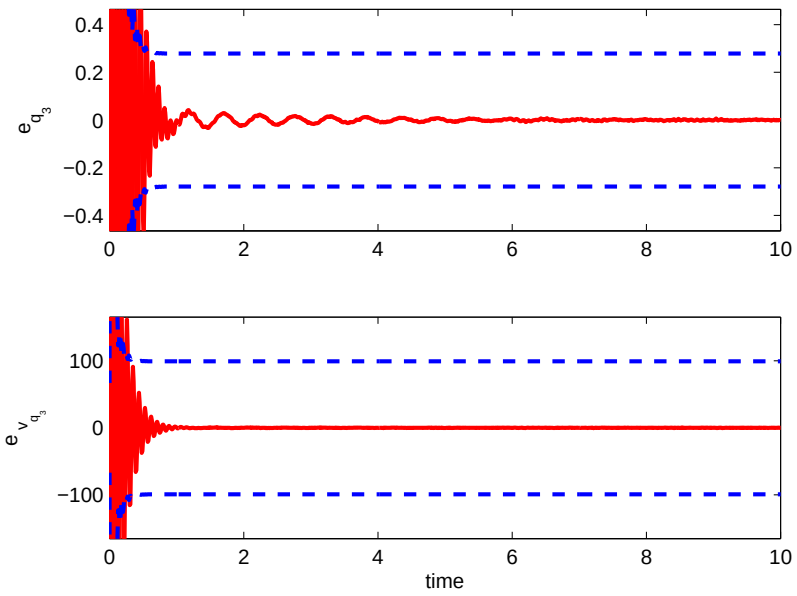

Fig. 80. Error in Estimated Modal Amplitudes Using Linear Assumed Modes: q_3 and $\dot{q}_3$.

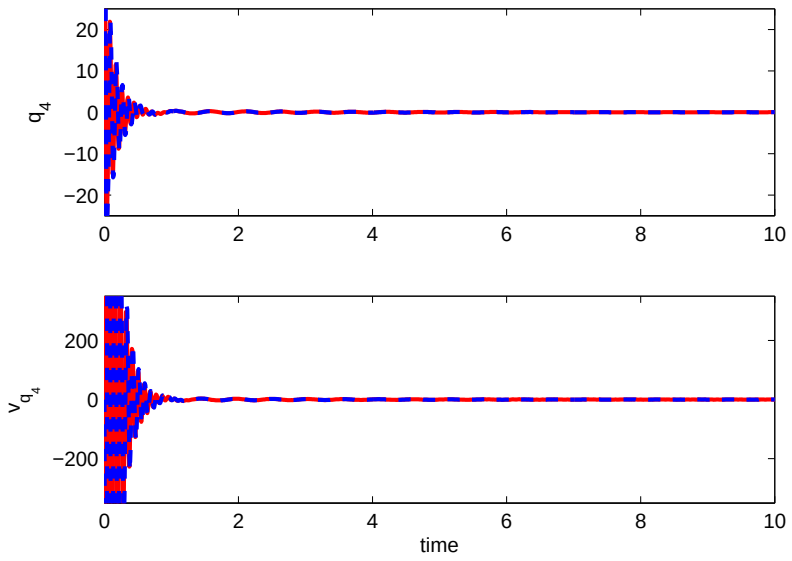

Fig. 81. Actual and Estimated Modal Amplitudes Using Linear Assumed Modes: q_4 and $\dot{q}_4$.

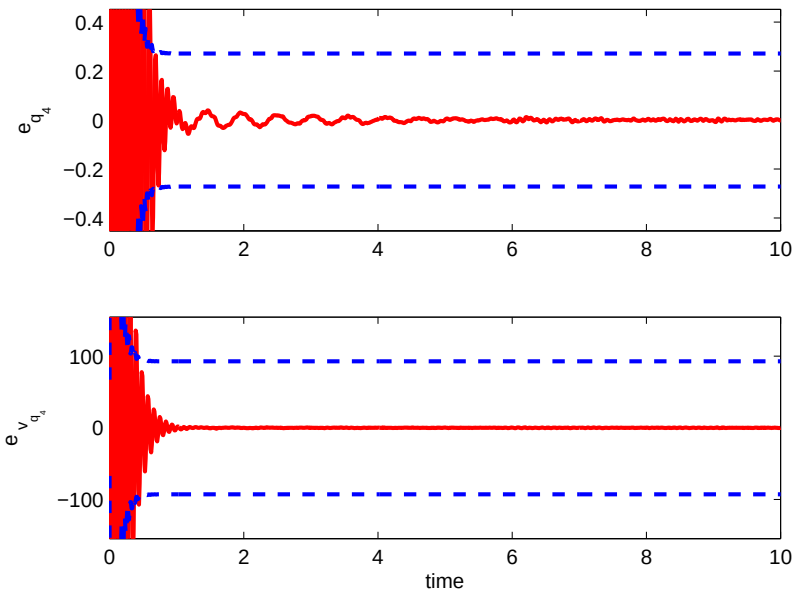

Fig. 82. Error in Estimated Modal Amplitudes Using Linear Assumed Modes: q_4 and $\dot{q}_4$.

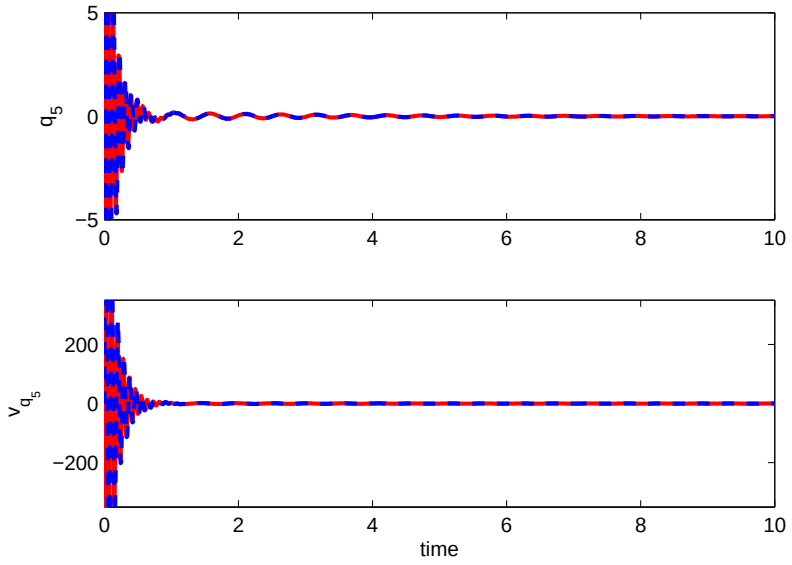

Fig. 83. Actual and Estimated Modal Amplitudes Using Linear Assumed Modes: q_5 and $\dot{q}_5$.

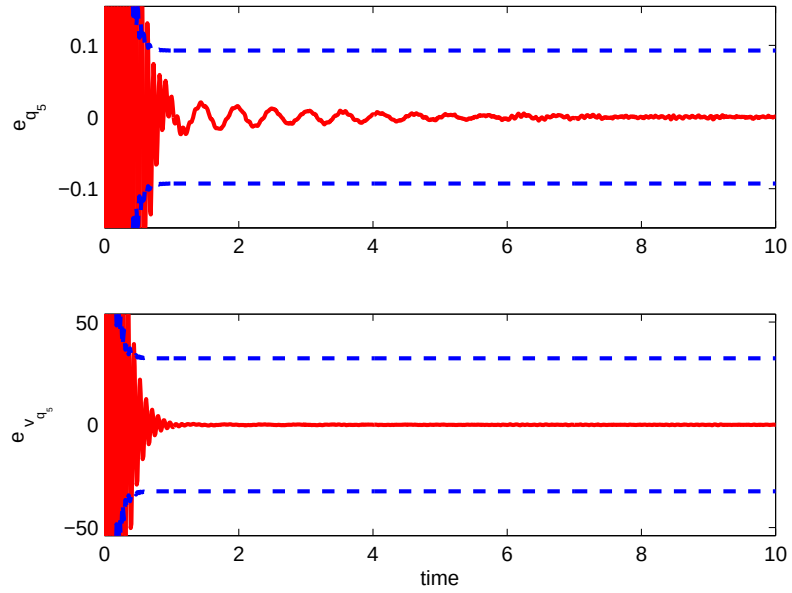

Fig. 84. Error in Estimated Modal Amplitudes Using Linear Assumed Modes: q_5 and $\dot{q}_5$.

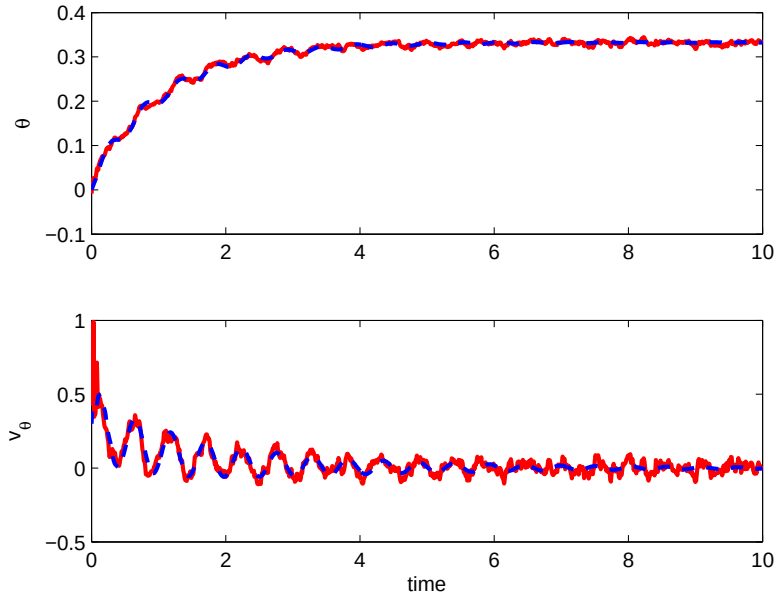

Fig. 85. Actual and Estimated Modal Amplitudes Using Linear Assumed Modes: θ and $\dot{\theta}$.

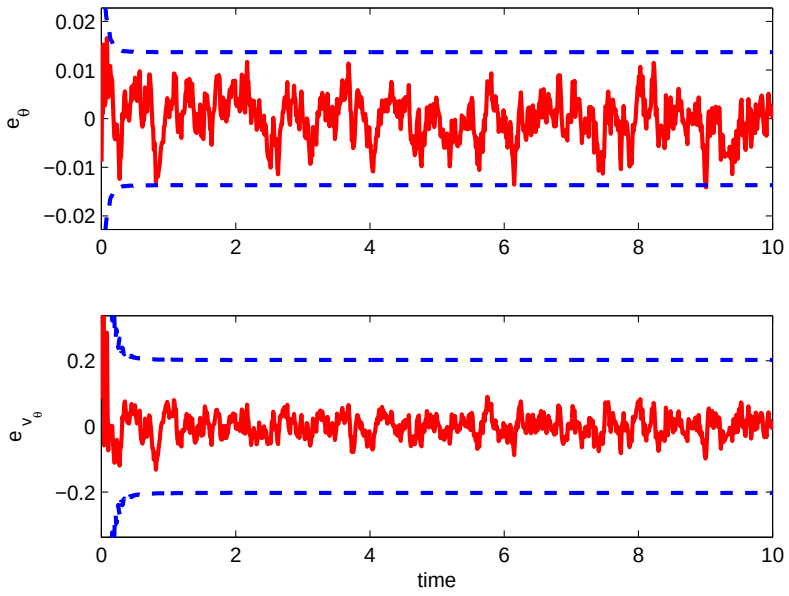

Fig. 86. Error in Estimated Modal Amplitudes Using Linear Assumed Modes: θ and $\dot{\theta}$.

2. Hybrid Example: Quadratic Assumed Modes

Quadratic assumed modes is now examined for this problem. This method accounts for higher-order kinematics, which are included at both the position- and velocity-level kinematics.

$$\boldsymbol{r} = (R + x + \mathbf{u})\hat{\boldsymbol{b}}_1 + \mathbf{w}\hat{\boldsymbol{b}}_2$$

$$\dot{\boldsymbol{r}} = \left(\dot{\mathbf{u}} - \mathbf{w}\dot{\theta}\right)\hat{\boldsymbol{b}}_1 + \left((R + x + \mathbf{u})\dot{\theta} + \dot{\mathbf{w}}\right)\hat{\boldsymbol{b}}_2 \tag{6.23}$$

Utilizing Eqs. 6.1 and 6.2, forming the kinetic and potential energies, neglecting higher order energy terms (those which result in nonlinearities in the governing equations), and adding proportional damping yields the following equations.

$$(\hat{J} + \boldsymbol{q}^T(M + 2\bar{M})\boldsymbol{q})\ddot{\theta} + N^T\ddot{\boldsymbol{q}} + C_\theta\dot{\theta} + 2\boldsymbol{q}^T(M + 2\bar{M})\dot{\boldsymbol{q}}\dot{\theta} = u \tag{6.24}$$

$$M\ddot{\boldsymbol{q}} + N\ddot{\theta} + C\dot{\boldsymbol{q}} + (K - (M + 2\bar{M})\dot{\theta}^2)\boldsymbol{q} = 0 \tag{6.25}$$

Here, the matrix $\bar{M}_{ij}$ accounts for some higher-order nonlinearities.

$$\bar{M}_{ij} = \int_0^L \rho(R + x)\Psi_{ij}\mathrm{d}x \tag{6.26}$$

The quantity $(M+2\bar{M})$ can be shown to always be negative definite, and the resulting effective stiffness matrix, $(K-(M+2\bar{M})\dot{\theta}^2)$, reflects the expected stiffening behavior of rotating flexible bodies [32].

The simulation results in Figs. 87-100 show that the CDEKF accurately estimates the states using quadratic assumed modes. These results use the same parameters as in the linear assumed modes simulations. Both methods are effective for measurements derived from associated finite-dimensional approximations, and now each is applied to new measurements constructed from a third, higher-fidelity finite-dimensional approximation.

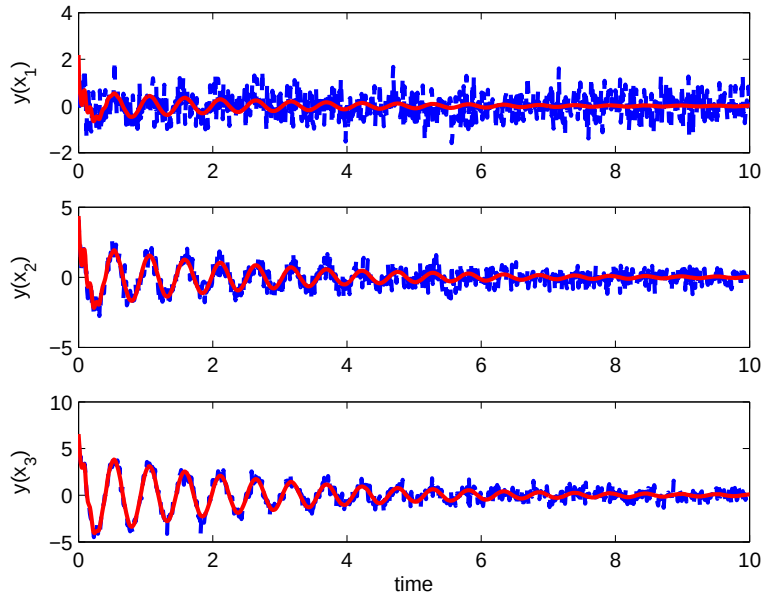

Fig. 87. Measured and Reconstructed Measurements Using Quadratic Assumed Modes: $y(x_1) - y(x_3)$.

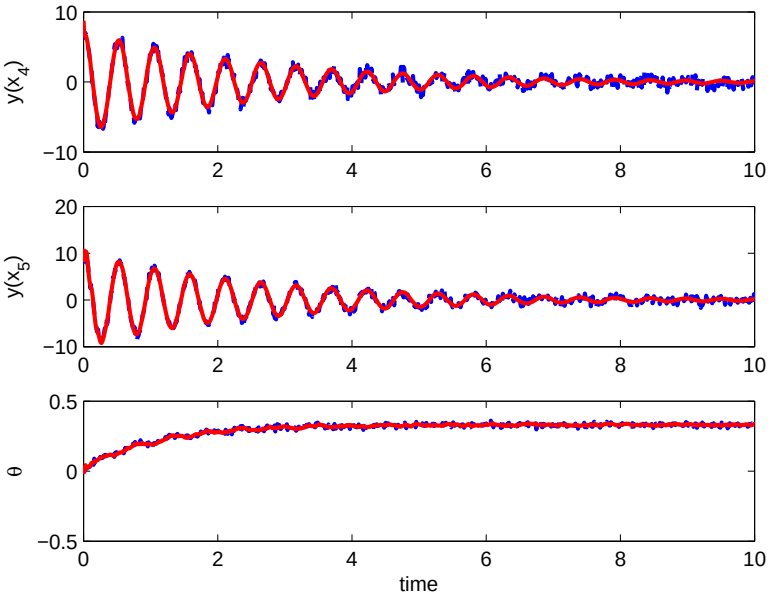

Fig. 88. Measured and Reconstructed Measurements Using Quadratic Assumed Modes: $y(x_4) - y(x_5)$ and θ.

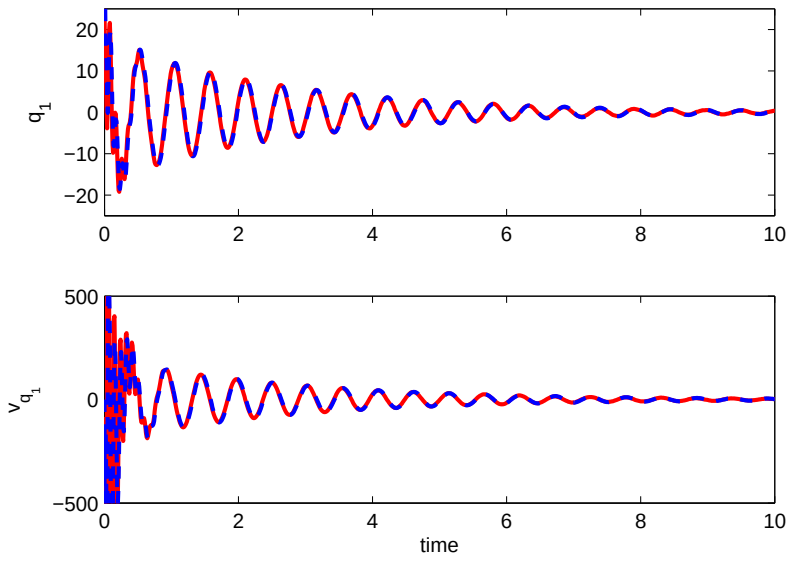

Fig. 89. Actual and Estimated Modal Amplitudes Using Quadratic Assumed Modes: q_1 and $\dot{q}_1$.

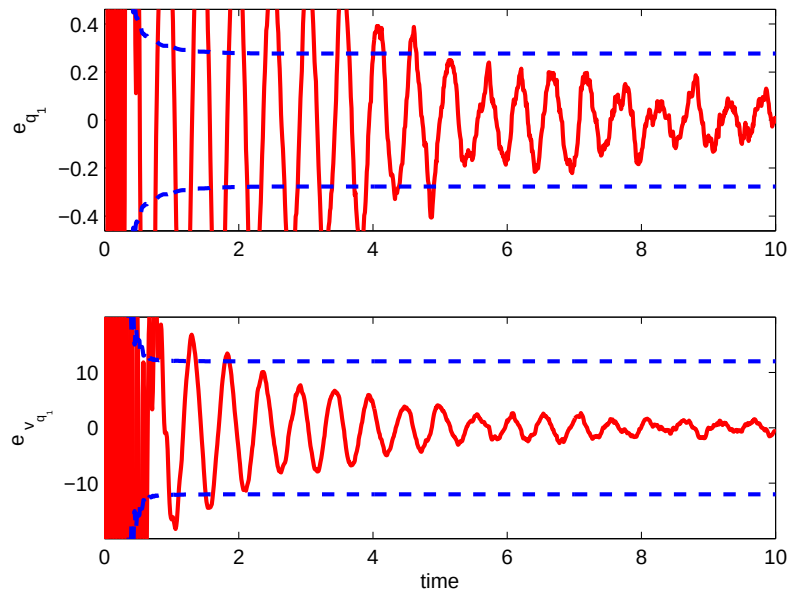

Fig. 90. Error in Estimated Modal Amplitudes Using Quadratic Assumed Modes: q_1 and $\dot{q}_1$.

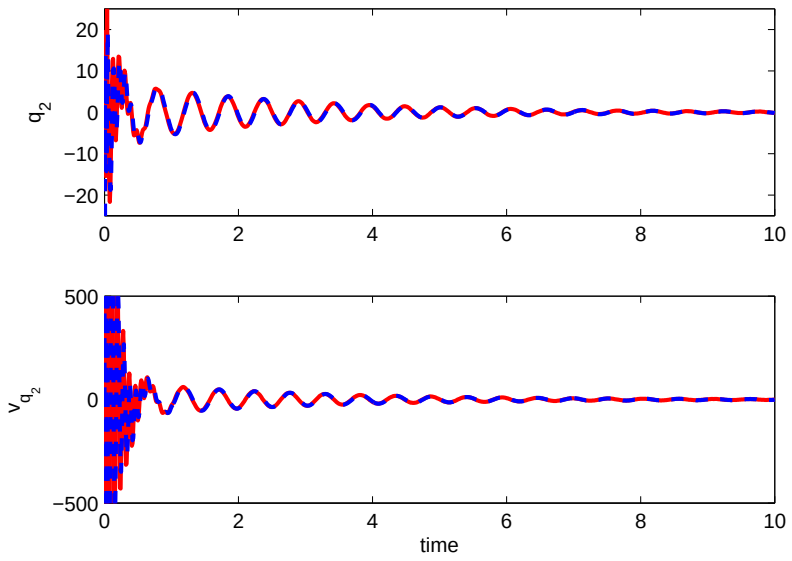

Fig. 91. Actual and Estimated Modal Amplitudes Using Quadratic Assumed Modes: q_2 and $\dot{q}_2$.

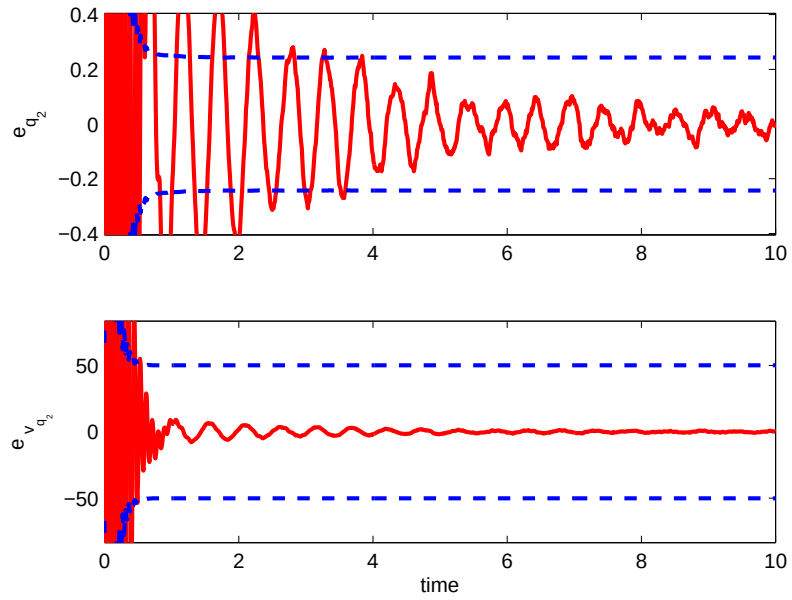

Fig. 92. Error in Estimated Modal Amplitudes Using Quadratic Assumed Modes: q_2 and $\dot{q}_2$.

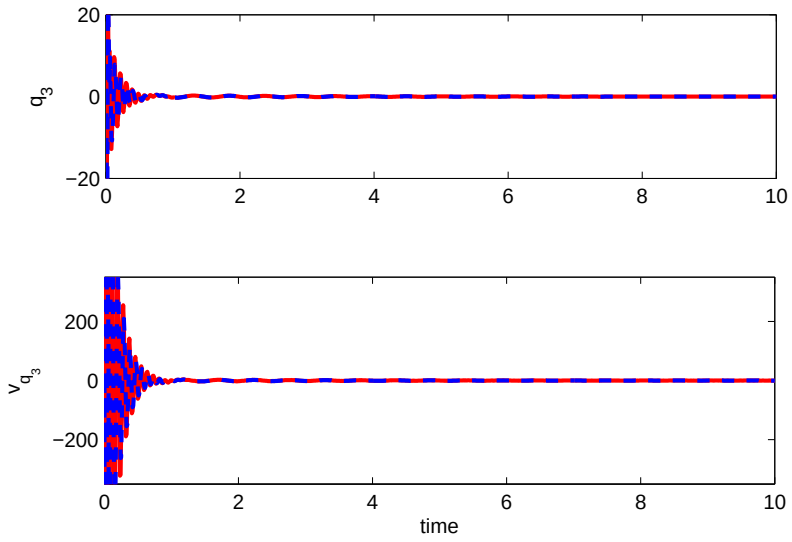

Fig. 93. Actual and Estimated Modal Amplitudes Using Quadratic Assumed Modes: q_3 and $\dot{q}_3$.

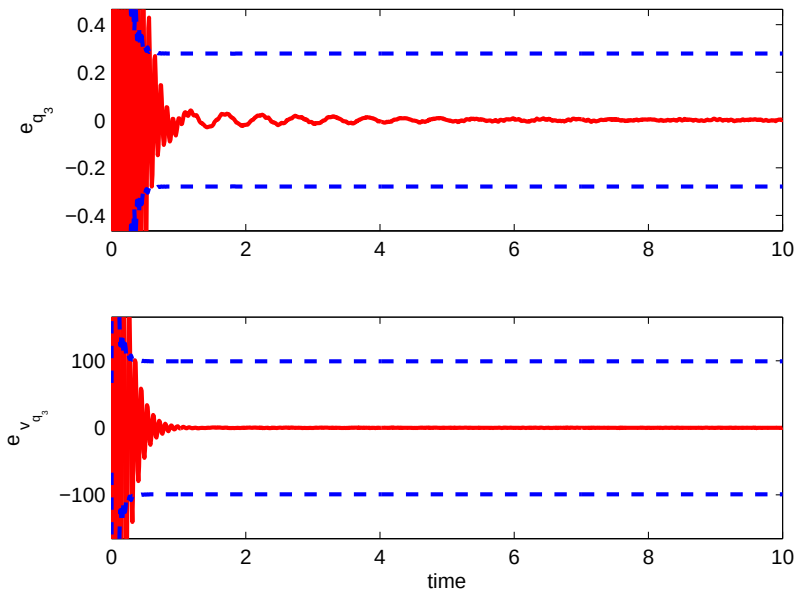

Fig. 94. Error in Estimated Modal Amplitudes Using Quadratic Assumed Modes: q_3 and $\dot{q}_3$.

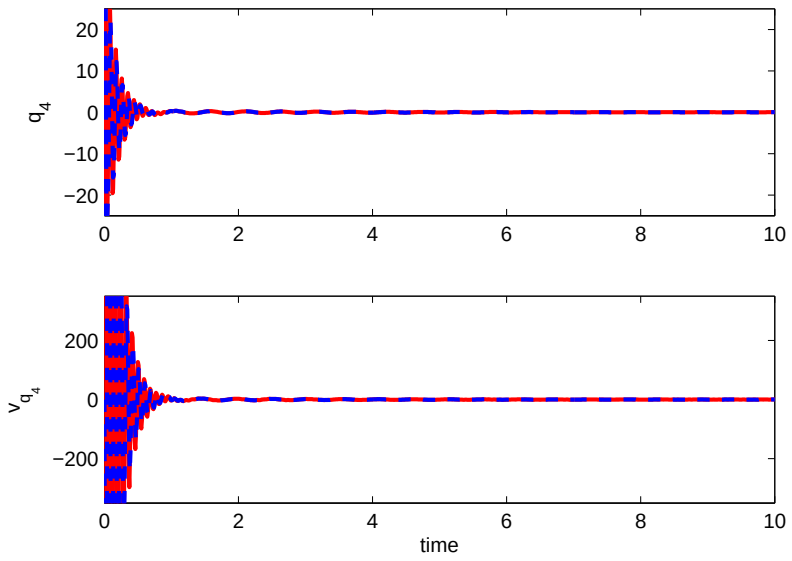

Fig. 95. Actual and Estimated Modal Amplitudes Using Quadratic Assumed Modes: q_4 and $\dot{q}_4$.

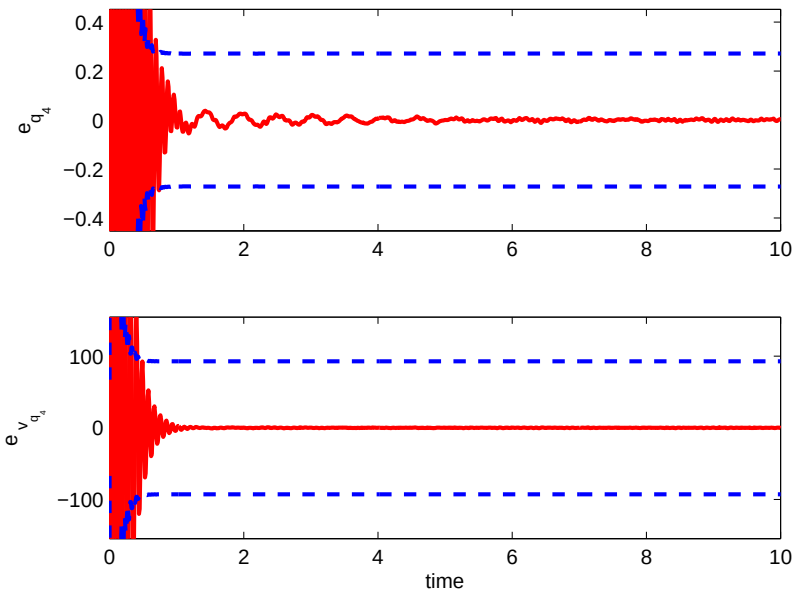

Fig. 96. Error in Estimated Modal Amplitudes Using Quadratic Assumed Modes: q_4 and $\dot{q}_4$.

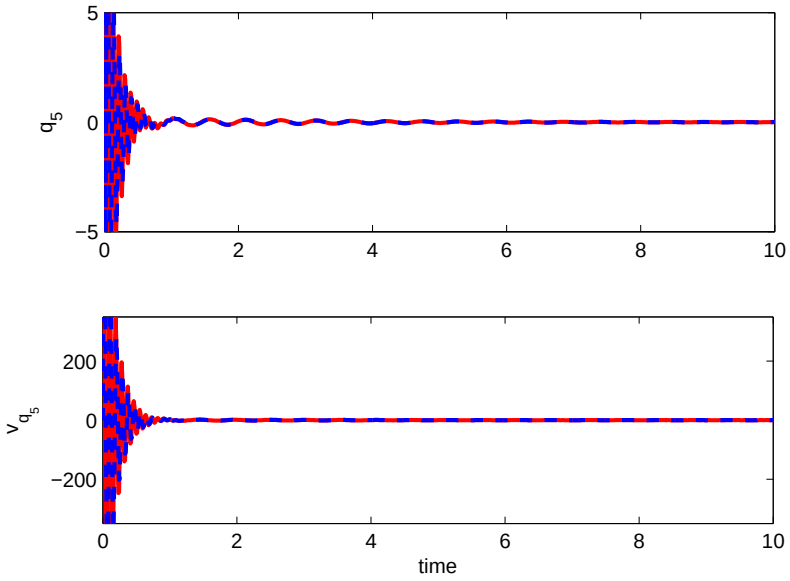

Fig. 97. Actual and Estimated Modal Amplitudes Using Quadratic Assumed Modes: q_5 and $\dot{q}_5$.

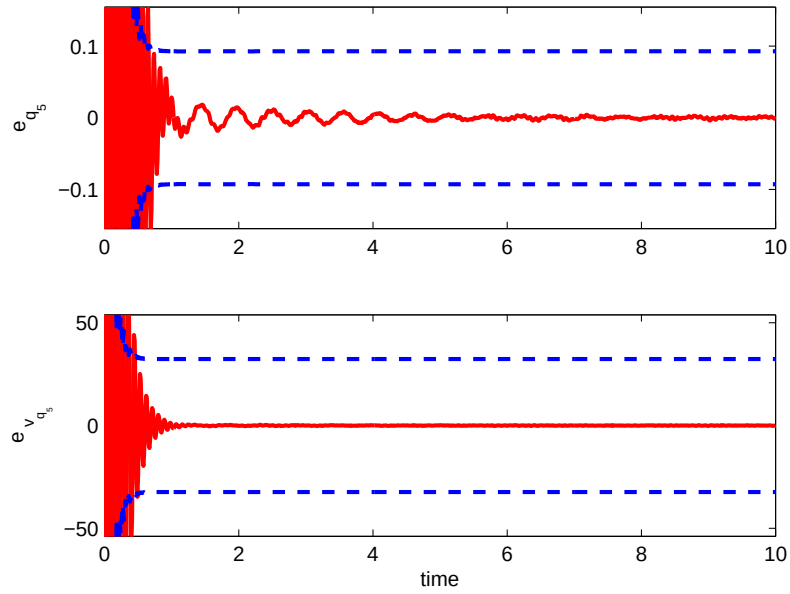

Fig. 98. Error in Estimated Modal Amplitudes Using Quadratic Assumed Modes: q_5 and $\dot{q}_5$.

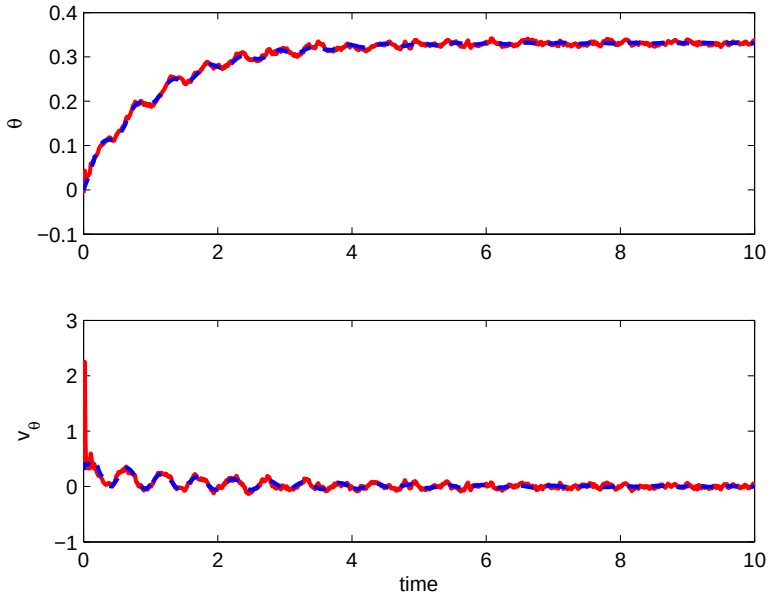

Fig. 99. Actual and Estimated Modal Amplitudes Using Quadratic Assumed Modes: θ and $\dot{\theta}$.

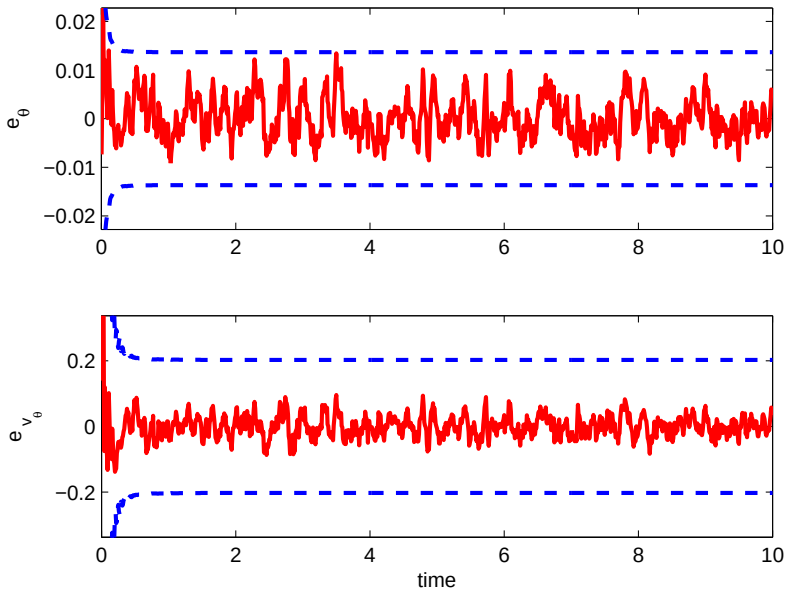

Fig. 100. Error in Estimated Modal Amplitudes Using Quadratic Assumed Modes: θ and $\dot{\theta}$.

3. Hybrid Example: Constant Angular Velocity

In order to simulate higher-fidelity finite-dimensional measurements of the infinite-dimensional motion, the example complexity is reduced. Now consider the problem of the slewing satellite rotating at a prescribed angular velocity, $\dot{\theta}$. Here, it is a assumed that there exists a control input u such that $\ddot{\theta} = 0$. For this case, the IPDEs of Eqs. 6.8 and 6.9 reduce to the following pair of PDE and ODE equations.

$$\rho\ddot{\mathbf{w}} - \rho\mathbf{w}\dot{\theta}^2 + EI\mathbf{w}'''' = 0 \tag{6.27}$$

$$\ddot{\theta} = 0 \tag{6.28}$$

The boundary conditions from Eqs. 6.10 and 6.11 still apply. Here, Eq. 6.27 is a homogeneous linear partial differential equation that admits application of the separation of variables method. In this approach, the assumed solution to the PDE consists of an infinite sum of terms that are each the product of a space-varying function, $\phi_i(x)$ and a time-varying function, $q_i(t)$. Though this sum is similar to that of the assumed modes methods, the substitution is made into the governing PDE rather than at the kinematic level. Once this substitution is made, the resulting equation can be partitioned into terms that are functions of space only and time only.

$$\rho\phi\ddot{q} = (\rho\phi\dot{\theta}^2 - EI\phi'''')q \tag{6.29}$$

$$\frac{\ddot{q}}{q} = \frac{\rho\phi\dot{\theta}^2 - EI\phi''''}{\rho\phi} = -\omega^2 \tag{6.30}$$

In this equation, the left-hand side is a function of time only, whereas the right-hand side is a function of space only. For the two equations to be equal for any location x and time t, each side of the equation must be equal to a constant, $-\omega^2$. The solution

of the time-varying equation, $\ddot{q} + \omega^2 q = 0$, is well-known.

$$q(t) = A\sin(\omega t) + B\cos(\omega t) \tag{6.31}$$

The coefficients A and B can be calculated using the initial conditions. The solution to the space-varying ODE is less well known, but the equation can be rearranged into a more familiar form.

$$EI\phi'''' - \rho\dot{\theta}^2 - \rho\omega^2\phi = 0 \tag{6.32}$$

$$\phi'''' - \frac{\rho}{EI}(\dot{\theta}^2 + \omega^2)\phi = \phi'''' - \beta^4\phi = 0 \tag{6.33}$$

The final, simplified form of this equation, coupled with the associated boundary conditions, is also the form of the classic differential Eigenvalue problem for the transverse deflection of a cantilevered beam. This problem has the following general solution.

$$\phi_i(x) = C_1\sin(\beta_i x) + C_2\cos(\beta_i x) + C_3\sinh(\beta_i x) + C_4\cosh(\beta_i x) \tag{6.34}$$

The Eigenvalues, β_i, of this problem can be found in the literature or by applying the boundary conditions to Eq. 6.34, finding the transcendental equation associated with the nontrivial solution for the coefficients C_i, and solving for the roots of this equation [7]. Here, the pseudo-spectral method using Tchebychev polynomials is employed to find the Eigenvalues (see Appendix A). Note that spectral and pseudo-spectral methods are commonly used to solve differential Eigenvalue problems in fluid mechanics, but have recently been applied to distributed parameter systems in structural dynamics using Tchebychev polynomials and radial basis functions [34, 35]. Here, the first five Eigenvalues are retained, as shown in Table III.

These Eigenvalues are combined with the boundary conditions and the general solution of the space-varying ODE (Eq. 6.34) to form a truncated series solution to

Table III. Hybrid Example Eigenvalues.

Eigenvalue Number	Numerical Value
$\beta_1 L$	1.875
$\beta_2 L$	4.694
$\beta_3 L$	7.855
$\beta_4 L$	11.000
$\beta_5 L$	14.137

the differential Eigenvalue problem. For this problem, each Eigenfunction term in the series has the following form with arbitrary amplitude C.

$$\phi_i(x) = C\Big[\cosh(\beta_i x) - \cos(\beta_i x) - \frac{\cosh(\beta_i L) + \cos(\beta_i L)}{\sinh(\beta_i L) + \sin(\beta_i L)}\left(\sinh(\beta_i x) - \sin(\beta_i x)\right)\Big] \tag{6.35}$$

Each of the Eigenvalues of the spatial ODE can then be related to the frequencies of the time-varying amplitudes with the following relation.

$$\omega_i^2 = \frac{EI}{\rho}\beta_i^4 - \dot{\theta}^2 \tag{6.36}$$

These frequency values can be employed in Eq. 6.31. For each of the retained Eigenvalues, the Eigenfunction of Eq. 6.35 can be multiplied by the time-varying amplitude of Eq. 6.31. The individual solutions can then be summed to approximate the original PDE of Eq. 6.27. Note that it is clear from Eq. 6.36 that the system is not stable for sufficiently large angular velocities. This behavior reflects the choice to neglect higher-order nonlinearities in the kinematics.

The performance of the CDEKF with each of the two finite-dimensional models is now investigated for this constant $\dot{\theta}$ case. First, all system parameters are nondi-

mensionalized and normalized: $L = E = I = \rho = R = m = 1$. Using the separation of variables method outlined above, the truncated Eigenfunction solution can be used to construct true measurements.

$$y_k(i) = \mathbf{w}(x_i, t_k) = \phi_j(x_i) q_j(t_k), \quad j = 1 \ldots 5 \tag{6.37}$$

For these simulations, measurements are taken at 10 locations along the flexible body, in addition to measurements of the angle θ. The initial state estimates are found as before, with $\theta(t_0) = 1$ rad. Measurement noise ($\sigma = .1$) is added to all of the measurements and is used to construct R_k as before. The process noise covariance matrix is $Q(t) = .1I$, where I is the identity matrix and the diagonal element related to θ is defined $Q_{\theta\theta}(t) = .01$. To reflect the assertion that there exists a control u such that $\dot{\theta}$ is constant, Eqs. 6.18 and 6.24 are reduced to $\ddot{\theta} = 0$ in the propagation step of the CDEKF. Note that, with the exception of the state estimate propagation equation (Eq. 2.29) and state matrix F (Eq. 2.31) in the state covariance matrix propagation equation, the parameters, measurements, and structure of the CDEKF algorithms are the same for both the linear and quadratic assumed modes methods.

Unlike the previous results for the hybrid example, the error for the states associated with the flexible body are not provided. Because the measurements are simulated using the Eigenfunctions and the assumed modes method is implemented with admissible functions, the $q_i(t)$ are defined differently and subsequently have values that are inherently disparate. Rather, measurements that are "reconstructed" from the admissible functions and the estimated time-varying amplitudes are compared to the actual measurements constructed using the Eigenfunctions, which are (nearly) exact solutions to the PDE. This comparison provides a means for analyzing "how well" the combination of space- and time-varying functions chosen in the linear and quadratic assumed methods model the infinite-dimensional coordinate dynamics.

Two cases are considered. First, the angular velocity is prescribed such that the system is stable: $\dot{\theta} = .4$ rad/s. The simulation results for this case are shown in Figs. 101-124. These plots show that the quadratic assumed modes model appears to more quickly converge to the true measurements. Analysis of the errors for each method also shows that the measurements reconstructed from the linear assumed modes estimates have 3-4% greater error over the simulation time period than those calculated with the states from the quadratic assumed modes method. These results indicate that the accommodation of higher-order effects may allow the quadratic assumed modes model to more quickly filter the "real" PDE measurements.

The angular velocity of the second case is chosen to drive the system unstable: $\dot{\theta} = 4$. For this case, see Figs. 125-140. The unstable behavior of the system is clear in the figures: the transverse deflection grows much greater than 1, the length of the flexible appendage itself. Both approximations fail to filter the measurements after a short period of time. The error in the quadratic assumed modes model gradually increases with time, but provides an estimate nonetheless. On the other hand, the linear assumed modes model seems to converge to the true measurements for a considerably longer amount of time, but then fails altogether and provides no estimates at all. The initial convergence of the linear assumed modes method is likely because both the continuous model (Eq. 6.9) and linear assumed modes model (Eq. 6.19) share the characteristic that the stiffness matrix softens as $\dot{\theta}$ increases.

The measurements of Case 1 more closely resemble the behavior observed in physical, real-world hybrid dynamical systems. The simulation results indicate a stronger correlation of increased CDEKF performance of quadratic assumed modes, particularly with Case 1. This relationship supports the supposition that quadratic assumed modes may typically provide a better finite-dimensional approximation for use in estimation of hybrid dynamical systems.

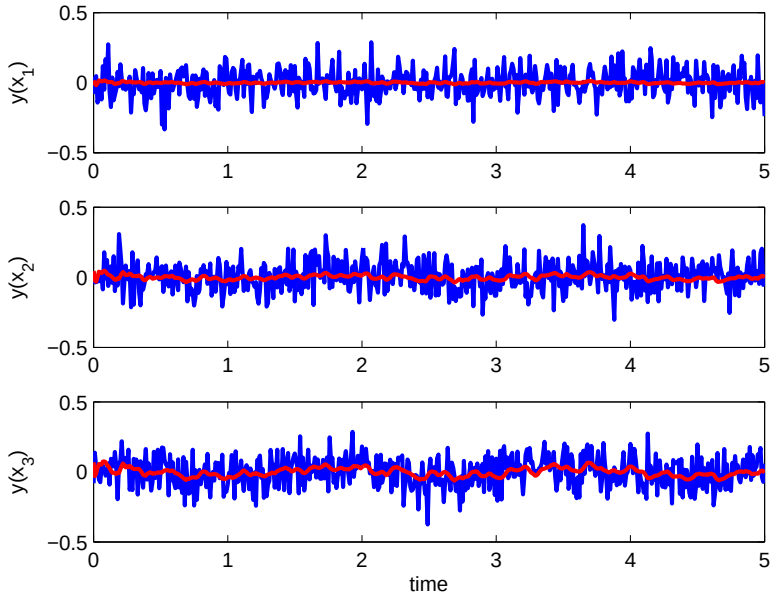

Fig. 101. Actual and Reconstructed Measurements Using Linear Assumed Modes, Case 1: $y(x_1) - y(x_3)$.

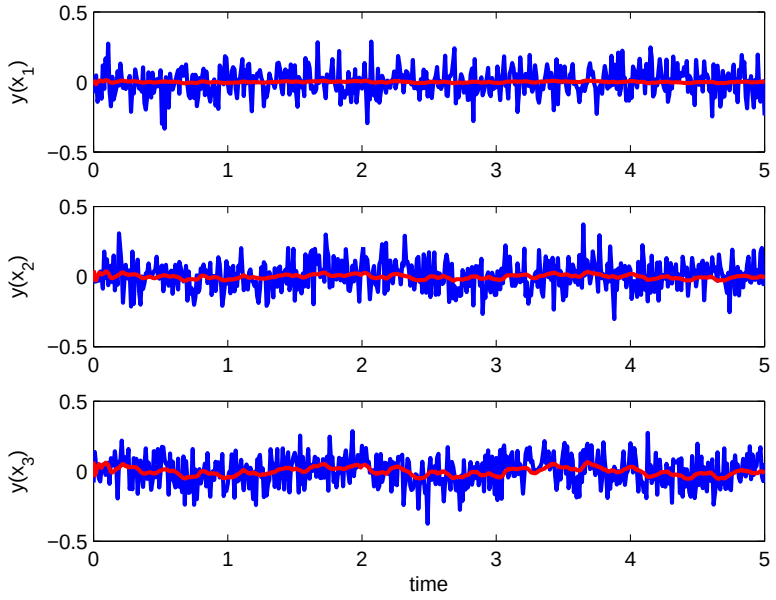

Fig. 102. Actual and Reconstructed Measurements Using Quadratic Assumed Modes, Case 1: $y(x_1) - y(x_3)$.

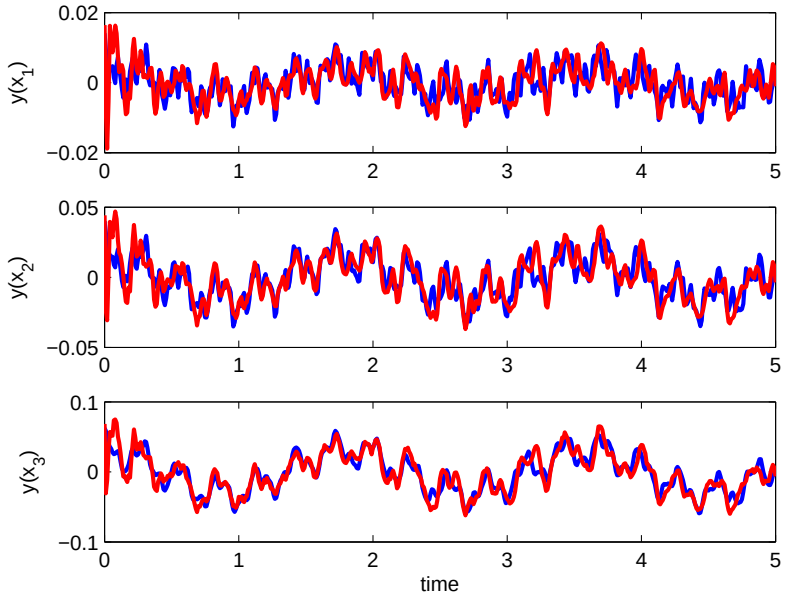

Fig. 103. True and Reconstructed Measurements Using Linear Assumed Modes, Case 1: $y(x_1) - y(x_3)$.

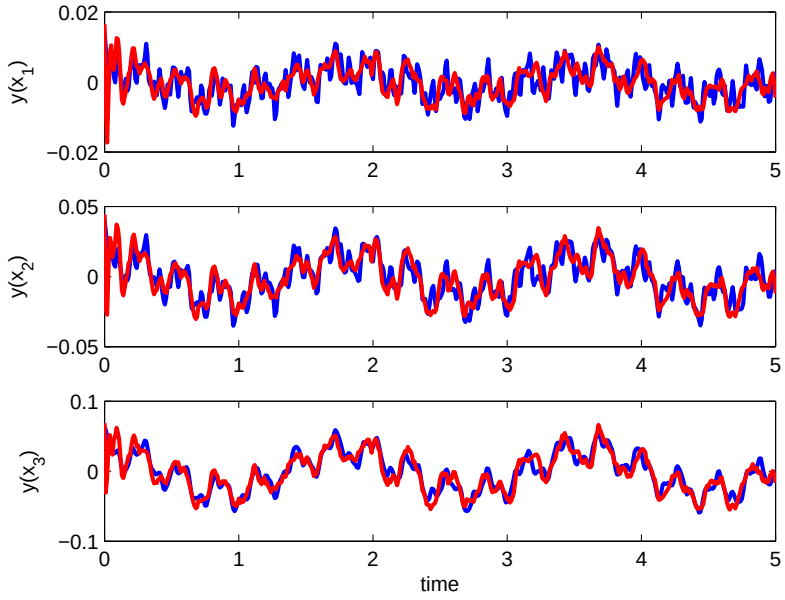

Fig. 104. True and Reconstructed Measurements Using Quadratic Assumed Modes, Case 1: $y(x_1) - y(x_3)$.

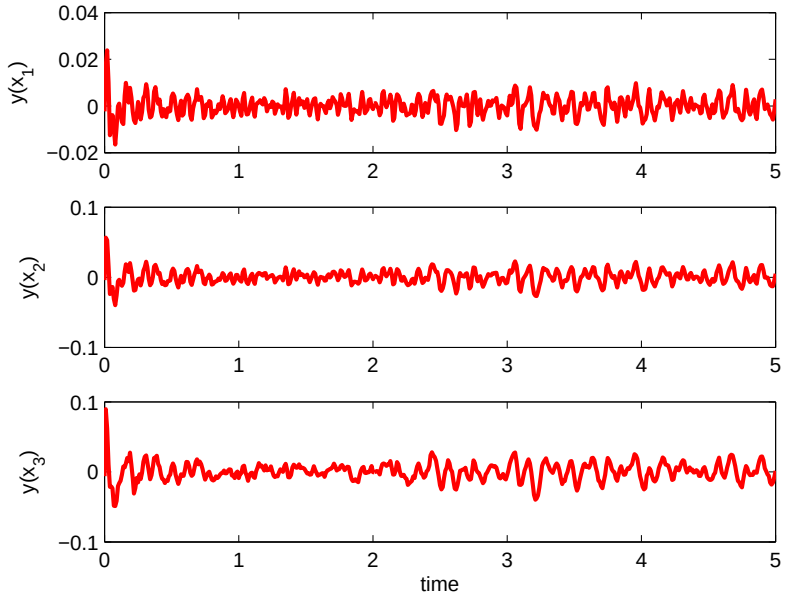

Fig. 105. Error in Reconstructed Measurements Using Linear Assumed Modes, Case 1: $y(x_1) - y(x_3)$.

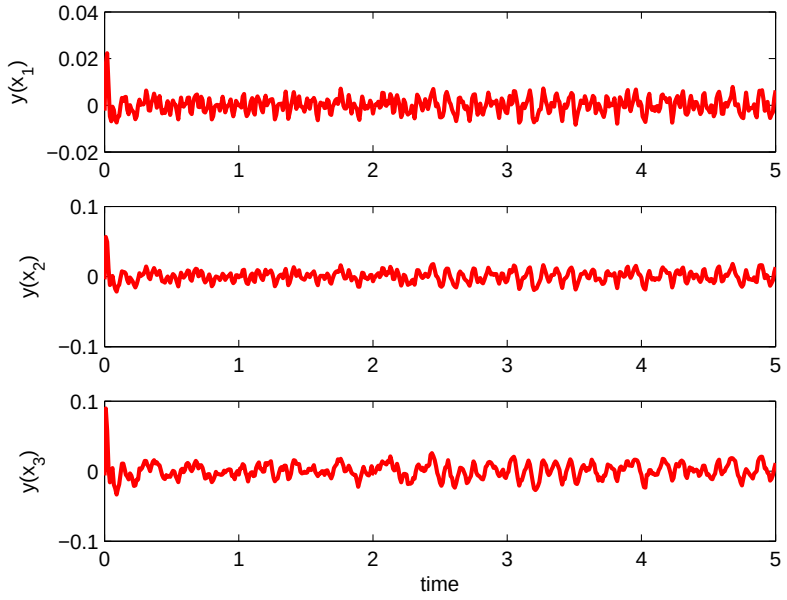

Fig. 106. Error in Reconstructed Measurements Using Quadratic Assumed Modes, Case 1: $y(x_1) - y(x_3)$.

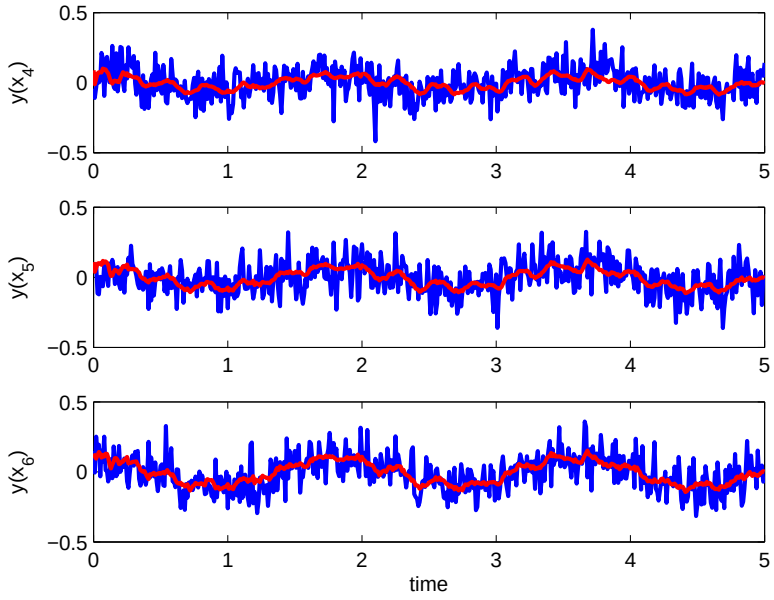

Fig. 107. Actual and Reconstructed Measurements Using Linear Assumed Modes, Case 1: $y(x_4) - y(x_6)$.

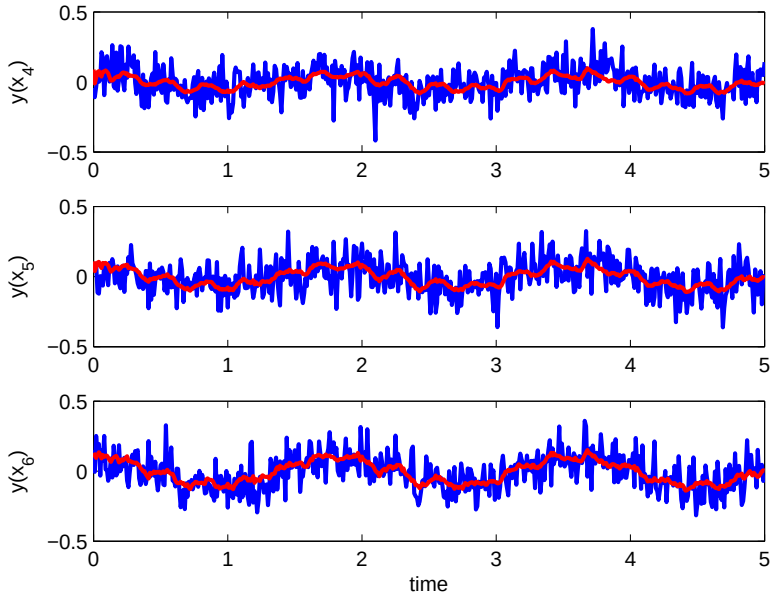

Fig. 108. Actual and Reconstructed Measurements Using Quadratic Assumed Modes, Case 1: $y(x_4) - y(x_6)$.

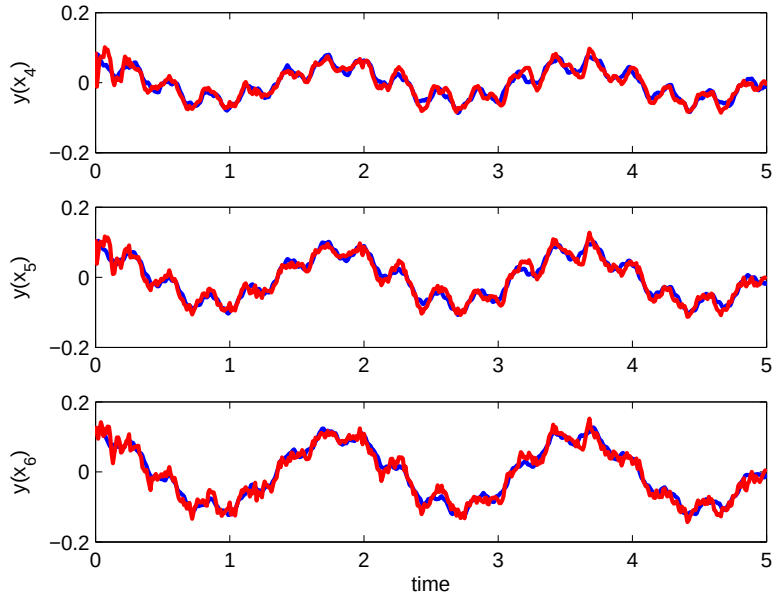

Fig. 109. True and Reconstructed Measurements Using Linear Assumed Modes, Case 1: $y(x_4) - y(x_6)$.

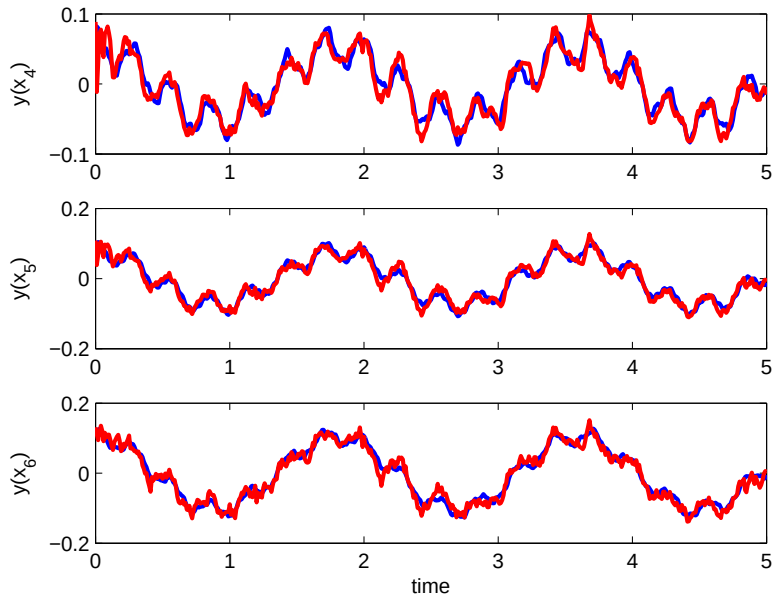

Fig. 110. True and Reconstructed Measurements Using Quadratic Assumed Modes, Case 1: $y(x_4) - y(x_6)$.

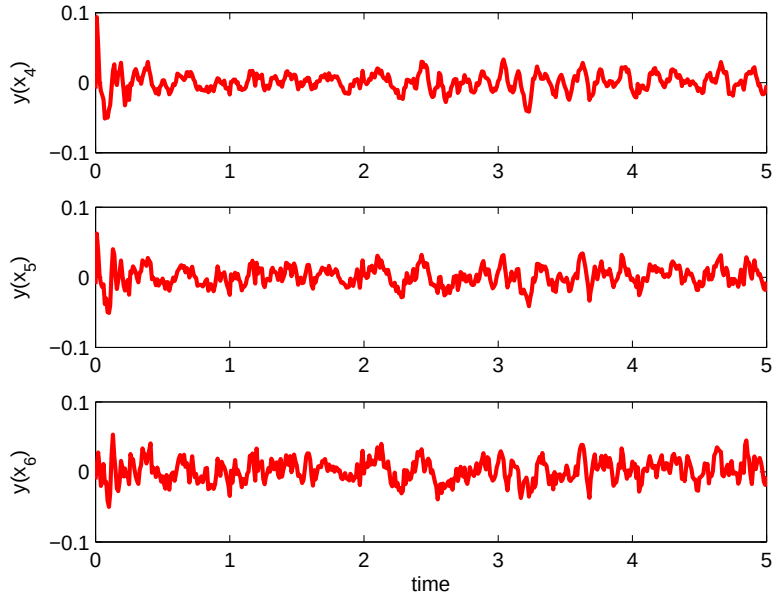

Fig. 111. Error in Reconstructed Measurements Using Linear Assumed Modes, Case 1: $y(x_4) - y(x_6)$.

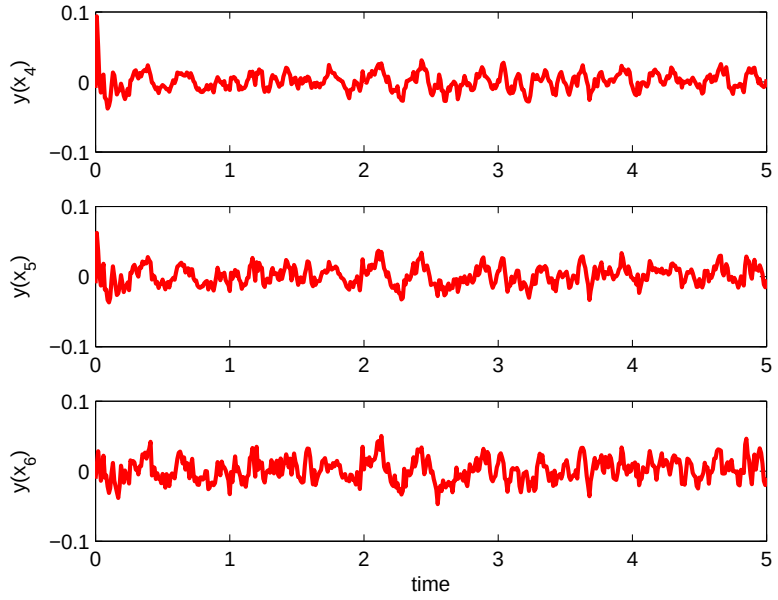

Fig. 112. Error in Reconstructed Measurements Using Quadratic Assumed Modes, Case 1: $y(x_4) - y(x_6)$.

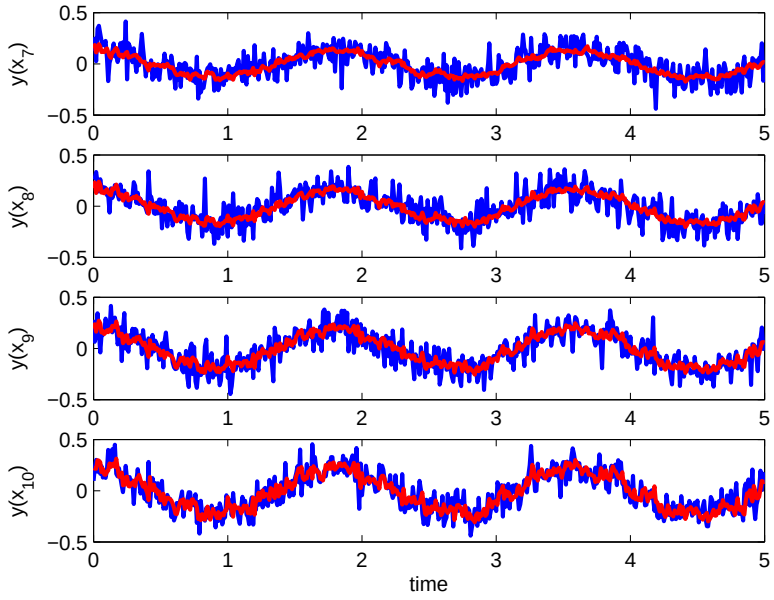

Fig. 113. Actual and Reconstructed Measurements Using Linear Assumed Modes, Case 1: $y(x_7) - y(x_{10})$.

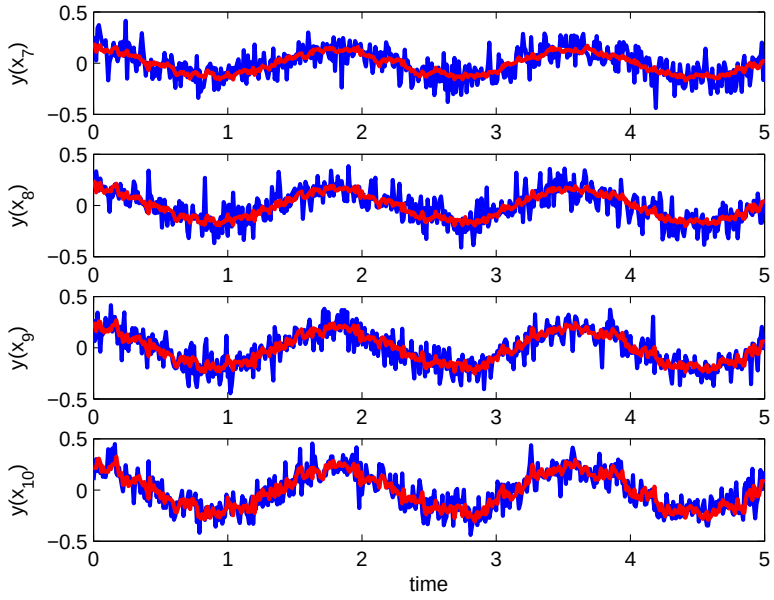

Fig. 114. Actual and Reconstructed Measurements Using Quadratic Assumed Modes, Case 1: $y(x_7) - y(x_{10})$.

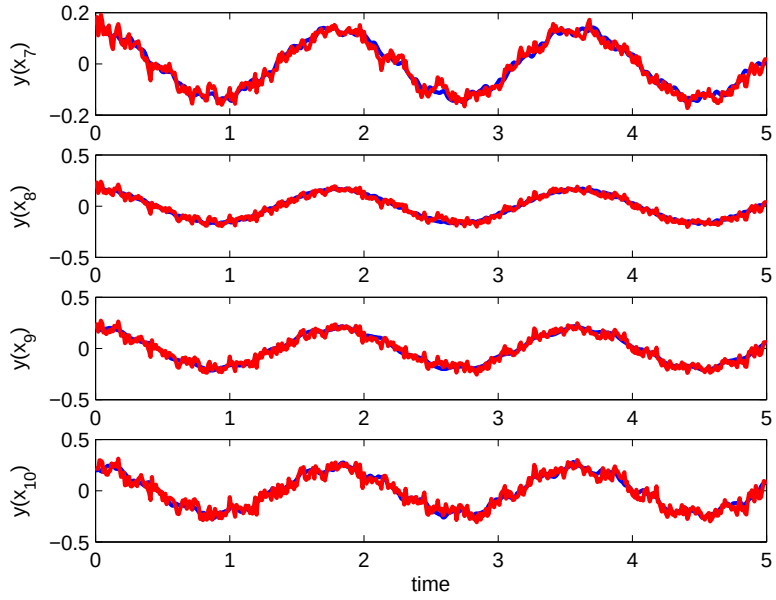

Fig. 115. True and Reconstructed Measurements Using Linear Assumed Modes, Case 1: $y(x_7) - y(x_{10})$.

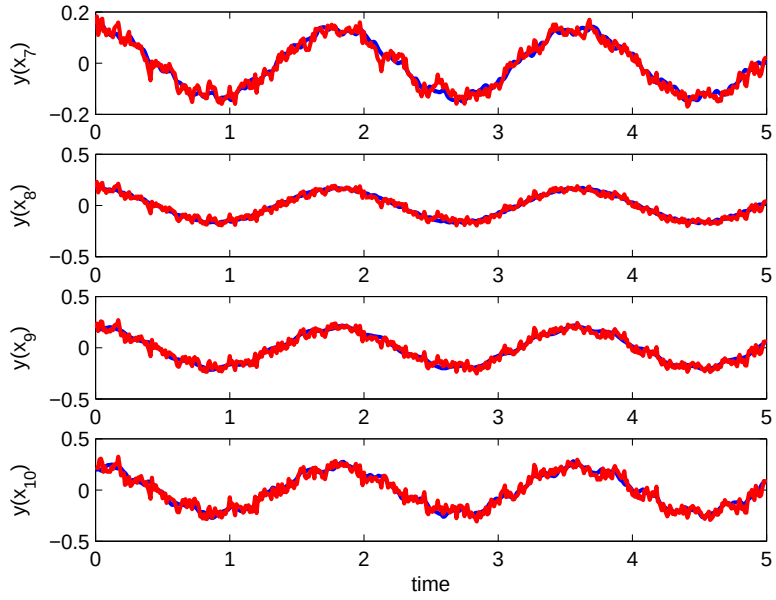

Fig. 116. True and Reconstructed Measurements Using Quadratic Assumed Modes, Case 1: $y(x_7) - y(x_{10})$.

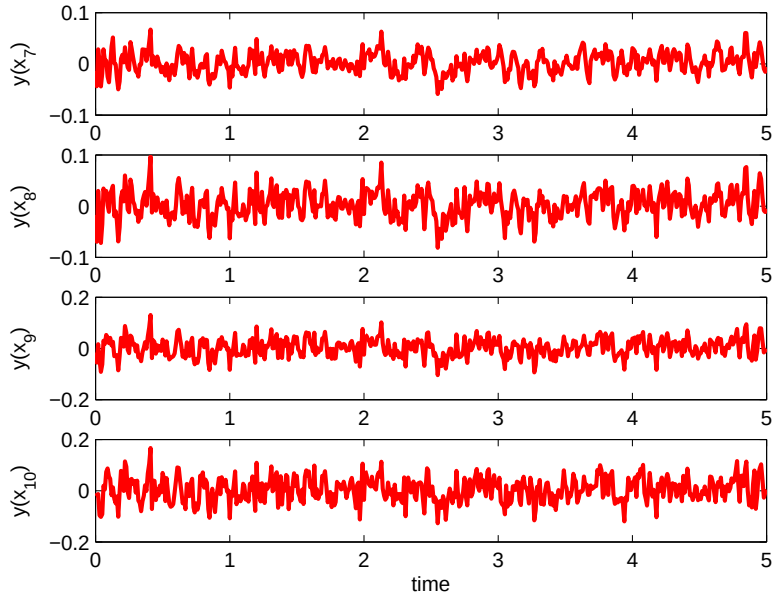

Fig. 117. Error in Reconstructed Measurements Using Linear Assumed Modes, Case 1: $y(x_7) - y(x_{10})$.

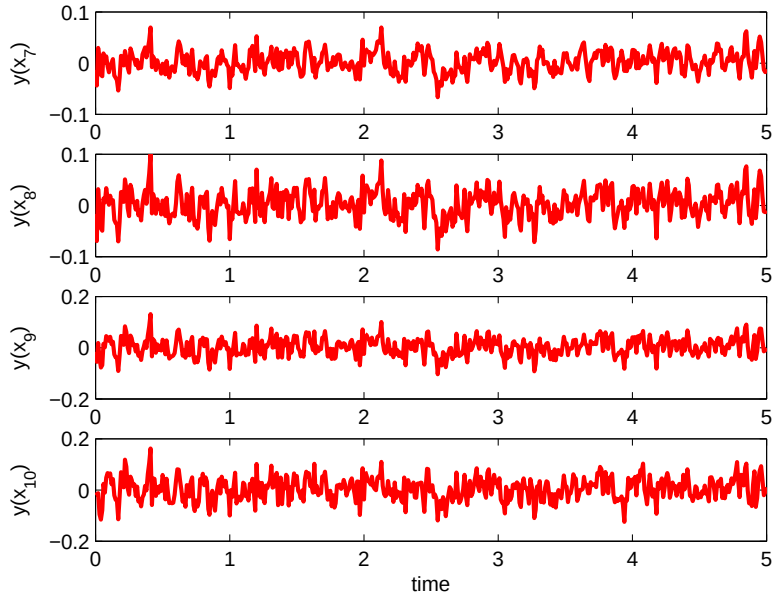

Fig. 118. Error in Reconstructed Measurements Using Quadratic Assumed Modes, Case 1: $y(x_7) - y(x_{10})$.

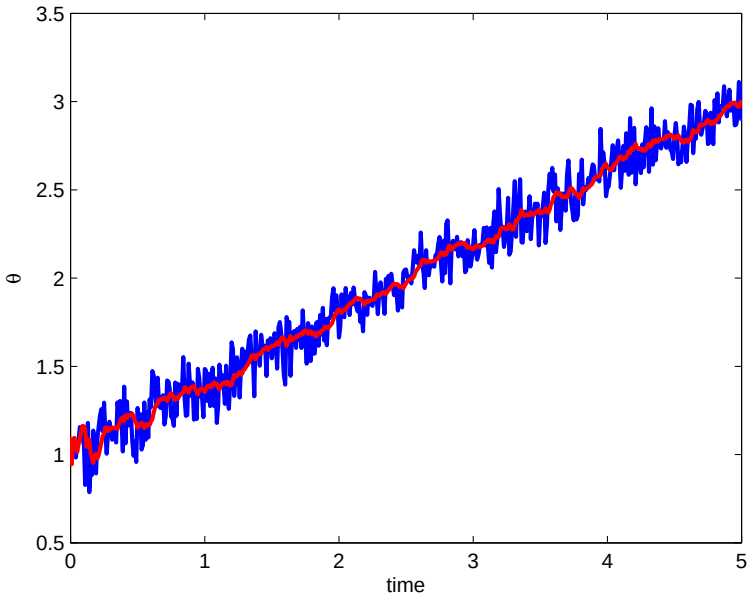

Fig. 119. Actual and Reconstructed Measurements Using Linear Assumed Modes, Case 1: θ, $\dot{\theta}$.

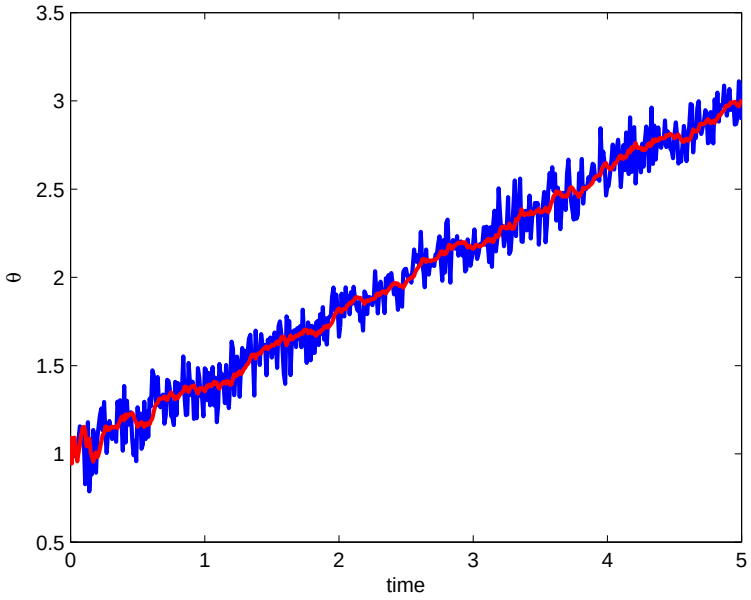

Fig. 120. Actual and Reconstructed Measurements Using Quadratic Assumed Modes, Case 1: θ, $\dot{\theta}$.

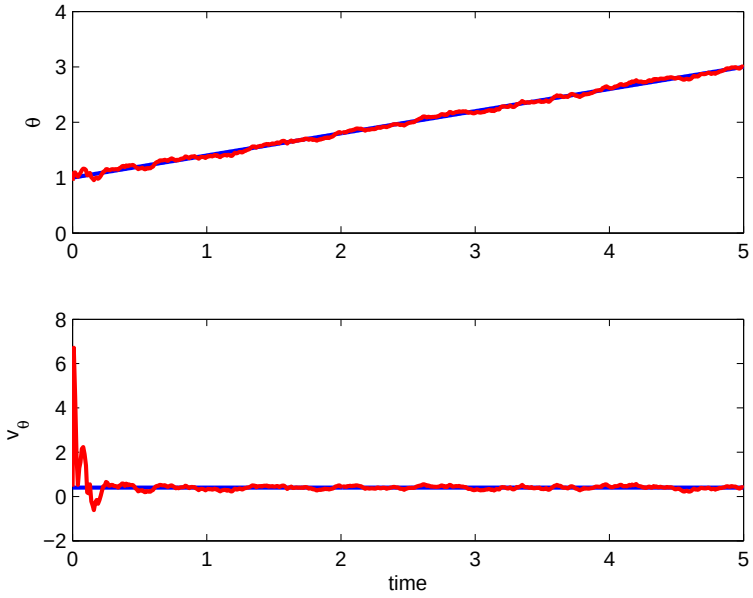

Fig. 121. True and Reconstructed Measurements Using Linear Assumed Modes, Case 1: θ, $\dot{\theta}$.

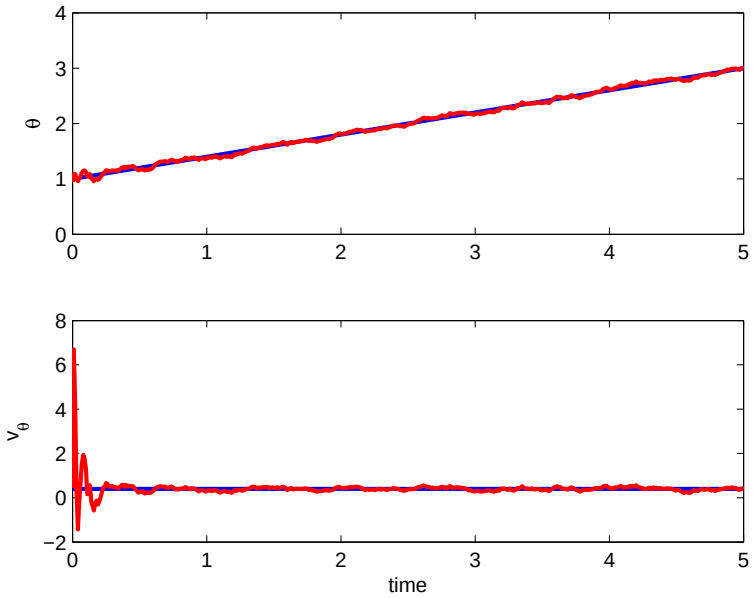

Fig. 122. True and Reconstructed Measurements Using Quadratic Assumed Modes, Case 1: θ, $\dot{\theta}$.

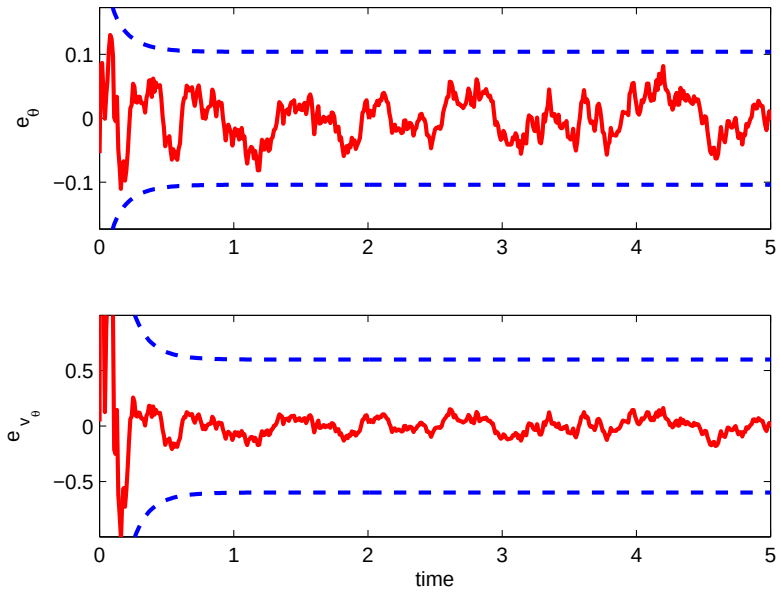

Fig. 123. Error in Reconstructed Measurements Using Linear Assumed Modes, Case 1: θ, $\dot{\theta}$.

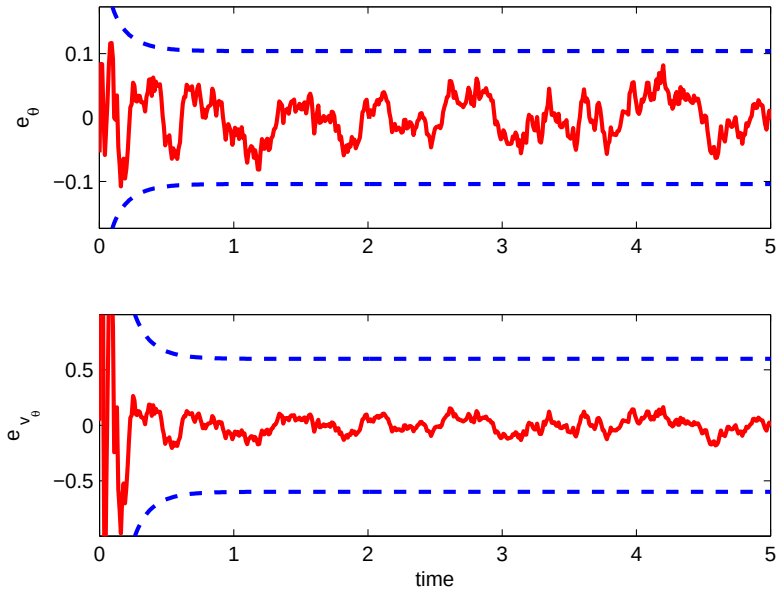

Fig. 124. Error in Reconstructed Measurements Using Quadratic Assumed Modes, Case 1: θ, $\dot{\theta}$.

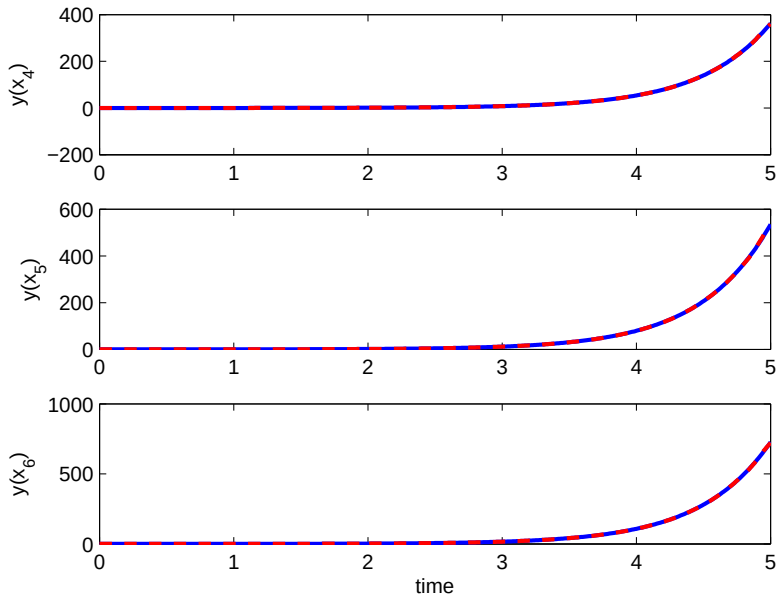

Fig. 125. True and Reconstructed Measurements Using Linear Assumed Modes, Case 2: $y(x_1) - y(x_3)$.

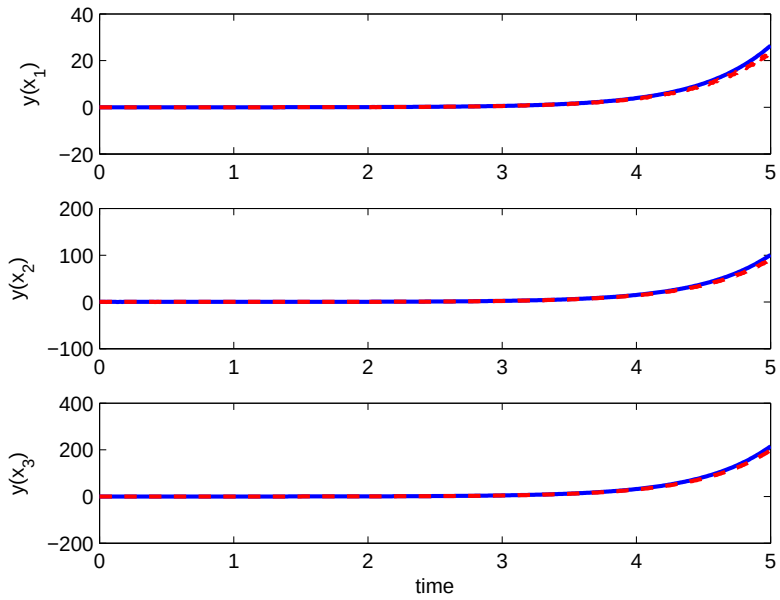

Fig. 126. True and Reconstructed Measurements Using Quadratic Assumed Modes, Case 2: $y(x_1) - y(x_3)$.

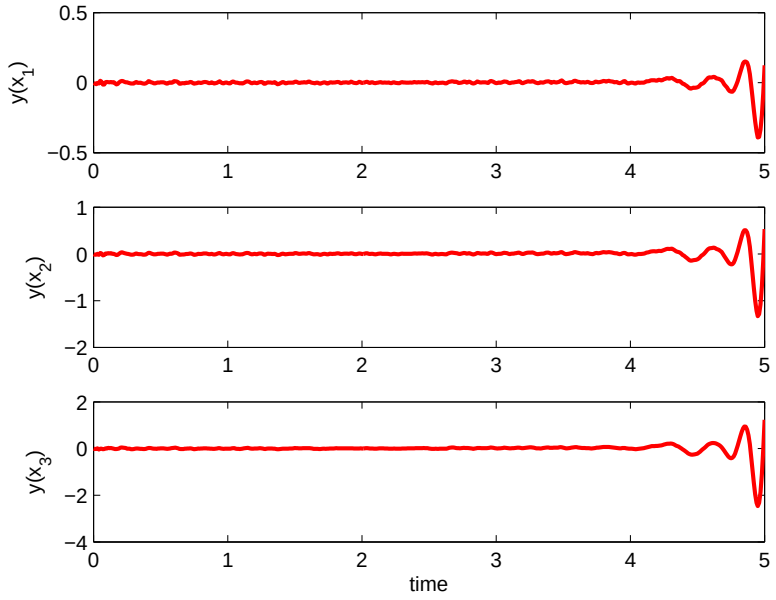

Fig. 127. Error in Reconstructed Measurements Using Linear Assumed Modes, Case 2: $y(x_1) - y(x_3)$.

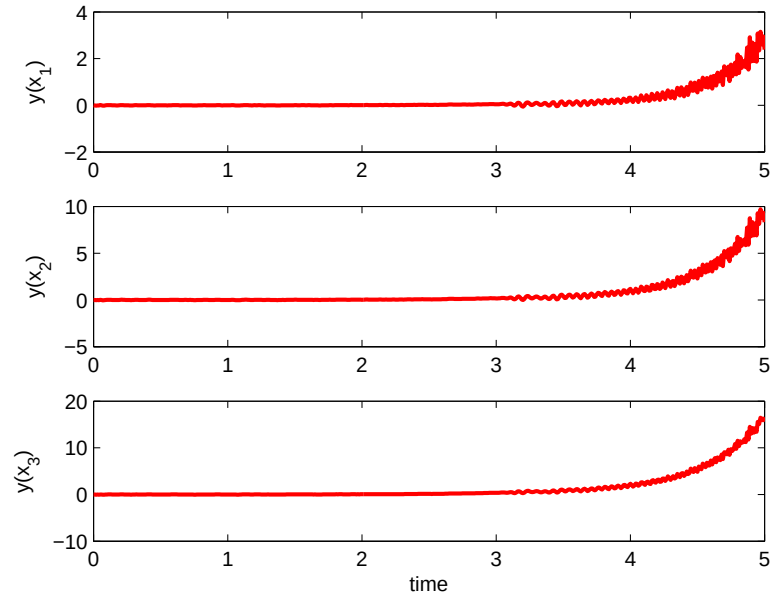

Fig. 128. Error in Reconstructed Measurements Using Quadratic Assumed Modes, Case 2: $y(x_1) - y(x_3)$.

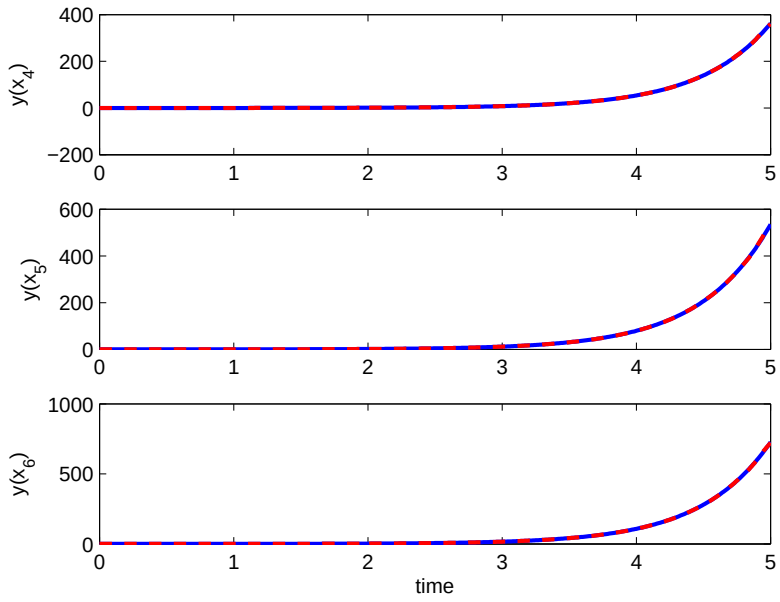

Fig. 129. True and Reconstructed Measurements Using Linear Assumed Modes, Case 2: $y(x_4) - y(x_6)$.

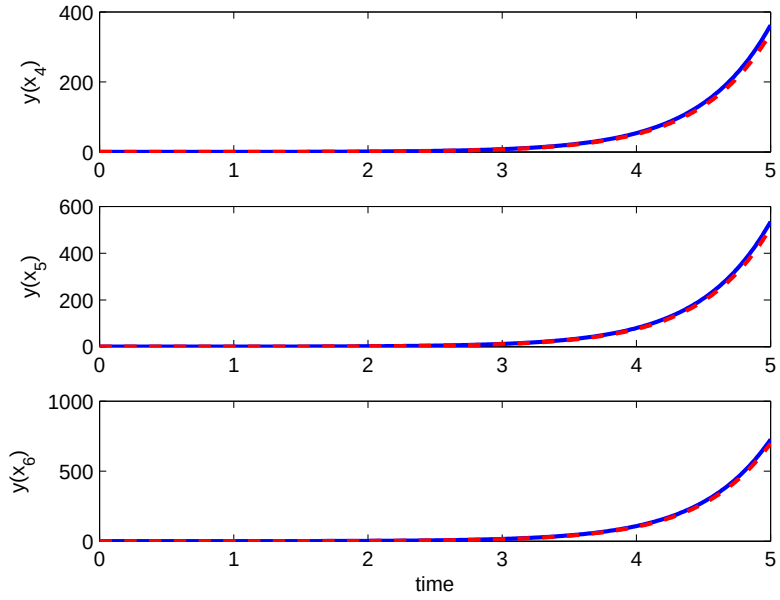

Fig. 130. True and Reconstructed Measurements Using Quadratic Assumed Modes, Case 2: $y(x_4) - y(x_6)$.

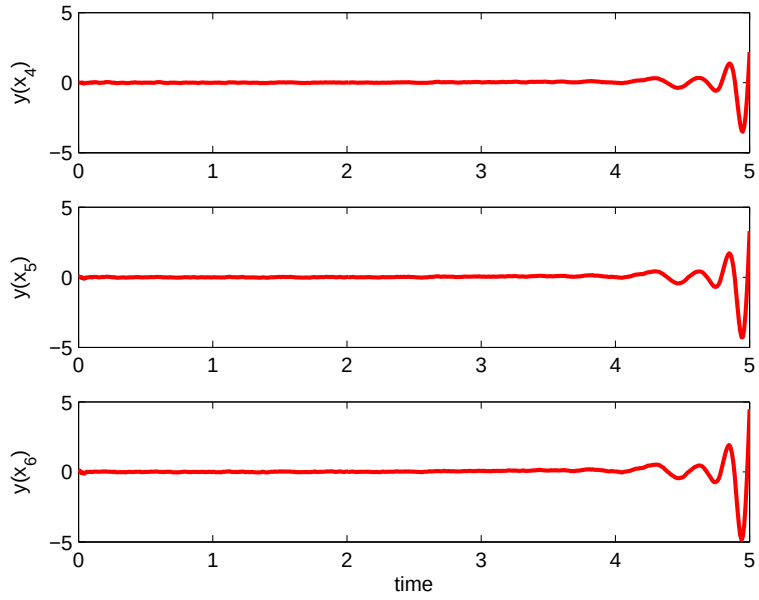

Fig. 131. Error in Reconstructed Measurements Using Linear Assumed Modes, Case 2: $y(x_4) - y(x_6)$.

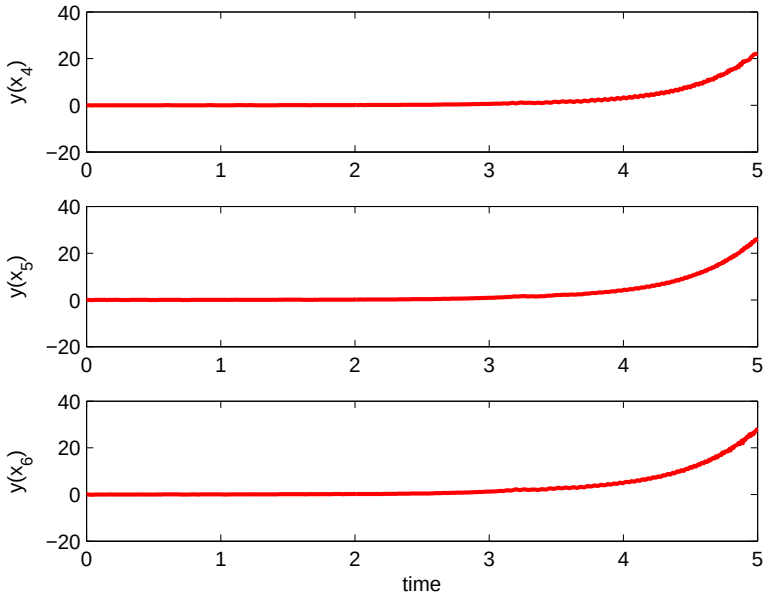

Fig. 132. Error in Reconstructed Measurements Using Quadratic Assumed Modes, Case 2: $y(x_4) - y(x_6)$.

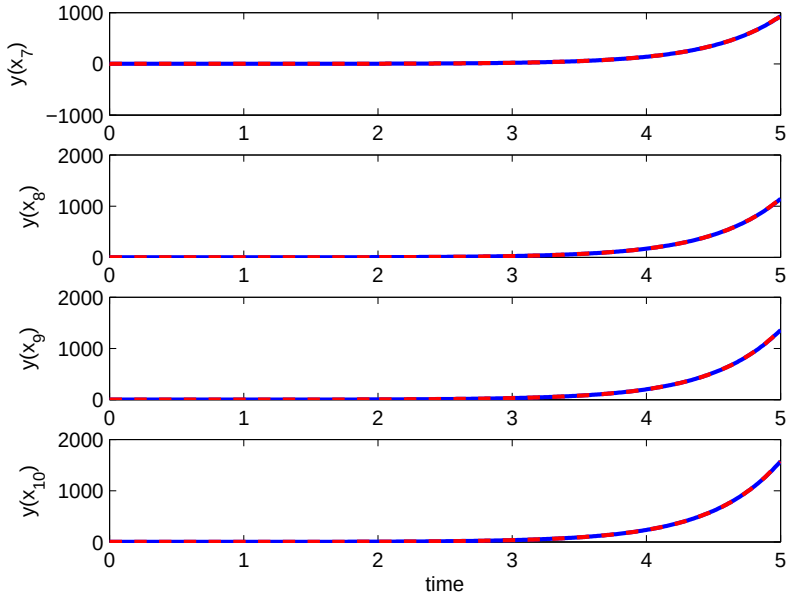

Fig. 133. True and Reconstructed Measurements Using Linear Assumed Modes, Case 2: $y(x_7) - y(x_{10})$.

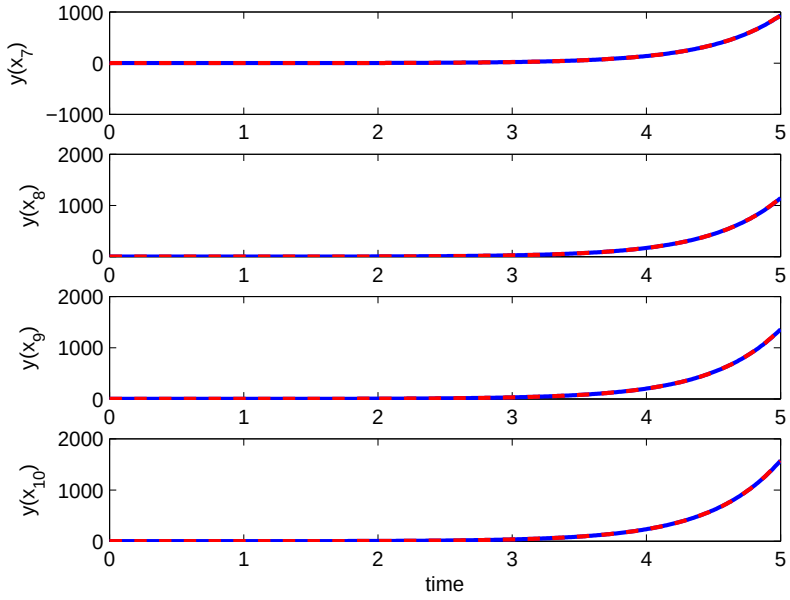

Fig. 134. True and Reconstructed Measurements Using Quadratic Assumed Modes, Case 2: $y(x_7) - y(x_{10})$.

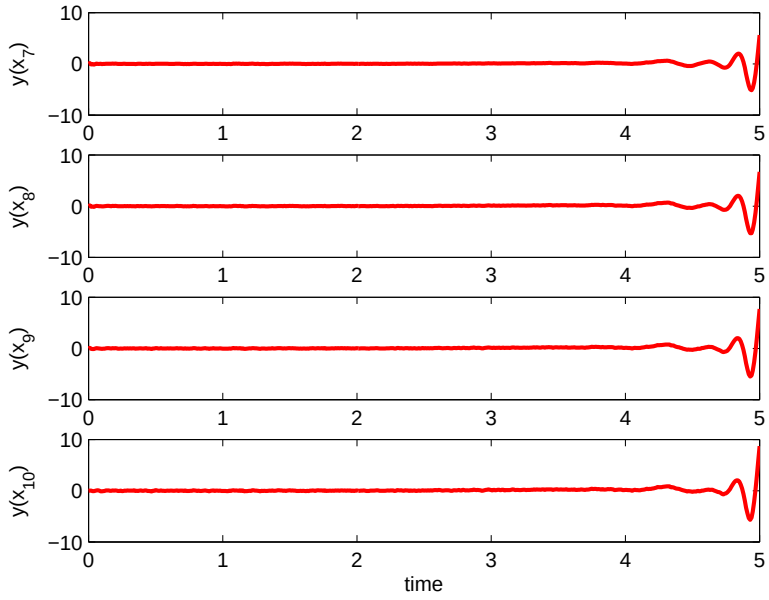

Fig. 135. Error in Reconstructed Measurements Using Linear Assumed Modes, Case 2: $y(x_7) - y(x_{10})$.

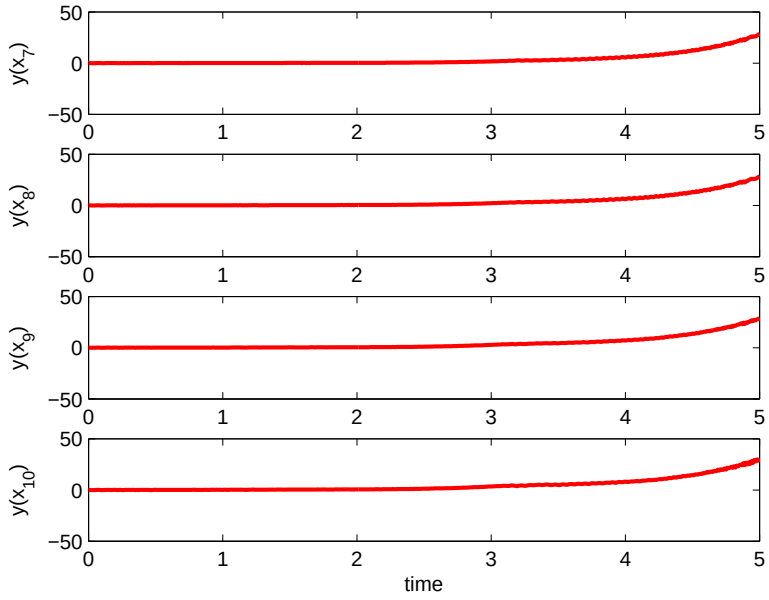

Fig. 136. Error in Reconstructed Measurements Using Quadratic Assumed Modes, Case 2: $y(x_7) - y(x_{10})$.

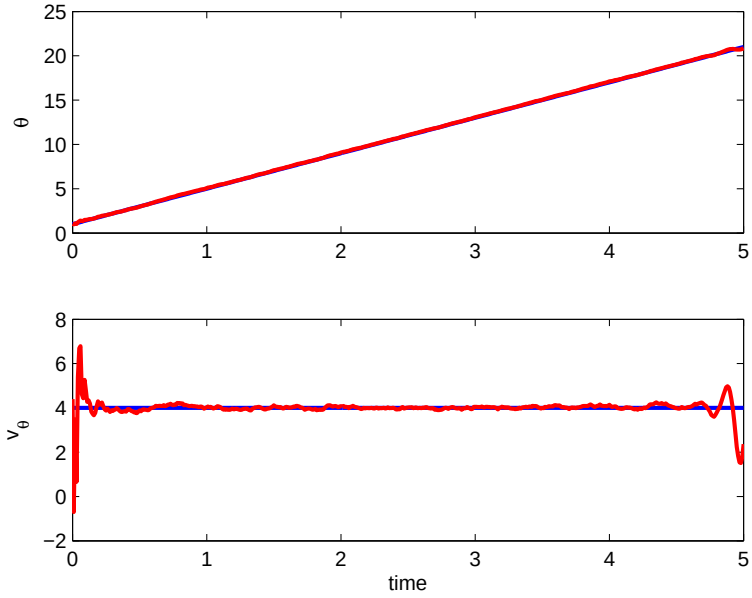

Fig. 137. True and Reconstructed Measurements Using Linear Assumed Modes, Case 2: θ, $\dot{\theta}$.

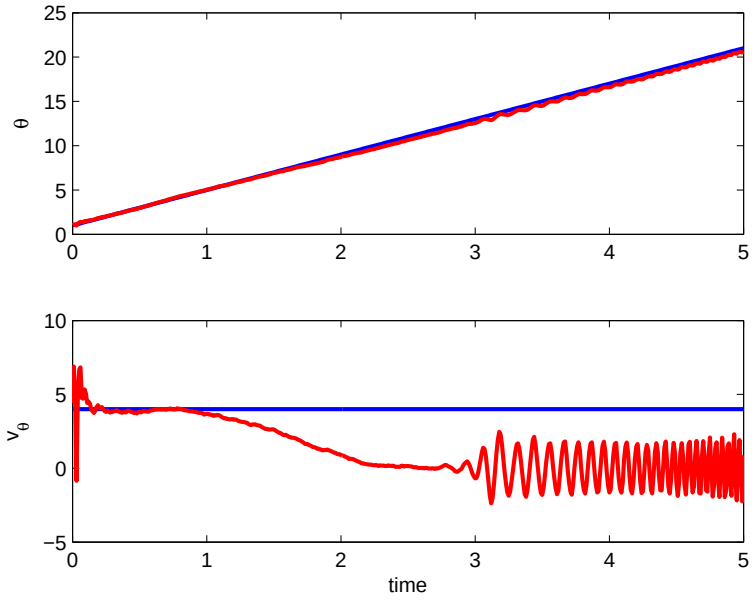

Fig. 138. True and Reconstructed Measurements Using Quadratic Assumed Modes, Case 2: θ, $\dot{\theta}$.

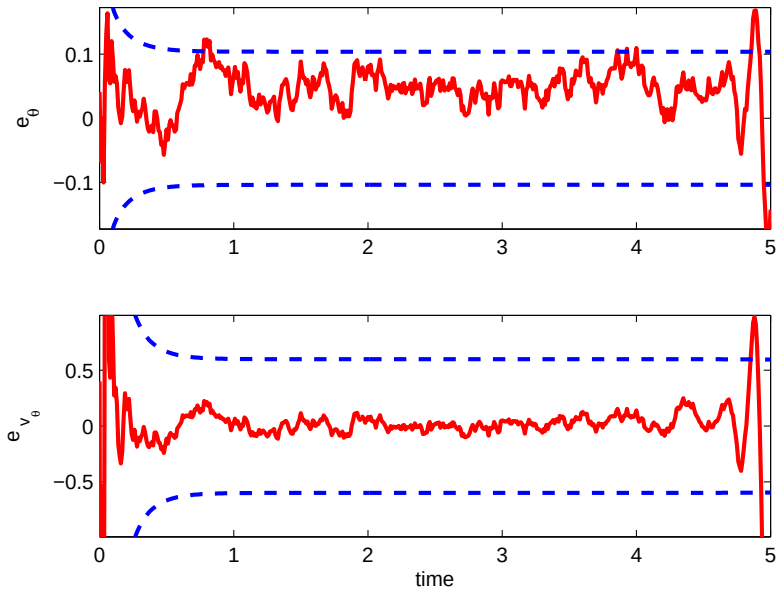

Fig. 139. Error in Reconstructed Measurements Using Linear Assumed Modes, Case 2: θ, $\dot{\theta}$.

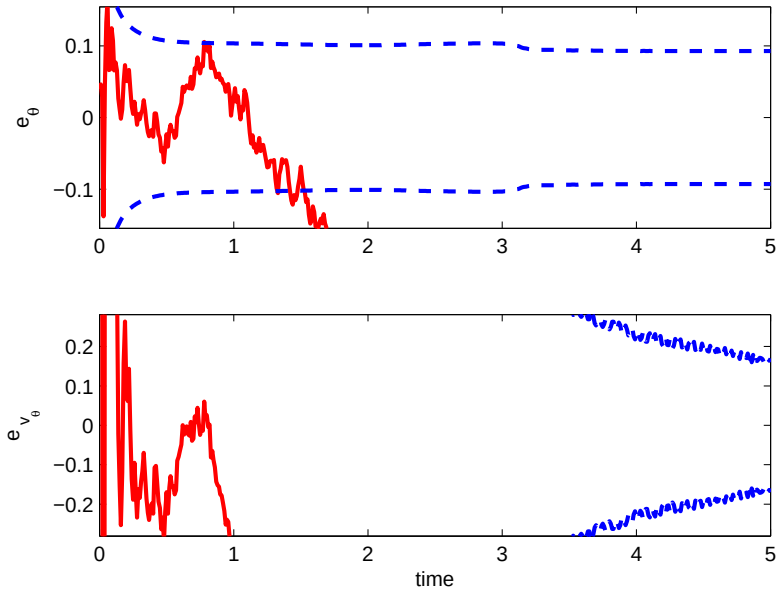

Fig. 140. Error in Reconstructed Measurements Using Quadratic Assumed Modes, Case 2: θ, $\dot{\theta}$.

E. Summary

In this chapter, two finite-dimensional approximations are presented for estimation of hybrid dynamical systems. Both approaches seek to utilize existing variations of the assumed modes method to transform the governing IPDEs into ODEs and subsequently implement the CDEKF. The two methods approximate the infinite-dimensional coordinate, $\mathbf{w}(x,t)$, as a sum of a series of terms composed of a spatial function, $\phi(x)$, and a finite-dimensional time-varying amplitude, $q(t)$. The first method of linear assumed modes is well-known, but the resulting linear equations exhibit undesired behavior for some systems. The second method of quadratic assumed modes requires some additional initial computation, but yields governing equations that better reflect the dynamic behavior of real, physical systems.

The simulations for a slewing satellite reflect these observations. First, both approximations are shown to work well in the CDEKF framework. Next, for the constant angular velocity case, Eigenfunctions are used to create close approximations of "real" measurements to show that both methods can accurately filter these measurements for a stable system. The quadratic assumed modes model more quickly converges to the truth and subsequently reduces error in the states. Further investigation shows that, for the mathematically unstable case of a large angular velocity, the linear assumed modes model provides better initial estimates but later fails to estimate the states altogether. This result is not surprising given the structure of the equations and scale of the unstable measurements. For the unstable case both estimation methods reach their limitations as the (physically) impossible large deformations quickly outgrow the order of other states and parameters of the system. Overall, the results indicate that using quadratic assumed modes to create a linear, finite-dimensional model of the flexible body is more advantageous for physical systems.

CHAPTER VII

DIRECT ESTIMATION

The ability of direct linearization for dynamic system modeling to bypass the nonlinear equations en route to the linearized equations, as described in Ch. III, begs the question: "Can this direct treatment be applied to estimation?" In this chapter, a straightforward approach for constructing the elements of the CDEKF for a linearized system are presented. First, a brief overview of the direct linearization method from a Lagrangian perspective is outlined. The extensions of these ideas to estimation in the CDEKF framework are then presented.

A. Departure Motion

Direct linearization for a discrete system about an equilibrium point is available in the literature [9]. For estimation applications, though, the linearized motion about a nonlinear reference trajectory may be of greater interest. The CDEKF is itself based on this premise [1].

First, consider the form of the governing nonlinear equations for the system.

$$\dot{\boldsymbol{x}}(t) = \boldsymbol{f}(\boldsymbol{x}, \boldsymbol{u}, t) \tag{7.1}$$

Here, $\boldsymbol{x}$ are the states of the system, and $\boldsymbol{u}$ are the system controls. The measurements associated with this motion have the following nonlinear measurement model.

$$\boldsymbol{y}_m = \boldsymbol{h}(\boldsymbol{x}, \boldsymbol{u}, t) \tag{7.2}$$

The differential equations and measurement model for the nominal reference trajectory are then respectively Eqs. 7.1 and 7.2 evaluated at $\{\boldsymbol{x}^*, \boldsymbol{u}^*, t\}$. In this chapter,

the superscript $(^*)$ indicates the reference motion.

Now define the true motion of the system to be the sum of the reference motion and a *departure motion*, which is a perturbation of the system states from the reference trajectory.

$$\boldsymbol{x} = \boldsymbol{x}^* + \delta\boldsymbol{x} \tag{7.3}$$

Similarly, the true measurements and controls are given by the following equations.

$$\boldsymbol{y} = \boldsymbol{y}^* + \delta\boldsymbol{y} \tag{7.4}$$

$$\boldsymbol{u} = \boldsymbol{u}^* + \delta\boldsymbol{u} \tag{7.5}$$

Traditionally, the governing equations for the departure motion are written using a first-order Taylor series approximation.

$$\delta\dot{\boldsymbol{x}} = F(t)\delta\boldsymbol{x} + B(t)\delta\boldsymbol{u} \tag{7.6}$$

$$\delta\boldsymbol{y}_m = H(t)\delta\boldsymbol{x} + D(t)\delta\boldsymbol{u} \tag{7.7}$$

For these equations, the F and H matrices are defined as shown below.

$$\begin{aligned} F(t) &= \left.\frac{\partial \boldsymbol{f}}{\partial \boldsymbol{x}}\right|_{\boldsymbol{x},^*\boldsymbol{u},^*} \quad ; \quad B(t) = \left.\frac{\partial \boldsymbol{f}}{\partial \boldsymbol{u}}\right|_{\boldsymbol{x},^*\boldsymbol{u},^*} \\ H(t) &= \left.\frac{\partial \boldsymbol{h}}{\partial \boldsymbol{x}}\right|_{\boldsymbol{x},^*\boldsymbol{u},^*} \quad ; \quad D(t) = \left.\frac{\partial \boldsymbol{h}}{\partial \boldsymbol{u}}\right|_{\boldsymbol{x},^*\boldsymbol{u},^*} \end{aligned} \tag{7.8}$$

In this work, the relationship for $\delta\boldsymbol{y}_m$ is retained. However, the equation for $\delta\dot{\boldsymbol{x}}$ is explored a little further.

B. Direct Linearization via the Lagrangian

Here, a brief overview of direct linearization for discrete systems is discussed [9, 36]. Note that direct linearization via the Gibbs function is presented in Ch. III for constrained systems with quasi-velocities, and a Lagrangian direct linearization

treatment for continuous and hybrid dynamical systems by the author is available in Ref. [19]. Each of these concerns motions about equilibrium. Here, non-equilibrium reference trajectory motions are considered.

To start, consider the form of a position vector for an element of a discrete system as a function of n generalized coordinates, $\boldsymbol{q}(t)$, and (explicitly) time.

$$\boldsymbol{r} = \boldsymbol{r}(\boldsymbol{q}, t) \tag{7.9}$$

Taking the frame-independent time derivative yields the velocity vector.

$$\dot{\boldsymbol{r}} = \frac{\partial \boldsymbol{r}}{\partial q_i}\frac{\mathrm{d}q_i}{\mathrm{d}t} + \frac{\partial \boldsymbol{r}}{\partial t} = \frac{\partial \boldsymbol{r}}{\partial q_i}\dot{q}_i + \frac{\partial \boldsymbol{r}}{\partial t} = \boldsymbol{\tau}_i \dot{q}_i + \boldsymbol{\tau}_0 \tag{7.10}$$

Here, $\boldsymbol{\tau}_i$ and $\boldsymbol{\tau}_0$ are called the Lagrangian vectors, among other names [11]. The kinetic energy can then be formed.

$$T = \frac{1}{2} m \left(\dot{\boldsymbol{r}} \cdot \dot{\boldsymbol{r}} \right) = \frac{1}{2} m \left(\boldsymbol{\tau}_i \cdot \boldsymbol{\tau}_j \dot{q}_i \dot{q}_j + 2 \boldsymbol{\tau}_i \cdot \boldsymbol{\tau}_0 \dot{q}_i + \boldsymbol{\tau}_0 \cdot \boldsymbol{\tau}_0 \right) \tag{7.11}$$

One characteristic of the direct linearization method is to first partition this function into three categories, T_2, T_1, and T_0. Terms quadratic in, linear in, and independent of the generalized velocities compose T_2, T_1, and T_0 respectively.

$$T_2 = \frac{1}{2} m \left(\boldsymbol{\tau}_i \cdot \boldsymbol{\tau}_j \dot{q}_i \dot{q}_j \right) \quad ; \quad T_1 = m \left(\boldsymbol{\tau}_i \cdot \boldsymbol{\tau}_0 \dot{q}_i \right) \quad ; \quad T_0 = \frac{1}{2} m \left(\boldsymbol{\tau}_0 \cdot \boldsymbol{\tau}_0 \right) \tag{7.12}$$

Note that the T_1 and T_0 terms exist only for rheonomic systems, which are explicitly a function of time (unlike scleronomic systems). This expression for the kinetic energy can be combined the potential energy, here assumed have the form $V = V(q)$, to construct the Lagrangian.

$$L = L(\dot{\boldsymbol{q}}, \boldsymbol{q}, t) = T_2(\dot{\boldsymbol{q}}, \boldsymbol{q}, t) + T_1(\dot{\boldsymbol{q}}, \boldsymbol{q}, t) + T_0(\boldsymbol{q}, t) - V(\boldsymbol{q}) \tag{7.13}$$

Consider now an alternative path to the direct linearization solution in lieu of the classic "quadraticize" method [9, 36]. The traditional method applies a Taylor series approximation to the Lagrangian, retains 2^{nd}-order terms, and then employs Lagrange's equations for discrete systems (reproduced from Ch. II here).

$$\frac{\mathrm{d}}{\mathrm{dt}}\left(\frac{\partial L}{\partial \dot{q}_j}\right) - \frac{\partial L}{\partial q_j} = Q_j \tag{7.14}$$

Here, Lagrange's equations are instead applied first and then followed with a Taylor series approximation retaining only 1^{st}-order terms. It can been shown that the nature of partial differentiation causes the resulting equations to be the same as those constructed with the classic approach [19].

Using the partitioned form of the Lagrangian, Eq. 7.14 yields the following non-linear equation.

$$\left[\frac{\partial^2 T_2}{\partial \dot{q}_j \partial \dot{q}_i}\right]\ddot{q}_i + \left[\frac{\partial^2 (T_2+T_1)}{\partial \dot{q}_j \partial q_i}\right]\dot{q}_i + \left[\frac{\partial (T_2+T_1)}{\partial t \partial \dot{q}_j}\right] - \frac{\partial (T_2+T_1+T_0-V)}{\partial q_j} - Q_j = 0 \tag{7.15}$$

For this exercise, partial differentiation with respect to time indicates explicit differentiation only. Thus, if $f = f(y_i(x,t), x, t)$, then $\partial f/\partial t = \partial f/\partial t$ only, and $\partial f/\partial t \neq (\partial f/\partial y_i)(\partial y_i/\partial t) + \partial f/\partial t$. Also note that the generalized forces are assumed to be a function of m system controls or time, or both, $Q_j = Q_j(u_r, t)$.

The next step is to linearize Eq. 7.15. Let g be defined as the left side of Eq. 7.15, and let $\boldsymbol{x}^* = [\boldsymbol{q}^*, \dot{\boldsymbol{q}}^*]$ represent the vector of generalized positions and velocities evaluated at the reference trajectory. Linearizing about this trajectory, $\{\boldsymbol{x}^*, \boldsymbol{u}^*\}$, defining

$\delta \boldsymbol{x} = \boldsymbol{x} - \boldsymbol{x}^*$, and retaining only linear terms gives the following expansion.

$$
\begin{aligned}
0 &= g(\ddot{q}_j, \dot{q}_j, q_j, u_r, t) \\
&\approx g|_{\boldsymbol{x}^*, \boldsymbol{u}^*} + \left[\frac{\partial g}{\partial \ddot{q}_k}\right]_{\boldsymbol{x}^*} \delta\ddot{q}_k + \left[\frac{\partial g}{\partial \dot{q}_k}\right]_{\boldsymbol{x}^*} \delta\dot{q}_k + \left[\frac{\partial g}{\partial q_k}\right]_{\boldsymbol{x}^*} \delta q_k + \left[\frac{\partial g}{\partial u_r}\right]_{\boldsymbol{u}^*} \delta u_r + \dots \\
&\approx \left[\frac{\partial^2 T_2}{\partial \dot{q}_i \partial \dot{q}_j}\delta_{jk}\right]_{\boldsymbol{x}^*} \delta\ddot{q}_k + \left[\frac{\partial^2 (T_2 + T_1)}{\partial \dot{q}_i \partial q_j}\delta_{jk} - \frac{\partial^2 (T_2 + T_1)}{\partial q_i \partial \dot{q}_k} + \frac{\partial^3 T_2}{\partial t \partial \dot{q}_j \partial \dot{q}_k}\right]_{\boldsymbol{x}^*} \delta\dot{q}_k \\
&\quad + \left[\frac{\partial^3 (T_2 + T_1)}{\partial t \partial \dot{q}_i \partial q_k} + \frac{\partial^3 T_2}{\partial \dot{q}_i \partial \dot{q}_j \partial q_k}\ddot{q}_j + \frac{\partial^3 (T_2 + T_1)}{\partial \dot{q}_1 \partial q_j \partial q_k}\dot{q}_j - \frac{\partial^2 (T_2 + T_1 + T_0 - V)}{\partial q_i \partial q_k}\right]_{\boldsymbol{x}^*} \delta q_k \\
&\quad - \left[\frac{\partial Q_i}{\partial u_r}\right]_{\boldsymbol{u}^*} \delta u_r + \dots
\end{aligned}
\tag{7.16}
$$

For scleronomic systems that are linearized about an equilibrium point and are only subject to potential forces, this equation reduces to the traditional direct linearization result for discrete systems.

$$
\begin{aligned}
0 &\approx \left[\frac{\partial^2 T_2}{\partial \dot{q}_i \partial \dot{q}_k}\right]_{eq} \delta\ddot{q}_k + \left[\frac{\partial^2 T_1}{\partial \dot{q}_i \partial q_k} - \frac{\partial^2 + T_1}{\partial q_i \partial \dot{q}_k}\right]_{eq} \delta\dot{q}_k - \left[\frac{\partial^2 (T_0 - V)}{\partial q_i \partial q_k}\right]_{eq} \delta q_k \\
&\approx m_{ij}\delta\ddot{q}_j + (z_{ji} - z_{ij})\delta\dot{q}_j + k_{ij}\delta q_j
\end{aligned}
\tag{7.17}
$$

This form allows one to calculate the three partial derivative matrices (m_{ij}, z_{ij}, k_{ij}) from the Lagrangian and substitute these coefficient matrices into the above equation. That is, one can form the kinetic and potential energies and directly write the linearized equations without first forming the nonlinear equations.

Returning to the more generalized case (i.e., rheonomic), Eq. 7.16 yields the linearized equations about the reference trajectory.

$$
\begin{aligned}
\left[\frac{\partial Q_i}{\partial u_r}\right]_{\boldsymbol{u}^*} \delta u_r &= \left[\frac{\partial^2 T_2}{\partial \dot{q}_i \partial \dot{q}_k}\right]_{\boldsymbol{x}^*} \delta\ddot{q}_k + \left[\frac{\partial^2 (T_2 + T_1)}{\partial \dot{q}_i \partial q_k} - \frac{\partial^2 (T_2 + T_1)}{\partial q_i \partial \dot{q}_k} + \frac{\partial^3 T_2}{\partial t \partial \dot{q}_j \partial \dot{q}_k}\right]_{\boldsymbol{x}^*} \delta\dot{q}_k \\
&\quad + \left[\frac{\partial^3 (T_2 + T_1)}{\partial t \partial \dot{q}_i \partial q_k} + \frac{\partial^3 T_2}{\partial \dot{q}_i \partial \dot{q}_j \partial q_k}\ddot{q}_j + \frac{\partial^3 (T_2 + T_1)}{\partial \dot{q}_i \partial q_j \partial q_k}\dot{q}_j - \frac{\partial^2 (T_2 + T_1 + T_0 - V)}{\partial q_i \partial q_k}\right]_{\boldsymbol{x}^*} \delta q_k
\end{aligned}
\tag{7.18}
$$

The coefficient matrices are defined as follows.

$$\begin{aligned} m_{ij}(t) &= \left[\frac{\partial^2 T_2}{\partial \dot{q}_i \partial \dot{q}_j}\right]_{\boldsymbol{x}^*} \quad ; \quad z_{ij}(t) = \left[\frac{\partial^2 (T_2 + T_1)}{\partial \dot{q}_i \partial q_j}\right]_* \\ k_{ij}(t) &= -\left[\frac{\partial^2 (T_2 + T_1 + T_0 - V)}{\partial q_i \partial q_j}\right]_{\boldsymbol{x}^*} \quad ; \quad n_{ij}(t) = \left[\frac{\partial^3 T_2}{\partial \dot{q}_i \partial q_j \partial \dot{q}_k}\ddot{q}_k\right]_* \\ p_{ij}(t) &= \left[\frac{\partial^3 (T_2 + T_1)}{\partial \dot{q}_i \partial q_j \partial q_k}\dot{q}_k\right]_{\boldsymbol{x}^*} \quad ; \quad b_{ir}(t) = \left[\frac{\partial Q_i}{\partial u_r}\right]_{\boldsymbol{u}^*} \end{aligned} \tag{7.19}$$

The resulting directly linearized equations for the departure motion can then be written in a condensed form.

$$m_{ij}\delta\ddot{q}_j + \Big(\dot{m}_{ij} + z_{ij} - z_{ji}\Big)\delta\dot{q}_j + \Big(\dot{z}_{ij} + n_{ij} + p_{ij} + k_{ij}\Big)\delta q_j = b_{ir}\delta u_r \tag{7.20}$$

Here, an overdot on a coefficient indicates (explicit) partial differentiation with respect to time. This equation can also be written in matrix form.

$$M\delta\ddot{\boldsymbol{q}} + \Big(\dot{M} + Z + Z^T\Big)\delta\dot{\boldsymbol{q}} + \Big(\dot{Z} + N + P + K\Big)\delta\boldsymbol{q} = B\delta\boldsymbol{u} \tag{7.21}$$

Assuming the mass matrix is invertible, one can solve for generalized accelerations.

$$\delta\ddot{\boldsymbol{q}} = -M^{-1}\Big(\dot{M} + Z + Z^T\Big)\delta\dot{\boldsymbol{q}} - M^{-1}\Big(\dot{Z} + N + P + K\Big)\delta\boldsymbol{q} + M^{-1}B\delta\boldsymbol{u} \tag{7.22}$$

Defining $\delta\boldsymbol{x} = [\delta\boldsymbol{q};\, \delta\dot{\boldsymbol{q}}]$, the entire set of linearized state equations can be written using a state-vector form.

$$\delta\dot{\boldsymbol{x}} = \begin{bmatrix} [0]_{n\times n} & [I]_{n\times n} \\ -M^{-1}\Big(\dot{Z} + N + P + K\Big) & -M^{-1}\Big(\dot{M} + Z + Z^T\Big) \end{bmatrix}\delta\boldsymbol{x} + \begin{bmatrix} [0]_{n\times m} \\ B \end{bmatrix}\delta\boldsymbol{u} \tag{7.23}$$

Just as with the traditional set of linearized equations, these equations can be constructed by simply (1) taking the partial derivatives indicated in Eq. 7.19 evaluated on the reference trajectory, and (2) substituting them into the directly linearized equation given above, Eq. 7.23.

C. Direct Estimation

In the CDEKF, the current estimate is used as the reference motion [1]. With this choice for the nominal trajectory, Eq. 7.8 and Eq. 2.31 (see Ch. II) show that the definitions of F and H are essentially the same. Note that for estimation, it is not necessary to have equations linear in the controls $\boldsymbol{u}$, so associated linearization steps can be neglected. The resulting governing equations then have the following form.

$$\dot{\hat{\boldsymbol{x}}} = \begin{bmatrix} [0]_{n\times n} & [I]_{n\times n} \\ -M^{-1}\Big(\dot{Z}+N+P+K\Big) & -M^{-1}\Big(\dot{M}+Z+Z^T\Big) \end{bmatrix} \hat{\boldsymbol{x}} + \boldsymbol{Q} \tag{7.24}$$

Comparing the structure of the state estimate propagation equation, Eq. 2.29, and Eq. 7.24 above, it is straightforward to now write the state matrix $F(t)$ in terms of the direct linearization coefficient matrices.

$$F(t) = \begin{bmatrix} [0]_{n\times n} & [I]_{n\times n} \\ -M^{-1}\Big(\dot{Z}+N+P+K\Big) & -M^{-1}\Big(\dot{M}+Z+Z^T\Big) \end{bmatrix} \tag{7.25}$$

Thus, tuning aside, for "direct estimation" one needs only to take the following steps to build a CDEKF estimation algorithm.

1. Form the kinetic and potential energies.
2. Construct the symbolic coefficient matrices of Eq. 7.19.
3. Find the symbolic coefficient matrix H_k of Eq. 2.31.
4. Evaluate the measurement matrix H_k at the current estimate.
5. Evaluate the state matrix F at the current estimate using Eq. 7.25.
6. Substitute F into the state estimate propagation equation, Eq. 7.24, and the state covariance matrix propagation equation, Eq. 2.30.

Here, it is clear that the full, nonlinear equations once again are unnecessary! The first three of these steps are performed once, whereas the last three are iterative within the CDEKF framework.

D. Summary

In this chapter, a straightforward approach for applying the ideas of direct linearization to estimation is outlined. Closer examination of the directly linearized equations of motion about a reference trajectory yields a mechanism for constructing the state matrix F (which is essential in the state covariance matrix propagation equation) without first forming the full nonlinear equations. This approach is particularly advantageous for nonlinear, multi-degree of freedom systems for which the nonlinear governing equations are quite cumbersome. Furthermore, automatic partial differentiation software, such as Object Oriented Coordinate Embedding Algorithm (OCEA), provides an additional tool for creating the coefficient matrices [37].

Though these ideas are applied to an unconstrained discrete system, it is clear that they can also be applied to wider class of systems based on the other work presented in this dissertation. Coupled with Ch. III, these same generalizations could be made from a Gibbs/Appell viewpoint to apply direct estimation to systems with nonholonomic constraints. Using the ideas of Ch. IV, redundant coordinate systems can be easily incorporated with this material. Finally, the linear and quadratic assumed modes methods result in linear equations, so there is also a connection to these ideas for continuous and hybrid systems. Overall, this "direct estimation" approach to implementing the CDEKF is a straightforward result that is easily utilized and can be applied to a broad class of systems.

CHAPTER VIII

CONCLUSION

In this dissertation, several strategies for state estimation of constrained and hybrid dynamical systems are presented. The unifying theme of the work is to provide straightforward methods for applying a well-known estimation algorithm, the continuous-discrete extended Kalman filter, to a greater class of dynamical systems.

First, direct linearization methods are expanded to accommodate constrained systems subject to nonholonomic constraints. Using a modified Gibbs-Appell perspective and quasi-velocities, this work allows one to form linearized equations of motion for constrained systems directly from the kinematics and potential energy without first constructing the nonlinear equations. When the nonlinear equations are unnecessary, this direct linearization procedure provides a convenient tool for writing the linearized state estimate propagation equations for the CDEKF.

For constrained systems that are instead represented with redundant coordinates, a "constraint force" viewpoint is employed to ease the formation of the state matrix for the CDEKF. This approximation allows one to calculate the constraint force through multiple methods, rather than find the constraint force as an explicit function of the states. For multi-body systems, this modification is particularly useful. The method is shown to be effective for two redundant coordinate examples. However, the simulation results also indicate that this approach can be more sensitive to measurement observability and sampling frequency than that which accounts for the state dependence of the constraint force in the full state matrix.

Often, the constraints are defined such that they are always held, as is the case with redundant coordinate systems. However, there exist systems for which a con-

straint may be broken. For the class of systems subject to constraint violation, it is desirable to have a method for determining when the constraint is no longer satisfied and the system dynamics are subsequently unconstrained. For example, the control strategy may be contingent on the current dynamic model. Here, two methods for determining constraint violation are presented. Each utilizes both a constraint estimate and variance associated with this estimate, where the constraint estimate variance is used as a measure to account for uncertainty associated with the state estimates. The magnitude of the constraint estimate relative to the variance is then used to select the most appropriate system model for state propagation in the CDEKF. The direct constraint construction method (Method 1) is shown to outperform the full estimation method (Method 2) for two examples in simulation. Furthermore, Method 1 is more straightforward to implement within the CDEKF structure. These two advantages recommend it over Method 2 in practice.

In addition to constrained systems, estimation for hybrid systems is also briefly investigated. Here, initial steps for considering how to accommodate integro-partial differential equations in the CDEKF are discussed. Two finite-dimensional treatments of the spatial domain, linear assumed modes and quadratic assumed modes, are employed as means to represent IPDEs and PDEs within the traditional CDEKF structure. Observations of model behavior, as well as simulation results, indicate that quadratic assumed modes, which accounts for higher-order nonlinear effects, is likely better suited for implementation with physical systems.

For constrained systems and hybrid systems, as well as finite-dimensional unconstrained systems, the method of direct estimation applies. This result unites the underlying ideas of direct linearization and the CDEKF to outline a clear, simple approach for constructing the Kalman filter for a broad class of nonlinear governing equations. Like direct linearization, direct estimation begins with the system kine-

matics and potential energy. However, in addition to the linearized equations about a reference trajectory, this approach produces the state matrix. With these two elements and a measurement model, the CDEKF is directly constructed. For unconstrained systems, direct estimation is straightforward. For constrained systems, this idea can be coupled with Gibbs-Appell directly linearized equations, and for hybrid systems it can be applied in conjunction with an assumed modes method.

Overall, this collection of strategies facilitates the application of a classic engineering tool, the continuous-discrete extended Kalman filter, to a larger class of system dynamics. These methods allow systems represented with less traditional dynamical models to benefit from a well-known, proven, and powerful estimation approach.

REFERENCES

[1] J. Crassidis and J. Junkins, *Optimal Estimation of Dynamic Systems*. Boca Raton, FL: Chapman & Hall\CRC Press, 2004.

[2] R. E. Kalman, "A new approach to linear filtering and prediction problems," *Journal of Basic Engineering*, vol. 82, pp. 35–45, 1960.

[3] R. E. Kalman and R. S. Bucy, "New results in linear filtering and prediction theory," *Journal of Basic Engineering*, vol. 83, pp. 95–107, 1961.

[4] S. J. Julier and J. K. Uhlmann, "Unscented filtering and nonlinear estimation," in *Proceedings of the IEEE*, vol. 92, no. 3, p. 422, March 2004.

[5] E. A. Wan and R. van der Menve, "The unscented Kalman filter for nonlinear estimation," in *Proceedings of the IEEE 2000 Adaptive Systems for Signal Processing, Communications, and Control Symposium*, Lake Louise, Alberta, Canada, October, pp. 153–158.

[6] N. J. Choe, "Detection and orbit determination of tethered satellite systems," Ph.D. dissertation, Dept. Aero. Eng., Auburn University, Auburn, AL, 2003.

[7] J. L. Junkins and Y. Kim, *Introduction to Dynamics and Control of Flexible Structures*. Washington, DC: American Institute of Aeronautics and Astronautics, Inc., 1993.

[8] H. Schaub and J. L. Junkins, *Analytical Mechanics of Space Systems*. Reston, VA: American Institute of Aeronautics and Astronautics, Inc., 2003.

[9] H. Baruh, *Analytical Dynamics*. New York: McGraw-Hill Companies, Inc., 1999.

[10] W. M. Lai, D. Rubin, and E. Krempl, *Introduction to Continuum Mechanics*, 3rd ed. Burlington, MA: Butterworth-Heinemann, 1999.

[11] J. E. Hurtado, *Kinematic and Kinetic Principles*. College Station, TX: John E. Hurtado/Published by Lulu, 2007.

[12] L. Meirovitch, *Computational Methods in Structural Dynamics*. Alphen aan den Rijn, The Netherlands: Sijthoff and Noordhoff International Publishers B.V., 1980.

[13] H. Goldstein, *Classical Mechanics*, 2nd ed. Reading, MA: Addison-Wesley Publishing, 1980.

[14] A. Laulusa and O. Bauchau, "Review of classical approaches for constraint enforcement in multibody systems," *Journal of Computational and Nonlinear Dynamics*, vol. 3, no. 1, pp. 011 004: 1–8, January 2008.

[15] J. E. Hurtado, "Some new methods for optimal control of constrained dynamical systems," Ph.D. dissertation, Dept. Aero. Eng., Texas A&M University, College Station, 1995.

[16] S. Lee and J. L. Junkins, "Explicit generalization of Lagrange's equations for hybrid coordinate dynamical systems," *Journal of Guidance, Control, and Dynamics*, vol. 15, no. 6, pp. 1443–1452, 1992.

[17] J. Roskam, *Airplane Flight Dynamics and Automatic Flight Controls, Part 1*. Lawrence, KS: DARcorporation, 2001.

[18] J. Stewart, *Calculus*, 2nd ed. Pacific Grove, CA: Brooks/Cole Publishing Company, 1991.

[19] J. J. Parish, J. E. Hurtado, and A. Sinclair, "Direct linearization of continuous and hybrid dynamical systems," *Journal of Computational and Nonlinear Dynamics*, vol. 4, no. 3, pp. 031 002:1–11, 2009.

[20] T. Kane and D. Levinson, *Dynamics: Theory and Applications*. New York: McGraw-Hill Book Company, 1985.

[21] T. Kane, P. Likins, and D. Levinson, *Spacecraft Dynamics*. New York: McGraw-Hill Book Company, 1983.

[22] J. W. Gibbs, "On the fundamental formulae of dynamics," *American Journal of Mathematics*, vol. II, pp. 49–64, 1879.

[23] P. Appell, "Sur une forme generale des equations de la dynamique," *Journal fúr die Reine und Angewandte Mathematik*, vol. 121, pp. 310-319, 1900.

[24] E. A. Desloge, "Relationship between Kane's equation and the Gibbs-Appell equations," *Journal of Guidance, Control, and Dynamics*, vol. 10, no. 1, pp. 120–122, 1987.

[25] L. Meirovitch, *Methods of Analytical Dynamics*. New York: McGraw-Hill Companies, Inc., 1980.

[26] T. Kane and D. Levinson, "Formulation of equations of motion for complex spacecraft," *Journal of Guidance, Control, and Dynamics*, vol. 3, no. 2, pp. 99–112, 1980.

[27] D. E. Rosenthal, "Comment on 'relationship between Kane's equation and the Gibbs-Appell equations'," *Journal of Guidance, Control, and Dynamics*, vol. 10, no. 6, pp. 595–596, 1987.

[28] A. K. Banerjee, "Comment on 'relationship between Kane's equation and the Gibbs-Appell equations'," *Journal of Guidance, Control, and Dynamics*, vol. 10, no. 6, pp. 596–597, 1987.

[29] D. Simon and T. Chia, "Kalman filtering with state equality constraints," *IEEE Transactions on Aerospace and Electronic Systems*, vol. 39, pp. 128–136, January 2002.

[30] J. D. Turner and T. Elgohary, "Generalized frequency domain state-space models for analyzing flexible rotating spacecraft," presented at The Kyle T. Alfriend Astrodynamics Symposium, Monterey, CA, May 17-19, 2010.

[31] S. R. Beaver, "Input-output approximation for nonlinear structural dynamics," M.S. thesis, Dept. Aero. Eng., Texas A&M University, College Station, 2007.

[32] D. J. Segalman and C. R. Dohrmann, "A method for calculating the dynamics of rotating flexible structures. 1. derivation," *Journal of Vibration and Acoustics*, vol. 118, no. 3, pp. 313–317, July 1996.

[33] ——, "A method for calculating the dynamics of rotating flexible structures. 2. example calculations," *Journal of Vibration and Acoustics*, vol. 118, no. 3, pp. 318–322, July 1996.

[34] B. Yagcia, S. Filiza, L. L. Romerob, and O. B. Ozdoganlar, "A spectral-Tchebychev technique for solving linear and nonlinear beam equations," *Journal of Sound and Vibration*, vol. 321, no. 1-2, pp. 375–404, March 2009.

[35] A. J. M. Ferreira and G. E. Fasshauer, "Computation of natural frequencies of shear deformable beams and plates by an RBF-pseudospectral method," *Computer Methods in Applied Mechanics and Engineering*, vol. 196, no. 1-3, pp.

134–146, December 2006.

[36] J. J. Parish, "Direct linearization of continuous and hybrid dyanmical systems," M.S. thesis, Dept. Aero. Eng., Texas A&M University, College Station, 2007.

[37] D. Griffith, J. Turner, and J. Junkins, "Automatic generation and integration of equations of motion for flexible multibody dynamical systems," *Journal of the Astronautical Sciences*, vol. 53, no. 3, pp. 251–279, 2005.

[38] N. A. Denissen, "Roughness-induced transient growth: Continuous-spectrum receptivity and secondary instability analysis," Ph.D dissertation, Dept. Aero. Eng., Texas A&M University, College Station, 2011.

[39] ——, "Numerical methods for differential eigenvalue problems," Lecture notes, Dept. Aero. Eng., Texas A&M University, College Station, 2011.

APPENDIX A

NUMERICAL SOLUTION FOR THE DIFFERENTIAL EIGENVALUE PROBLEM

This appendix provides a brief outline of a numerical solution for finding the Eigenvalues (and Eigenfunctions) of a boundary-value problem consisting of a linear differential equation over a specified spatial domain with boundary conditions. References [7], [12], [34], [38], and [39] each contribute to the discussion that follows.

A. Differential Eigenvalue Problem

Consider the class of problems that can be written in the following form.

$$L\phi = \lambda R\phi \tag{A.1}$$

$$B_i\phi = 0 \qquad i = 1 \ldots p \tag{A.2}$$

Here, λ is the Eigenvalue, and L and R are linear differential operators of respective order $2p$ and $2q$ acting on the spatially dependent Eigenfunction $\phi(x)$ with $p > q$. The linear differential operator associated with the boundary conditions, B_i, has maximum order $2p - 1$. This class of problems typically has an infinite number of Eigenvalues and associated Eigenfunctions.

B. Transformation to an Algebraic Eigenvalue Problem

The differential Eigenvalue problem of Eq. A.1 can be transformed to an algebraic problem (with some discretization error) by applying the pseudo-spectral method. First, the Eigenfunction is approximated as a linear combination of $N+1$ orthogonal functions T_n.

$$\phi(x) \approx a_n T_n(x) \qquad n = 0 \ldots N \tag{A.3}$$

The approximation approaches the true Eigenfunction as $N \to \infty$. Here, Tchebychev polynomials are chosen as the orthogonal (on the weighted domain $-1 < \eta < 1$) basis functions used to approximate the Eigenfunction because they can accommodate mixed boundary conditions. The true domain, $l_1 < x < l_2$, can be easily mapped to and from the region $-1 < \eta < 1$.

$$\eta(x) = \frac{2}{l_2 - l_1}x - \frac{l_2 + l_1}{l_2 - l_1} \quad ; \quad x(\eta) = \frac{l_2 - l_1}{2}\eta + \frac{l_2 + l_1}{2} \tag{A.4}$$

The Tchebychev polynomials are primarily defined using their recursive property.

$$\begin{aligned} T_0 &= 1 \\ T_1 &= \eta \\ T_n &= 2\eta T_{n-1} - T_{n-2} \end{aligned} \tag{A.5}$$

A helpful feature related to this recursion is that the polynomial derivatives have the following form.

$$\frac{\mathrm{d}^k}{\mathrm{d}\eta^k}(T_n(x)) = 2n\frac{\mathrm{d}^{k-1}}{\mathrm{d}\eta^{k-1}}(T_{n-1}) + \frac{n}{n-2}\frac{\mathrm{d}^k}{\mathrm{d}\eta^k}(T_{n-2}) \tag{A.6}$$

Here, the kth derivative is a function of the next two lower-order polynomials. This characteristic allows differentiation to be written as a matrix operation.

$$\phi'(\eta) = \frac{\mathrm{d}}{\mathrm{d}\eta}\left(\phi(\eta)\right) = \frac{\mathrm{d}}{\mathrm{d}\eta}\left(a_n T_n(\eta)\right) = a_m D_{mn} T_n(\eta) \tag{A.7}$$

This $N+1 \times N+1$ differentiation matrix D can be written as follows.

$$D = \begin{bmatrix} 0 & 1 & 0 & 3 & 0 & 5 & \dots \\ 0 & 0 & 4 & 0 & 8 & 0 & \dots \\ 0 & 0 & 0 & 6 & 0 & 10 & \dots \\ 0 & 0 & 0 & 0 & 8 & 0 & \dots \\ \vdots & \vdots & \vdots & \vdots & \vdots & \vdots & \vdots \end{bmatrix} \tag{A.8}$$

The matrix elements D_{ij} from Eq. A.6 are given below.

$$\begin{aligned} D_{1,1+2j-3} &= 2j-3 \qquad j \geq 2 \\ D_{i,i+2j-3} &= 2(i+2j-4) \qquad i \geq 2,\, j \geq 2 \end{aligned} \tag{A.9}$$

Note that the differentiation matrix can again be post-multiplied to apply higher-order differentiation (i.e. $\phi'' = TDD\boldsymbol{a}$).

The goal is to now solve for the Eigenvalues λ and the associated Eigenvector of coefficients a_n used in the Eigenfunction approximation. To have a sufficient number of algebraic equations, $N+1$ collocation points on which to evaluate $T_n(x)$ are needed. Gauss-Lobatto sampling for the collocation points is used to maximize accuracy.

$$\eta_j = \cos\left(\frac{j\pi}{N}\right) \qquad j = 0 \dots N \tag{A.10}$$

Note that $\eta_0 = 1$ and $\eta_N = -1$. The matrix T of Tchebychev polynomials can then be defined.

$$T = \begin{bmatrix} T_0(\eta_0) & \dots & T_N(\eta_0) \\ \vdots & & \vdots \\ T_0(\eta_N) & \dots & T_N(\eta_N) \end{bmatrix} \tag{A.11}$$

For building the T matrix, an alternative definition of the Tchebychev polynomials

is helpful.

$$T_n(\eta_j) = \cos\left(n\cos^{-1}(\eta_j)\right) \tag{A.12}$$

Once Eqs. A.1, A.3, A.12, A.11, and A.8 have been applied, the problem takes the form of an algebraic Eigenvalue problem.

$$A\boldsymbol{a} = \lambda B\boldsymbol{a} \tag{A.13}$$

The boundary conditions are enforced using Eqs. A.3 and A.7 and then substituting these results into the appropriate rows of Eq. A.13. The resulting form of the Eigenvalue problem can then be solved using any number of numerical methods available. Note that enforcement of each boundary condition results in an associated "infinite" Eigenvalue to be ignored.

C. Example: Cantilevered Beam

Consider the classic distributed parameter example of a cantilevered beam of length L. Using separation of variables, as described in Ch. VI, the ODE over the spatial domain and boundary conditions can be found.

$$\phi''''(x) - \beta^4\phi(x) = 0 \tag{A.14}$$

$$\phi''(L) = 0 \quad ; \quad \phi'''(L) = 0 \quad ; \quad \phi(0,t) = 0 \quad ; \quad \phi'(0,t) = 0 \tag{A.15}$$

Applying Eqs. A.3 and A.8 to Eq. A.14 with $\lambda = \beta^4$ yields the following Eigenvalue problem.

$$TDDDD\boldsymbol{a} = \beta^4 T\boldsymbol{a} \rightarrow A\boldsymbol{a} = \lambda B\boldsymbol{a} \tag{A.16}$$

The boundary conditions are enforced as follows.

$$\begin{aligned}
&\phi(x=0)=0 \rightarrow \phi(\eta=-1)=0 \rightarrow \\
&\qquad A(N,:)=T(N,:)\,;\; B(N,:)=[0]_{1\times N+1} \\
&\phi'(x=0)=0 \rightarrow \phi'(\eta=-1)=0 \rightarrow \\
&\qquad A(N-1,:)=TD(N,:)\,;\; B(N-1,:)=[0]_{1\times N+1} \\
&\phi''(x=L)=0 \rightarrow \phi''(\eta=1)=0 \rightarrow \\
&\qquad A(0,:)=TDD(0,:)\,;\; B(0,:)=[0]_{1\times N+1} \\
&\phi'''(x=L)=0 \rightarrow \phi'''(\eta=1)=0 \rightarrow \\
&\qquad A(1,:)=TDDD(0,:)\,;\; B(1,:)=[0]_{1\times N+1}
\end{aligned} \tag{A.17}$$

Using the MATLAB function *eig(A,B)* with $N = 124$, Eq. A.16 can be solved for close approximations of the Eigenvalues. Table IV shows the first eight values for $\omega_i = \sqrt{16\lambda_i}$ together with reference values given by Ref. [7] for comparison. The same underlying system parameters ($\rho = E = I = 1$) are used with the exception of L: the coefficient of λ has the value $L^4 = 2^4 = 16$ due to the length of the domain, $\{-1 < \eta < 1\}$, and the definition $\lambda = \beta^4$.

This method is able to efficiently solve for near approximations of the true Eigenvalues for this example. The Eigenvectors associated with each of the Eigenvalues gives the vector of coefficients for the linear combination of $N + 1$ Tchebychev polynomials used to approximate each Eigenfunction. Alternatively, if the form of the Eigenfunctions is explicitly known, the Eigenvalues can be used to write these functions (and their associated amplitudes for the PDE problem of Ch. VI).

Table IV. Exact and Pseudo-Spectral Method Eigenvalues.

ω_i	Pseudo-Spectral	Exact
ω_1	3.5187	3.5160
ω_2	22.0324	22.0345
ω_3	61.6961	61.6972
ω_4	120.9036	120.9019
ω_5	199.8603	199.8595
ω_6	298.5556	298.5555
ω_7	416.9907	416.9908
ω_8	555.1652	555.1652

D. Summary

In this Appendix, a numerical method for finding the Eigenvalues (and subsequently their associated Eigenfunctions) is described and demonstrated for a well-known example. Applying the pseudo-spectral method with Tchebychev polynomial basis functions is shown to be an effective approach for solving the class of differential Eigenvalue problems outlined herein. This method is particularly promising for linear differential equations for which the exact Eigenfunctions are not known *a priori* (unlike the simple example presented here). These methods are commonly used in fluid mechanics, and other, similar tools from the aerofluids discipline would likely prove useful in the analysis of continuous and hybrid systems in structural dynamics.

VITA

Julie Marie Jones Parish began her undergraduate studies at Texas A&M University in August 2001. In August 2005, she began her graduate studies under the advisement of Dr. John E. Hurtado at Texas A&M. Ms. Parish received her Bachelor of Science degree in Aerospace Engineering from Texas A&M University in May 2005, Master of Science degree in Aerospace Engineering from Texas A&M University in December 2007, and Doctorate of Philosophy degree in Aerospace Engineering from Texas A&M University in August 2011.

During her studies, Ms. Parish was awarded the NDSEG and NSF graduate fellowships. She was also the recipient of the AIAA Orville and Wilbur Wright Graduate Award, NASA/Texas Space Grant Consortium Fellow, and Zonta International Amelia Earmark Fellowship. Her undergraduate achievements included receiving a National Merit Scholarship and the Crag Brown Outstanding Senior Engineer Award. Professionally, Julie has interned as a graduate fellow with the Department of Defense and at Sandia National Laboratories, and she has accepted an offer of employment at Sandia National Laboratories beginning Fall 2011.

Ms. Parish may be reached at julieparish@tamu.edu or by contacting Dr. John E. Hurtado, Department of Aerospace Engineering, Texas A&M University, College Station, TX 77843-3141.